

Mechanical Characterization of Irregular Architected Two-Phase Materials

Thesis by
Chelsea Fox

In Partial Fulfillment of the Requirements for the
Degree of
Doctor of Philosophy in Mechanical Engineering

The Caltech logo, featuring the word "Caltech" in a bold, orange, sans-serif font, centered within a light orange rectangular background.

CALIFORNIA INSTITUTE OF TECHNOLOGY
Pasadena, California

2025
(Defended May 12, 2025)

© 2025

Chelsea Fox
ORCID: 0009-0002-6612-8309

ACKNOWLEDGEMENTS

I would first like to thank my advisor, Prof. Chiara Daraio, for the amazing opportunity to be a part of her research group. I have learned so much from her about how to approach research and solve problems, and I could not be more grateful for all of her encouragement and enthusiasm as we pursued exciting research. I would also like to thank the members of the Daraio group for all of the great discussions, research collaborations, and friendships along the way, especially Tommaso Magrini, Beatriz Arsuffi, Israel Kellersztein, Connor McMahan, and Adeline Wihardja (who is an honorary group member). I would also like to thank the excellent SURF students, Athena Kolli, Kyle Chen, and Kyrillos Bastawros, who made summer research a fun and rewarding experience. All of our work would not have been possible without the experimental and fabrication assistance from Petros Arakelian, or without the administrative assistance from Carolina Oseguera, Jenni Campbell, and Lynn Seymour. I would also like to thank Prof. Guruswami Ravichandran, Prof. Ruby Fu, and Prof. Katherine Faber for serving as my thesis committee members. Finally, I would like to thank my parents for all of their love and support along the way.

ABSTRACT

Architected materials offer a wide range of mechanical properties through the choice of their constitutive materials and the design of their structure. Periodic architected materials are the most widely studied and used in practical applications, as their repeating unit cells are easy to design, fabricate, and analytically model, but these materials are only a small subset of the possible design space. Irregular architected materials, which are aperiodic but not necessarily stochastic, offer a way to achieve a wider design space of mechanical properties.

In this thesis, we explore the design space of irregular architected materials and relate structural irregularity to the mechanical properties using measures of topology and geometry. We show that these measures of irregularity can be used to spatially and temporally control the mechanical response across linear and non-linear regimes, including fracture and dynamic impact, and we show that irregularity leads to improved mechanical properties when compared with periodic equivalents. To generate the irregular architected materials, we use a virtual growth algorithm, which imitates the stochastic growth process of biological structures by assembling a finite set of building blocks according to local connectivity rules. By varying the building blocks and connectivity rules, we show how to achieve a wide range of structures with varying degrees of irregularity all the way up to fully periodic structures. This thesis primarily focuses on the fabrication and characterization of additively manufactured two-phase polymer composites, but the design methods and irregular structure characterizations are material-agnostic, opening up a wide design space for future architected materials which use irregularity to achieve excellent mechanical performances.

PUBLISHED CONTENT AND CONTRIBUTIONS

- [1] T. Magrini, C. Fox, A. Wihardja, A. Kolli & C. Daraio, (2023). “Control of Mechanical and Fracture Properties in Two-Phase Materials Reinforced by Continuous, Irregular Networks”. *Advanced Materials* 36 (6), 2305198. doi: 10.1002/adma.202305198.

C.F. participated in the design, fabrication, and testing of samples, data analysis and visualization, and in writing and revising the manuscript.

- [2] C. Fox, K. Chen, M. Antonini, T. Magrini & C. Daraio, (2024). “Extracting Geometry and Topology of Orange Pericarps for the Design of Bioinspired Energy Absorbing Materials”. *Advanced Materials* 36 (36), 2405567. doi: 10.1002/adma.202405567.

C.F. participated in the conceptualization, design, fabrication, and testing of samples, data analysis and visualization, and in writing and revising the manuscript.

- [3] C. Fox, T. Magrini & C. Daraio, (2024). “Fracture Characterization of Bioinspired Irregular Network Reinforced Composites” (In Review). doi: 10.48550/arXiv.2410.09061.

C.F. participated in the conceptualization, design, fabrication, and testing of samples, data analysis and visualization, and in writing and revising the manuscript.

- [4] C. Fox, K. Bastawros, T. Magrini & C. Daraio, (2025). “Controllable Interlocking from Irregularity in Two-Phase Composites” *Matter* (Accepted). doi: 10.48550/arXiv.2502.18392.

C.F. participated in the conceptualization, design, fabrication, and testing of samples, data analysis and visualization, and in writing and revising the manuscript.

- [5] C. Fox, K. Bastawros, T. Magrini & C. Daraio, (2025). “Mechanical and Temporal Response of High-Coordinated Irregular Network Reinforced Composites” (In Preparation).

C.F. participated in the conceptualization, design, fabrication, and testing of samples, data analysis and visualization, and in writing and revising the manuscript.

TABLE OF CONTENTS

Acknowledgements.....	iii
Abstract.....	iv
Published Content and Contributions	v
Table of Contents	vi
List of Illustrations.....	xi
Chapter I: Introduction.....	1
1.1 Research Objectives.....	1
1.2 Motivation.....	1
1.3 Chapter Outlines	4
1.4 Experimental Methods.....	5
1.4.1 Quasi-static Characterization.....	5
1.4.2 Fracture Characterization.....	5
1.4.3 Dynamic Characterization	7
1.4.4 Digital Image Correlation	9
Bibliography	11
Chapter II: Control of Mechanical and Fracture Properties in Two-Phase Materials Reinforced by Continuous, Irregular Networks.....	15
Abstract.....	15
2.1 Introduction.....	16
2.2 Design of Irregular Reinforcement	17
2.3 Network Characterization	18
2.4 Mechanical Properties.....	20
2.5 Conclusions.....	27
Bibliography	29
Chapter III: Fracture Characterization of Bioinspired Irregular Network Reinforced Composites.....	32

Abstract	32
3.1 Introduction.....	33
3.2 Materials and Methods.....	35
3.3 Results and Discussion	37
3.3.1 Single Edge Notch Plate Tension Fracture Tests	37
3.3.2 Fracture Behavior of the Composites: Plastic Zone Formation and Crack Extension	39
3.3.3 Effect of Structural Features	42
3.3.4 Plastic Zone Tailoring	45
3.4 Conclusions.....	46
Bibliography	48
Chapter IV: Mechanical and Temporal Response of High-Coordinated	
Irregular Network Reinforced Composites	51
Abstract	51
4.1 Introduction.....	52
4.2 Material Design, Generation and Characterization.....	53
4.2.1 Sample Generation.....	53
4.2.2 Structural Characterization	56
4.3 Results and Discussion	57
4.3.1 Homogeneous Topology Tensile Plate Tension Tests	57
4.3.2 Inhomogeneous Topology Tensile Plate Tension Tests.....	60
4.3.3 Fracture and Temporal Response of the Composites.....	62
4.4 Conclusions.....	65
Bibliography	67
Chapter V: Extracting Geometry and Topology of Orange Pericarps	
for the Design of Bioinspired Energy Absorbing Materials	70
Abstract	70
5.1 Introduction.....	71
5.2 Methods, Results and Discussion	73

5.2.1 Bioinspired Material Design	73
5.2.2 Material Generation and Fabrication	74
5.2.3 Mechanical Characterization: Quasi-static Testing.....	79
5.2.4 Mechanical Characterization: Structural Feature Analysis.....	81
5.2.5 Mechanical Characterization: Dynamic Testing	83
5.3 Conclusions.....	85
Bibliography	87
Chapter VI: Controllable Interlocking from Irregularity in Two-Phase	
Composites.....	91
Abstract	91
6.1 Introduction.....	92
6.2 Results and Discussion	93
6.2.1 Sample Design	93
6.2.2 Mechanical Characterization: Cylindrical Contact Loading.....	95
6.2.3 Mechanical Characterization: Matrix Response	98
6.2.4 Mechanical Characterization: Particle Response.....	101
6.2.5 Mechanical Characterization: Statistical Analysis.....	104
6.3 Conclusions.....	107
6.4 Methods.....	108
6.4.1 Sample Generation and Fabrication.....	108
6.4.2 Cylindrical Contact Compression Loading.....	109
6.4.3 Digital Image Correlation	110
Bibliography	111
Chapter VII: Conclusions	
7.1 Summary of Contributions.....	115
7.2 Outlook and Future Research Directions	116
7.3 Bibliography	120
Appendix A: Control of Mechanical and Fracture Properties in Two-Phase	
Materials Reinforced by Continuous, Irregular Networks.....	121

A.1 Experimental Section	121
A.1.1 Sample Fabrication	121
A.1.2 Mechanical Characterization.....	121
A.1.3 Digital Image Correlation	122
A.2 Supplementary Figures	122
A.3 Supplementary Discussion.....	128
A.3.1 The Virtual Growth Algorithm.....	128
A.3.2 The Reinforcing Networks.....	129
A.3.3 The Mechanical Behavior of the Reinforcing Networks	129
A.3.4 The Iterative Modification Design Process.....	130
A.3.5 The Polydispersity Index (PDI)	132
Appendix B: Fracture Characterization of Bioinspired Irregular Network Reinforced Composites	135
B.1 Supplementary Figures.....	135
B.2 Supplementary Discussion	139
B.2.1 Structural Feature Characterization.....	139
Appendix C: Mechanical and Temporal Response of High-Coordinated Irregular Network Reinforced Composites.....	140
C.1 Supplementary Figures.....	140
Appendix D: Extracting Geometry and Topology of Orange Pericarps for the Design of Bioinspired Energy Absorbing Materials	142
D.1 Supplementary Figures	142
D.2 Supplementary Discussion.....	146
D.2.1 Sample Preparation and Imaging	146
D.2.2 Bioinspired Sample Generation	148
D.2.3 Quasi-static Mechanical Testing	148
D.2.4 Digital Image Correlation	149
D.2.5 Dynamic Testing	149
D.2.6 Dynamic Wave Speed Testing.....	149

D.2.7 Tiles and Connectivity Rules	150
D.2.8 Quasi-static Sample Anisotropy Testing	150
Appendix E: Controllable Interlocking from Irregularity in Two-Phase Composites.....	153
E.1 Supplementary Figures	153

LIST OF ILLUSTRATIONS

<i>Number</i>	<i>Page</i>
1.1 Drop tower configuration.....	9
2.1 Architecture of two-phase materials. (a) Selected isodensity tile geometries and composite assembly. (b) Compositional design space in a ternary diagram. (A) and (B) architectures are represented by red and blue circles, respectively. (c) Average coordination $\langle R \rangle$ as a function of [T] tiles content. (A) and (B) reinforcing networks are represented by red and blue circles, respectively. d,e) Representative (A) and (B) architectures (d and e, respectively). (f,g) Close-up view of meso-structures that populate (A) and (B) architectures in (d) and (e), respectively. Yellow, green, cyan, and blue represent 4, 6, 8, and 10+ tiles meso-structures, respectively. (h) Meso-structure distributions in (A) (red bars) and (B) architectures (blue bars). (i) Example of meso-structure with labeled coordination and bridges. (j) Expanded version of (i). (k) Comparison of bridge length and their frequency for (A) and (B) architectures (red and blue, respectively).....	18
2.2 Mechanical characterization of composites. (a,b) Engineering stress–strain curves recorded during uniaxial tension tests on plate geometries of (A)-NRC's and (B)-NRC's (red solid lines in a, blue solid lines in b, respectively). The solid black lines in (a,b) represent the response of samples photographed in (c,d), respectively. The solid gray lines in (a,b) represent the response of the same (A)-NRC and (B)-NRC samples, without the matrix phase. Fracture events in the reinforcing phase of (A)-NRC's and (B)-NRC's are indicated by red and blue arrows in (a) and (b), respectively, and in the reinforcing networks by gray arrows (see also Figure A.6). (c,d) Fracture evolution in representative samples of (A)-NRC and (B)-NRC, respectively. The circles indicate the locations within the samples that display the signs of voids growth (circles in (c) and (d), frame II and insets in (c) and (d), frame II, bottom). (e,f) Digital image correlation (DIC) maps of the representative samples of (A)-NRC and (B)-NRC recorded at 0.5% strain (e and f, respectively). The DIC maps	

refer to the areas of samples highlighted by (*) in frame I of c) and d).	21
2.3 Modified composites and their performance. (a) Modifications of connectivity rules and average coordination number as a function of [T] tiles (top and bottom, respectively). (b) Engineering stress–strain diagram of Mod-(A)-NRC's (red solid lines) and of original (A)-NRC's (gray solid lines). The modulus of toughness (MOT) is reported for both composites at the top of the diagram. (c,d) Fracture evolution in representative Mod-(A)-NRC at 0.5% and 16% strain (c and d, respectively). (e) Engineering stress–strain diagram of Mod-(B)-NRC's (blue solid lines) and of the original (B)-NRC's (gray solid lines). The MOT is reported for both composites at the top of the diagram. (f,g) Fracture evolution in representative Mod-(B)-NRC at 0.5% and 16% strain (f and g, respectively). (h,i) Modification of microstructure of (A)- and (B)-networks (h and i, respectively) and measured polydispersity index (PDI) for each network. (j,k) Variation in relative meso-structure orientation distribution of (A) and (B)-networks (j and k, respectively). (l) Frequency of bridge lengths for (A)- and Mod-(A)-networks (top and bottom, respectively). (m) Frequency of bridge lengths for (B)- and Mod-(B)-networks (top and bottom, respectively).	24
2.4 Multiarchitecture meso-scale assemblies. (a,b) Laminate assemblies: (A), Mod-(B), (A) and Mod-(B), (A), Mod-(B) (a and b, respectively). The insets highlight differences in reinforcing architecture. Fracture evolution (I, II, III (a) and (b), respectively). (c,d) DIC maps at 0.5% strain in laminate assemblies. (e) Sketch of cross section of cortical bone (f) Cortical bone inspired meso-scale assembly. Mod-(A) constitutes osteon-inspired features (dashed red semicircles), (A) constitutes the matrix phase. (g) DIC map at 7% strain and highlighting strain distribution in cortical bone inspired assembly. (h,i) Fracture evolution at 11% and 21% strain (h and i, respectively).	27
3.1 Material and structural characterization. (a) VGA tiles and coordination numbers. (b) VGA connectivity rules, green is allowed, red is not allowed. (c) Fracture samples with characteristic length scale. (d) Average coordination number. (e) Constitutive uniaxial stress-strain plot for reinforcing and matrix phase materials. (f-i) Frequency of 2.3 coordination structural	

feature areas for 5x5, 10x10, 20x20 and 30x30 tiles. (j) Exponential fits of structural feature areas for 2.3, 2.5 and 2.8 coordination samples with 30x30 tiles. (k) Exponential fit parameters for increasing sizes of sample regions of interest.	36
3.2 Mechanical characterization and DIC images of plastic zone growth for bulk material and composite samples. (a-e) Force-displacement plots for bulk and composite samples. (f-j) 2D DIC strain maps of bulk and composite samples with plasticity threshold in red and time stamps.	38
3.3 Plastic zone size, crack extension length, J-integrals and R-curves for composite material samples. S corresponds to start of test, Y corresponds to yielding, C corresponds to crack initiation, F corresponds to failure. (a) Plastic zone area as a function of displacement for 2.3, 2.5, and 2.8 coordination samples. (b) Crack extension length as a function of displacement for 2.3, 2.5, and 2.8 coordination samples, with inset showing single edge notch plate tension sample dimensions. (c) Incremental elastic J-integrals (η_e normalized) and plastic J-integrals (η_p normalized) as a function of displacement for 2.3, 2.5, and 2.8 coordination samples. (d) R-curves for 2.3, 2.5, and 2.8 coordination samples.	41
3.4 Structural feature analysis. (a) Zoomed images of maximum plastic zone area for 2.3, 2.5, and 2.8 coordination samples with overlaid map of structural features. (b) Sample bridges for lengths of 1, 2, 3, and 4 mm (characteristic lengths). (c) Distributions of bridge lengths for 2.3, 2.5, and 2.8 coordination samples. (d) Samples with highlighted structural features ahead of the crack tip that contribute to the plastic zone shape for 2.3, 2.5, and 2.8 coordination samples. (e) Sample structural features with their constitutive bridges for 2.3, 2.5, and 2.8 coordination samples (gray, green, red, respectively). (f) Distributions of angles of alignment of structural features for 2.3, 2.5, and 2.8 coordination samples.	44
3.5 Tailoring the plastic zone. (a) 2.3 coordination and 2.8 coordination edge sample force-displacement plot. (b) Plastic zone size growth for 2.3 and 2.8 coordination edge sample. (c) 2D DIC strain maps for 2.3 coordination edge sample. (d) 2D DIC strain maps for 2.8 coordination edge sample.	46

4.1 Hexa-VGA generated sample design and characterization. (a) Hexa-VGA tiles. (b) Example hexa-VGA generated network and plate tension sample. (c) Tile distributions for each coordination and topology type. (d) Average area as a function of coordination number. (e) Maxwell number as a function of coordination number.	55
4.2 Geometry characterization of reinforcing network phase. (a-e) Radial distribution functions for homogeneous coordination samples. (f-n) Structural feature area distributions for all coordination samples. (o) Example of triangle normalized area. (p) Polydispersity index (PDI) as a function of coordination number for all coordination samples.	57
4.3 Tensile testing of irregular network reinforced composites. (a-e) Tensile stress-strain response of 2H_2X, 3H_3X, 4H_4X, 5H_5X and 6H_6X coordination samples. (f-j) Example 2D DIC ε_y strain fields for each sample from 0 to 2% global tensile strain. (k) Tensile stress-strain response of volume fraction equivalent samples.	60
4.4 Characterizing the effect of inhomogeneous topology on irregular network composites. (a) Tensile stress-strain response of 3H_3X, 3nH_24X and 3nH_15X samples. (b) Tensile stress-strain response of 4H_4X, 4nH_35X and 4nH_15X samples. (c-e) Example 2D DIC ε_y strain fields for 3H_3X, 3nH_24X and 3nH_15X samples at 2% global tensile strain. (f-h) Example 2D DIC ε_y strain fields for 4H_4X, 4nH_35X and 4nH_15X samples at 2% global tensile strain. (i) Volume fraction of reinforcing phase as a function of coordination number. (j) Modulus of toughness (MOT) (volume fraction normalized) as a function of coordination number.	62
4.5 Temporal characterization of irregular network composite fracture response. (a-c) Time evolution of crack nucleation and propagation for example 3H_3X, 5H_5X and 6H_6X composites. (d-h) Crack surface area opened as a function of tensile strain for homogeneous coordination samples, dashed lines show periodic volume fraction equivalent 6H_6X samples. (i) Time from fracture initiation to complete loss of load-bearing capacity in all samples. (j) Maximum crack area opened. (k) Average crack area opening rate for all samples.	65

- 5.1 Bioinspired material design method. (a) Orange pericarp image with right half as skeletonized structure. (b) Skeletonized structure with node locations. (c) Irregular tiles from skeleton. (d) Translation of biological tiles into reduced tile types using perimeter identification numbers and summation. (e) Connectivity rules from skeleton image. (f) Reduced set of five VGA tiles and their coordination number, R . (g) VGA-allowed and -not-allowed connectivity rules. (h) Example image of orange pericarp. (i) Example of VGA-generated sample.74
- 5.2 Orange pericarp characterization and VGA sample generation. (a) Cross-sectional image of orange pericarp. (b) Representative image of external region. (c) Representative image of internal region. (d) Tile percentages for external and internal regions. (e) Selected connectivity rule percentages for external and internal regions. (f) VGA-generated sample of external region. (g) VGA-generated sample of internal region. (h) 3D-printed composite polymer sample with 80% + 20% external and internal regions, respectively. (i) External and internal region density for orange pericarp and VGA samples. (j) External and internal region concavity ratio for orange pericarp and VGA samples.78
- 5.3 Quasi-static compression tests. (a) VGA-ext engineering stress-strain plot for three different samples. (b) VGA-int engineering stress-strain plot for three different samples. (c) VGA-full engineering stress-strain plot for three different samples. (d) Example 2D DIC strain maps for 0%, 5%, and 10% global strain for VGA-ext sample, yellow insets show coordination color coded example structural features. (e) Example 2D DIC strain maps for 0%, 5%, and 10% global strain for VGA-int sample, yellow insets show concave structural features at high strain and coordination color coded example structural feature. (f) Example 2D DIC strain maps for 0%, 5%, and 10% global strain for VGA-full sample, yellow insets show concave structural features at high strain.81
- 5.4 Experimental and finite element analysis of changes in structural feature morphology under quasi-static compressive loading. (a,c) Experimental testing of VGA-full structural features from 0% to 10% global strain, insets show example features with example bending angles. (b,d) Finite element analysis of VGA-full reinforcing phase structural features from 0% to 10% global strain. (e) Comparison of experimental and finite element

analysis of variations in bending angle of example structural features from 0% to 10% global strain. (f) Defining elliptic fit of structural features and their resulting eccentricity as a way to measure structural feature deformation. (g) Tracking the eccentricity of all structural features from 0% to 10% global strain in the VGA-full reinforcing phase (left) and in honeycomb reinforcing phase (right).	83
5.5 Drop tower testing. (a) VGA-full samples before, during and after loading. (b) Time versus distance of resliced striker/sample center axis with time in contact, and angles giving striker initial and final velocities. (c) Coefficient of restitution normalized for density for VGA-ext, VGA-int, VGA-full and honeycomb polymer composite samples as a function of concavity ratio. (d) Striker time in contact with sample for VGA-ext, VGA-int, VGA-full and honeycomb polymer composite samples. (e) VGA-full samples before and at maximum strain with highlighted large structural features. (f) Highlighted large structural features before and at maximum strain. (g) Coordination color coded tiling of largest structural feature.	85
6.1 Sample generation and characterization of design space. (a) Node identification with positive (green) and negative (red) nodes. (b) Assorted hexagonal tiles. (c) Hexagonal tile connectivity. (d) Composite material generation with reinforcing particles and matrix. (e) Hexa-VGA sample compositions as a function of coordination number. (f) Triangle-normalized particle size distributions as a function of coordination number.	95
6.2 Cylindrical contact loading characterization. (a-f) Force-displacement plots for coordinations 2X, 2.5X, 3X, 3.5X, 4X and 6X, respectively. Red refers to vertical matrix orientation, blue refers to horizontal matrix orientation, gray line highlights 1 mm displacement. (g-l) Selected samples with vertical orientation. (m-r) 2D DIC maps of ϵ_x strain for corresponding selected samples. (s-x) 2D DIC maps of ϵ_y strain for corresponding selected samples.	98
6.3 Matrix response characterization. (a-c) Example 3.5X matrix ϵ_x strain with increasing cylindrical contact displacement. (d) Volume normalized fraction of matrix engaged as a function of coordination number and cylindrical contact displacement for ϵ_x	

- strain. (e) Volume normalized fraction of matrix engaged as a function of coordination number and cylindrical contact displacement for ε_y strain. (f-k) Example 2X, 2.5X, 3X, 3.5X, 4X and 6X matrix ε_x strains at 1 mm cylindrical contact displacement with corresponding horizontally averaged ε_x strain values (grayscale bars with line plot average). (l) Average ε_x strain value as a function of depth for all 2X, 3X and 4X coordinations at 1 mm cylindrical contact displacement. (m) Average ε_x strain value as a function of coordination number for all 2X, 3X and 4X coordinations at various sample depths.....100
- 6.4 Particle response characterization. (a) Example 3X particle image at 0.5 mm (I) and 1 mm (II) cylindrical contact displacement. (b) Corresponding particle vector map at 0.5 mm (I) and at 1 mm (II) displacement. (c) Histogram of vector map line angle frequencies at 0.5 mm (I) and 1 mm (II) displacement. (d) Example 4X particle image at 0.5 mm (I) and 1 mm (II) displacement. (e) Corresponding particle vector map at 0.5 mm (I) and at 1 mm (II) displacement. (f) Histogram of vector map line angle frequencies at 0.5 mm (I) and 1 mm (II) displacement. (g) Example 6X particle image at 0.5 mm (I) and 1 mm (II) displacement. (h) Corresponding particle vector map at 0.5 mm (I) and at 1 mm (II) displacement. (i) Histogram of vector map line angle frequencies at 0.5 mm (I) and 1 mm (II) displacement.103
- 6.5 Statistical characterization of matrix and particles. (a) Continuous tiles for 60° example matrix plane according to coordination number. (b) Discontinuous tiles for 60° example matrix plane according to coordination number. (c) Example of continuous and discontinuous tiling plane. (d) Probability of continuous tiling as a function of number of tiles for various coordination numbers. (e) Examples of counts of neighboring particles per particle. (f) Neighboring particles per particle as a function of corrected coordination number, solid black line denotes upper limit. (g) Example of convex (red) particle and concave (green) and geometries. (h) Average neighboring particles per particle as a function of maximum continuous tiling, dashed black line denotes concavity threshold, solid black line denoted upper limit.107
- 7.1 Preliminary results of isodensity irregular network metallic samples. (top) VGA-generated periodic (left) and irregular

network architectures with low-coordination (center) and high coordination (right). (bottom) Metallic periodic (left) and irregular network samples with low-coordination (center) and high coordination (right)	118
A.1 Connectivity rules for (L), (T) and (-) tiles, with allowed connections (green shade) and prevented connections (red shade).....	122
A.2 (a) Meso-structure dimension analysis using elliptic fit to find X_m (meso-structure size), performed by image analysis. ² (b) Meso-structure size distributions for (A) and (B) architectures relating X_m dimension to concentration percent. Yellow, green, cyan and blue represent 4, 6, 8, and 10+ tiles meso-structures, respectively.....	122
A.3 (a,b) Meso-structure angle distribution in (A) and (B) networks (a and b respectively).....	123
A.4 (a) Meso-structure distributions around (L)-dominated 4-node substructures. (b) Substructure distributions around (T)-dominated architectures.....	123
A.5 (a) Engineering tensile strain-stress diagram plotted with opening angle of (L) tile as tensile loading is applied. (b) Progression of (L) tile angle opening under tensile loading.....	124
A.6 Comparison of reinforcing network and composite failure locations under tensile loading. (a) (A) reinforcing network and (b) (A)-NRC showing the same failure locations. (c) (B) reinforcing network and (d) (B)-NRC showing the same failure locations.	124
A.7 (a) Simple tension experiment performed on VeroWhite and TangoBlack specimens. (b) Single edge notch tension (SENT) experiment performed on VeroWhite and TangoBlack specimens at a loading rate of 1mm/min. (c) Evolution of the crack position over time during the fracture of a VeroWhite-TangoBlack-VeroWhite specimen, confirming sequential events of crack arrest at the interface (I and II). The crack position has been retrieved by image analysis. ² (d) Digital Image Correlation (DIC) maps of the e_{yy} strain during the test reported in (c). The inset confirms the sequential formation of a plastic zone in the	

- VeroWhite portions subject to local yielding, as also observed in literature.^{2,3} (e) Optical photographs during a controlled fracture experiment (SENT geometry) of a network reinforced composite loaded at 1mm/min (initial crack length/specimen width ~ 0.5). Sequential details display the instantaneous propagation of a crack at small displacements internally to the first meso-structure, within the TangoBlack matrix (scale bar = 1 mm). Circular insets highlight the event of fracture arrest at the first soft to hard interface and the nucleation of a void in a nearby meso-structure. (f) Optical photographs highlighting the sequence of craze formation, fibril elongation and fracture within the TangoBlack matrix phase, internally to a meso-structure.125
- A.8 (a) Stress strain curves recorded on A-NRCs with a different reinforcement volume fraction V_R , ranging from 0.15 to 0.45. (b) Modulus of Toughness (MOT) as a function of the reinforcement volume fraction. (c) Optical photographs depicting the evolution of the fracture in specimens with increasing reinforcement volume fraction 0.15 (left), 0.30 (center) and 0.45 (right).126
- A.9 (Left) Optical photographs of composites with increasing reinforcement volume fraction V_R ranging from 0.15 to 0.45. The ligament thickness map is obtained with the plugin ‘local thickness’³ in the open-source image analysis software Fiji² and it is then overlaid on the images. (Right) Ligament thickness distribution for each specimen (bars), smoothing of the distributions measured for each specimen (solid lines).126
- A.10 (Left) Optical photographs of composites with increasing reinforcement volume fraction V_R ranging from 0.15 to 0.45. The ligament thickness map is obtained with the plugin ‘local thickness’³ in the open-source image analysis software Fiji² and it is then overlaid on the images. (Right) Ligament thickness distribution for each specimen (bars), smoothing of the distributions measured for each specimen (solid lines).127
- A.11 Variations in distribution of meso-structure sizes for (A)-NRCs and Mod-(A)-NRCs (left) and (B)-NRCs and Mod-(B)-NRCs (right), measured by image analysis.² Yellow, green, cyan and blue represent 4, 6, 8, and 10+ tiles meso-structures,

respectively, before (white bars) and after (red and blue bars) connectivity rule modifications.	127
A.12 Images (left) and digital image correlation maps (right) recorded at 0.5% strain of (A)* and (B)* composites (top and bottom, respectively).	128
B.1 DIC images and fracture nucleation images for composite samples with different matrix phases. (a) 2D DIC strain maps and fracture nucleation image for 2.3 coordination composite sample with Shore60 matrix. (b) 2D DIC strain maps and fracture nucleation image for 2.3 coordination composite sample with TangoBlack matrix. (c) 2D DIC strain maps and fracture nucleation image for 2.8 coordination composite sample with Shore60 matrix. (d) 2D DIC strain maps and fracture nucleation image for 2.8 coordination composite sample with TangoBlack matrix.	135
B.2 Maximum plastic zone size reached as a function of coordination number for 2.3, 2.5, and 2.8 samples.	136
B.3 Calculating the incremental J-integral as elastic and plastic components.	136
B.4 Plastic zone size, J integral and R-curves for bulk material samples. (a) Plastic zone area as a function of displacement for Grey60 and VeroWhite samples. S corresponds to start of the test, Y corresponds to time at yield, C corresponds to time at crack initiation, F corresponds to time at failure. (b) Incremental elastic J integrals (η_e normalized) and plastic J integrals (η_p normalized) as a function of displacement for Grey60 and VeroWhite samples. (c) R-curves for Grey60 and VeroWhite samples.	137
B.5 Structural feature characterization. (a) Structural feature area distributions for 2.3 coordination (top), 2.5 coordination (middle) and 2.8 coordination (bottom) samples. (b) Structural feature area profiles as a function of distance across the sample for 2.3 coordination (top), 2.5 coordination (middle) and 2.8 coordination (bottom) samples.	138
C.1 Simple tension experiment performed on VeroWhite and TangoBlack samples.	140

C.2 Radial distribution functions for various topologies.	140
C.3 Crack surface area opened as a function of tensile strain for various topologies.....	141
D.1 All orange pericarp cross sections from 0 mm to 5 mm into the fruit.	142
D.2 Concavity description. (I) Original orange pericarp image. (II) Selected feature. (III) Highlighted bridge length (red) and Euclidean distance (blue).....	142
D.3 Orange pericarp and VGA sample characterization. (a) Counts of structural feature areas for external region of orange pericarp. (b) Counts of structural feature areas for internal region of orange pericarp. (c) Counts of structural feature angle of orientation for external region of orange pericarp. (d) Counts of structural feature angle of orientation for internal region of orange pericarp. (e) Structural feature area plotted as a function of elliptic fit angle of orientation of structural features for external region of orange pericarp. (f) Structural feature area plotted as a function of elliptic fit angle of orientation of structural features for internal region of orange pericarp. (g) Counts of structural feature angle of orientation for external region of VGA sample. (h) Counts of structural feature angle of orientation for internal region of VGA sample. (i) Structural feature area plotted as a function of elliptic fit angle of orientation of structural features for external region of VGA sample. (j) Structural feature area plotted as a function of elliptic fit angle of orientation of structural features for internal region of VGA sample.	143
D.4 External region (left) and internal region (right) engineering stress-strain plot for 0-, 15-, 30-, and 45-degree rotated VGA samples.	144
D.5 Quasi-static compression tests. (a) Engineering stress-strain plot for graded and periodic honeycomb samples. (b) Example 2D DIC strain maps for 0%, 5%, and 10% global strain for graded honeycomb sample. (c) Example 2D DIC strain maps for 0%, 5%, and 10% global strain for periodic honeycomb sample.	145

D.6 Sample external and internal region combinations. Sample PNG's for 10% + 90%, 20% + 80%, and 50% + 50% (top). Compressive stress strain data for each variation (center). Coefficient of restitution for each variation (bottom).....	145
D.7 Wave speed propagation in composite materials. Sample with linear dot pattern and loading direction (left). Resliced image in time with dot trajectories over time as deformation reaches each dot (right).	146
E.1 Simple tension experiment performed on VeroWhite and TangoBlack samples.	153
E.2 Force-displacement plots for volume fraction equivalent periodic samples for coordinations 2X, 3X, 4X and 6X, respectively. Red refers to vertical matrix orientation, blue refers to horizontal matrix orientation.	153
E.3 Force-displacement plots for coordination 6X, zoomed in to show variation from sample orientation.	154
E.4 Angle of orientation of particles as a function of alignment and coordination number.	154
E.5 Cylindrical contact loading characterization. 2D DIC maps of all samples for ϵ_x strain (above) and ϵ_y strain (below).	155
E.6 2D DIC maps of equivalent volume fraction 6X samples for ϵ_x strain (above) and ϵ_y strain (below) at 1 mm cylindrical contact displacement.	156
E.7 Volume normalized fraction of matrix engaged as a function of coordination number at 1 mm cylindrical contact displacement for comparison of irregular samples and periodic equivalent 6X coordination samples.	157

Chapter 1

INTRODUCTION

1.1 Research Objectives

This thesis explores the mechanical characterization of irregular architected materials, using topological and geometrical descriptors to quantify structure-to-property relationships. The primary objectives of the research presented in this thesis are (i) to understand the relationship between irregularity and mechanical behavior in both linear and non-linear regimes, including fracture and dynamic impact, and (ii) to leverage this understanding to develop materials with spatially and temporally controllable mechanical responses. In order to achieve these objectives we developed a framework to design, fabricate and test materials with intentionally designed irregularity.

1.2 Motivation

Irregular materials are ubiquitous in biological and engineering applications. In nature, irregularity can be observed across many length scales in many materials including collagen^[1], enamel^[2,3], bone^[4-6], barnacle exoskeletons^[7], mussel adhesive^[8], fruit peels^[9], and termite nests^[10]. These materials all use their irregular structures to achieve excellent mechanical properties, including high stiffness, strength, toughness, and flexibility^[1,2,6,7,10-12]. For example, the irregular foam-like structure of trabecular bone achieves high stiffness- and high strength-to-weight ratios for a variety of loading conditions^[4,13], while the irregular arrangement of collagen fibrils in cortical bone increases compliance, which allows the material to better withstand fracture^[1]. Similarly, the irregular foam-like structure of citrus fruit peel allows the fruit to accommodate dynamic impact when it falls from the tree^[9]. Another example is the adhesive plaques and threads of mussels, which lack

ordered protein structures, allowing the animal to arrange them into a continuous gradient to better accommodate repeated loading from wave motion or predators^[7]. Irregularity can also be found in engineering materials, including in foams^[14–17], composites^[18,19], polymer networks^[20], and metal grain boundaries^[21,22]. These materials achieve excellent mechanical performances as a result of irregularity, such as how foams achieve high-stiffness and high strength-to-weight ratios while maintaining isotropy from their irregular cell shapes^[14], how particle-reinforced composites can achieve both isotropy and good creep and fatigue performances from the addition of randomly distributed particles^[23], and how metals can achieve high strength from misaligned grain boundary pile-ups^[21]. However, although these engineering materials feature irregularity, the irregularity is not intentionally designed and instead arises from stochastic fabrication processes. In contrast, the irregular biological materials developed their structures as a result of evolution, indicating that nature may favor designed irregularity for functionality^[7,24].

To bridge the gap, we then turn our attention to architected materials, which are defined as materials that are intentionally designed to offer a wide range of mechanical properties beyond that of their constitutive materials^[25–31]. However, most architected materials studied to date are periodic, as repeating unit cells are easy to design, fabricate and analytically model^[29,31–36]. Some methods to design irregular architected materials have been presented, including spinodal decomposition^[37–39], network pruning^[40] and Voronoi tessellations^[41–43], but these methods are generally stochastic with limited control over structural irregularity. Nonetheless, it has been shown that these irregular architected materials can offer a way to achieve a wider range of mechanical performances, including auxetic responses^[44,45], improved damage tolerance^[46,47], ductility^[48] and toughness^[49], as well as tailorable stiffness and strength^[10,50,51].

Given these benefits arising from irregularity, it is therefore of particular interest to understand how irregularity leads to the excellent mechanical properties. To do so, it is necessary to develop methods to generate irregular materials with greater control over descriptors of irregularity, such as topology, defined as how elements connect, and geometry, defined as the shape of elements, in order to understand and quantify the structure-to-property relationships. To achieve this, virtual growth algorithms (VGA) have been developed. These generative algorithms imitate the growth process of biological material structures by assembling a set of building blocks according to local connectivity rules^[10,50-52]. Unlike other methods, the VGA method offers control over both the underlying geometry and topology of the generated structure, through control of building block geometry and inclusion or exclusion of connectivity rules. In this thesis, we will use and expand these VGA methods to explore how topological and geometrical control over irregularity allows us to understand and quantify the structure-to-property relationships of irregular architected materials.

In order to experimentally characterize the VGA-generated samples, it is also necessary to consider fabrication methods. The VGA-generated samples are complex, with local variations in topology and geometry which must be accurately fabricated in the samples. It is therefore necessary to use additive manufacturing (AM) techniques to achieve this level of precise resolution. There is a wide variety of AM methods, such as stereolithography, material extrusion, multi-jet fusion and selective laser sintering. These methods can be used for a range of materials (although some are particular to a certain class of materials), including polymers, metals and ceramics^[53]. Although we briefly explore irregular 2D truss-based materials, our primary focus is on irregular composite materials, which feature two distinct phases, inspired by the composition of many natural materials. We therefore choose to fabricate our composite materials from polymers, using a multi-jet AM photoresin polymer method to simultaneously print multiple phases with the

desired resolution and macroscale sample size for mechanical characterization. Additional details about material properties and printing details are provided in each chapter according to the specific materials and sample dimensions.

1.3 Chapter Outlines

This thesis begins with an exploration of the mechanical characterization of irregular network reinforced polymer composites generated using a VGA. In Chapter 2, we first study the role of irregular topology and geometry on the mechanical response of the polymer composites, including the stiffness, strength, and modulus of toughness. With this understanding of the structure-to-property relationships, we show how to modify the irregular network reinforcement at the meso-scale to improve the global mechanical performance, creating assemblies of various network reinforcements with spatially-tuned fracture initiation and propagation. In Chapter 3, we expand the fracture characterization, obtaining J-integral and R-curve measurements by exploring the role of reinforcement and matrix materials as well as structural feature size and geometry in the irregular composites. In Chapter 4, we introduce a hexagonal VGA, which allows us to explore higher degree topologies and demonstrate the temporal response of the fracture behavior of the composites. In this chapter, we also study the effect of irregularity on damage tolerance, showing that introducing irregularity leads to improved damage tolerance.

We then further explore the intersection of irregular materials and bioinspiration. In Chapter 5, we present a materials design method using statistical measures of topology and geometry in natural materials to develop spatially tailorable materials with excellent energy absorption, inspired by citrus pericarp. In Chapter 6, inspired by tough and strong materials such as nacre and bone, we explore the inverse of the network reinforced composites. We present a class of bioinspired interlocking materials, and then demonstrate how to use irregularity to control the degree of

interlocking and strain energy distribution. Finally, in Chapter 7, we present a summary of the research in this thesis and discuss the potential future research directions.

1.4 Experimental Methods

To conduct the mechanical characterization and analysis of the irregular architected materials presented in this thesis, a variety of experimental methods are used across quasi-static and dynamic regimes for both linear and non-linear deformations.

1.4.1 Quasi-static Characterization

To conduct quasi-static testing of the materials, we use a universal testing machine (Instron E3000 (Instron, USA)) equipped with a 5 kN load cell, which has a resolution of 5 N. To apply tensile loading, we use a set of either 5 cm or 7.5 cm wide steel grips which fix the top and bottom of the sample and then we apply displacement-controlled loading at quasi-static loading rates varying from 1 mm/s to 5 mm/s, according to the particular application. To apply compression loading, we use a set of 5 cm diameter steel compression platens, position the sample in the center, and apply displacement-controlled loading at the desired strain rate. To apply cylindrical contact loading, we place samples on the bottom compression platen, position a 1 cm diameter cylindrical steel contact above the sample, and apply displacement-controlled loading at the desired strain rate. To record images of the tests, we use a Nikon D750 camera (Nikon, USA) with a Nikkor 120 mm f/4 lens (Nikon, USA) at frame rates from 1-5 frames per second, according to the particular material response. Additional details for each study conducted, including specific sample dimensions, experimental configurations, camera frame rates and strain rates, are provided in each chapter.

1.4.2 Fracture Characterization

We then go beyond the simple tension and compression testing to conduct fracture characterization of the irregular architected materials, which is of great interest to understand how irregularity can lead to improved fracture resistance. Although analytical solutions exist to describe the mechanical properties relevant to fracture (e.g. stiffness, yield strength, and toughness) of cellular solids, which resemble our network reinforced materials, these models rely on assumptions of stochasticity or periodicity^[33,35,54]. In contrast, our materials are irregular, but not stochastic, as the VGA method used to generate the samples has a limited set of building blocks and connectivity rules. Other structural descriptors, including the Maxwell number^[55], can give indications about the overall deformation mechanisms of a lattice material, such as if it is in a bending- or stretching-dominated regime, but these measures are unable to consider the effect of local variations in topology and geometry on the fracture response. Our materials are also composites, with two distinct phases, which further complicates the use of analytical models. To bridge the design space between stochastic and periodic structures and determine the effect of structural irregularity on the fracture response, we therefore conduct a full fracture characterization.

Using linear elastic fracture mechanics (LEFM), we first conduct single edge notch tension (SENT) tests on each phase of the irregular composite materials, to determine the Mode I fracture toughness of the constitutive materials^[56]. The toughness is calculated by:

$$K_{Ic} = \frac{P}{B\sqrt{W}} \cdot f\left(\frac{a}{W}\right), \quad (1)$$

where P is the applied load, B is the sample thickness, W is the sample width, a is the crack width, and $f\left(\frac{a}{W}\right)$ is given by:

$$f\left(\frac{a}{W}\right) = \frac{\sqrt{2 \cdot \tan \frac{\pi a}{2W}}}{\cos \frac{\pi a}{2W}} \left[0.752 + 2.02 \frac{a}{W} + 0.37 \left(1 - \sin \frac{\pi a}{2W} \right) \right]. \quad (2)$$

We also conduct SENT tests on laminate samples to determine that the interfacial toughness between the reinforcing network and matrix phases is greater than that of the matrix phase. All of these force displacement curves are provided and further discussed in Chapter 2 and Appendix A.

With an understanding of the fracture response of the individual phases, in Chapter 2, we then conduct plate tension tests on the composite materials and obtain values for the modulus of toughness (MOT), in order to relate it to variations in the irregular reinforcing networks. The MOT is defined as

$$MOT = \int \sigma d\varepsilon, \quad (3)$$

where σ is the stress and ε is the strain, resulting in a measure of energy per unit volume of material. Although the MOT tells us how much energy the material is able to dissipate prior to rupture, it is also important to characterize the fracture response of the material with consideration of size effects as well as effects beyond the elastic regime, including plasticity. To do this, we conduct SENT tests on irregular network reinforced composites and use measures of the J-integral to obtain R-curves. Chapter 3 explores the effect of irregularity on R-curve shape and breaks down contributions of elastic and plastic deformation, relating topology and geometry to the fracture response.

1.4.3 Dynamic Characterization

The dynamic response of the irregular architected composites is also of interest to understand the effect of irregularity on mechanical properties at higher strain rates.

It has been shown that introducing irregularity into cellular architected materials can lead to improved mechanical performances and isotropy at dynamic strain rates, with damage delocalization^[57-59]. Here, we expand this characterization to our irregular network reinforced composite materials, using a drop tower apparatus to explore dynamic strain rates up to 100 s^{-1} . The drop tower consists of an aluminum tube with wall thickness of 0.3 cm, inner diameter of 2.7 cm, and height of 3 m, attached to a steel frame. A 10 cm steel striker with a diameter of 2.5 cm and a mass of $\sim 400 \text{ g}$ is released and falls down the tube to impact the sample, positioned and glued at the base. A photodiode placed at the base of the tube, just above the sample, captures the moment the striker passes the bottom of the tube, and is used to trigger a high speed camera (Phantom v1610, Vision Research, AMETEK, USA), which captures images of the event at frame rates up to 1 million frames per second. A schematic of the drop tower is provided in Figure 1.1. The striker can reach velocities up to 7-8 m/s, which can be measured both from high speed camera images and calculated from the energy balance of potential and kinetic energy, given the drop tower height of 3 m:

$$v = \sqrt{2gh}, \quad (4)$$

where v is the velocity, h is the height and g is the gravitational constant.

We can then quantify the energy absorption of the samples using the coefficient of restitution (CR), measured from the high speed camera images of striker position through time:

$$CR = \frac{v_f}{v_i}, \quad (5)$$

where v_f is the striker velocity after impact and v_i is the striker velocity before impact.

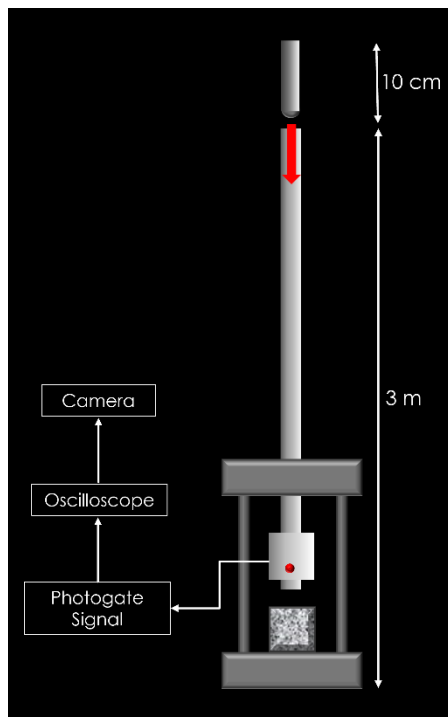


Figure 1.1: Drop tower configuration.

1.4.4 Digital Image Correlation

To non-invasively measure the deformation of the materials during loading, we use 2D digital image correlation (DIC). DIC uses image analysis to track the surface deformation of a continuous material across a set of images and can provide information about displacement, strain and rigid body motion. To conduct DIC, a high-contrast random speckle pattern is uniformly applied to the surface of the object of interest. The pattern should be sufficiently dense, containing about 50% dark and 50% light speckles, and the speckles should be large enough to take up between 3×3 and 7×7 pixels of the camera image. The speckle pattern should also be able to deform with the material of interest, and a wide range of speckling

techniques are available, including spray paint, ink, and particle deposition. In order to obtain the information about the material deformation and motion, there are two common DIC techniques: global DIC and local DIC. While global DIC examines the entire material's deformation simultaneously, local DIC tracks subsets of speckles independently, making it less computationally expensive^[60]. The choice of speckle size and subset size is therefore critical to obtain accurate measurements and must be tailored to the particular material and test. The specific details of the DIC techniques used, including speckling method, speckle size, subset size, step size, and strain measures are further discussed in each chapter and corresponding appendices.

BIBLIOGRAPHY

- [1] N. Reznikov, R. Almany-Magal, R. Shahar, S. Weiner, *Bone* **2013**, *52*, 676.
- [2] E. Beniash, R. A. Metzler, R. S. K. Lam, P. U. P. A. Gilbert, *J Struct Biol* **2009**, *166*, 133.
- [3] N. Reznikov, M. Bilton, L. Lari, M. M. Stevens, R. Kröger, *Science* **2018**, *360*.
- [4] T. M. Keaveny, E. F. Morgan, G. L. Niebur, O. C. Yeh, **2003**, *3*, 307.
- [5] W. J. Whitehouse, *J Microsc* **1974**, *101*, 153.
- [6] N. Kumar, A. Kumar, P. Uniyal, B. Ramalingaiah, S. Sharma, V. G. Goni, S. Aggarwal, S. K. Bhadada, B. Bhushan, *Philosophical Transactions of the Royal Society A* **2020**, *378*.
- [7] R. A. Metzler, F. Barthelat, J. J. Wilker, *Adv Funct Mater* **2019**, *29*, 1805734.
- [8] D. G. DeMartini, J. M. Errico, S. Sjoestroem, A. Fenster, J. H. Waite, *J R Soc Interface* **2017**, *14*.
- [9] M. Thielen, C. N. Z. Schmitt, S. Eckert, T. Speck, R. Seidel, *Bioinspir Biomim* **2013**, *8*.
- [10] K. Liu, R. Sun, C. Daraio, *Science* **2022**, *377*, 975.
- [11] A. Heyde, L. Guo, C. Jost, G. Theraulaz, L. Mahadevan, *Proc Natl Acad Sci* **2021**, *118*, e2006985118.
- [12] K. J. Koester, J. W. Ager, R. O. Ritchie, *Nat Mater* **2008**, *7*, 672.
- [13] R. Oftadeh, M. Perez-Viloria, J. C. Villa-Camacho, A. Vaziri, A. Nazarian, *J Biomech Eng* **2015**, *137*, 0108021.
- [14] M. F. A. L. J. Gibson, *Cellular Solids: Structure and Properties*, Cambridge Univ. Press, **1999**.
- [15] M. Alkhader, M. Vural, *Int J Eng Sci* **2008**, *46*, 1035.
- [16] A. P. Roberts, E. J. Garboczi, *Acta Mater* **2001**, *49*, 189.
- [17] M. J. Silva, L. J. Gibson, *Int J Mech Sci* **1997**, *39*, 549.

- [18] J. Njuguna, Ed., *Lightweight Composite Structures in Transport* **2016**, 1.
- [19] E. Kröner, *J Mech Phys Solids* **1967**, *15*, 319.
- [20] V. Sorichetti, A. Ninarello, J. M. Ruiz-Franco, V. Hugouvieux, W. Kob, E. Zaccarelli, L. Rovigatti, *Macromolecules* **2021**, *54*, 3769.
- [21] H. Van Swygenhoven, D. Farkas, A. Caro, *Physical Review B* **2000**, *62*, 831.
- [22] T. Watanabe, *Metallurgical transactions. A, Physical metallurgy and materials science* **1982**, *14 A*, 531.
- [23] N. Chawla, Y. L. Shen, *Adv Eng Mater* **2001**, *3*, 357.
- [24] P. Fratzl, *J R Soc Interface* **2007**, *4*, 637.
- [25] L. R. Meza, A. J. Zelhofer, N. Clarke, A. J. Mateos, D. M. Kochmann, J. R. Greer, *Proc Natl Acad Sci U S A* **2015**, *112*, 11502.
- [26] K. M. Conway, C. Kunka, B. C. White, G. J. Pataky, B. L. Boyce, *Mater Des* **2021**, *205*, 109696.
- [27] Y. Wang, B. Ramirez, K. Carpenter, C. Naify, D. C. Hofmann, C. Daraio, *Extreme Mech Lett* **2019**, *33*, 100557.
- [28] L. R. Meza, G. P. Phlipot, C. M. Portela, A. Maggi, L. C. Montemayor, A. Comella, D. M. Kochmann, J. R. Greer, **2017**.
- [29] M. R. O'Masta, L. Dong, L. St-Pierre, H. N. G. Wadley, V. S. Deshpande, *J Mech Phys Solids* **2017**, *98*, 271.
- [30] H. C. Tankasala, N. A. Fleck, *Int J Solids Struct* **2020**, *188–189*, 233.
- [31] V. S. Deshpande, N. A. Fleck, M. F. Ashby, *J Mech Phys Solids* **2001**, *49*, 1747.
- [32] L. R. Meza, S. Das, J. R. Greer, *Science (1979)* **2014**, *345*, 1322.
- [33] L. J. Gibson, M. F. Ashby, *Proc R Soc Lond A Math Phys Sci* **1982**, *382*, 43.
- [34] S. K. Maiti, M. F. Ashby, L. J. Gibson, *Scripta Metallurgica* **1984**, *18*, 213.
- [35] L. J. Gibson, M. F. Ashby, G. S. Schajer, C. I. Robertson, *Proc R Soc Lond A Math Phys Sci* **1982**, *382*, 25.
- [36] V. S. Deshpande, M. F. Ashby, N. A. Fleck, *Acta Mater* **2001**, *49*, 1035.

- [37] M. T. Hsieh, B. Endo, Y. Zhang, J. Bauer, L. Valdevit, *J Mech Phys Solids* **2019**, *125*, 401.
- [38] Y. Zhang, M. T. Hsieh, L. Valdevit, *Compos Struct* **2021**, *263*, 113693.
- [39] A. Guell Izard, J. Bauer, C. Crook, V. Turlo, L. Valdevit, A. Guell Izard, J. Bauer, L. Valdevit, C. Crook, V. Turlo, *Small* **2019**, *15*, 1903834.
- [40] D. Rayneau-Kirkhope, S. Bonfanti, S. Zapperi, *Appl Phys Lett* **2019**, *114*.
- [41] H. X. Zhu, A. H. Windle, *Acta Mater* **2002**, *50*, 1041.
- [42] H. X. Zhu, J. R. Hobdell, A. H. Windle, *Acta Mater* **2000**, *48*, 4893.
- [43] K. Li, X. L. Gao, J. Wang, *Int J Solids Struct* **2007**, *44*, 5003.
- [44] M. J. Mirzaali, H. Pahlavani, A. A. Zadpoor, *Appl Phys Lett* **2019**, *115*, 21901.
- [45] D. R. Reid, N. Pashine, J. M. Wozniak, H. M. Jaeger, A. J. Liu, S. R. Nagel, J. J. De Pablo, *Proc Natl Acad Sci U S A* **2018**, *115*, E1384.
- [46] K. Li, X. L. Gao, G. Subhash, *Int J Solids Struct* **2005**, *42*, 1777.
- [47] M. S. Pham, C. Liu, I. Todd, J. Lertthanasarn, *Nature* **2019**, *565*:7739 **2019**, *565*, 305.
- [48] D. Tüzes, P. D. Ispánovity, M. Zaiser, *Int J Fract* **2017**, *205*, 139.
- [49] S. Fulco, M. K. Budzik, H. Xiao, D. J. Durian, K. T. Turner, *PNAS Nexus* **2025**, *4*.
- [50] R. Wang, Y. Bian, K. Liu, *J Appl Mech* **2025**, *1*.
- [51] Y. Jia, K. Liu, X. S. Zhang, *J Mech Phys Solids* **2024**, *192*, 105787.
- [52] Y. Jia, K. Liu, X. S. Zhang, *Comput Methods Appl Mech Eng* **2024**, *425*, 116864.
- [53] I. Gibson, D. Rosen, B. Stucker, M. Khorasani, *Additive Manufacturing Technologies* **2020**, *1*.
- [54] S.K. Maiti, M. F. Ashby, L. J. Gibson, *Scripta Metallurgica* **1984**, *18*, 3.
- [55] J. C. M. F.R.S., *The London, Edinburgh, and Dublin Philosophical Magazine and Journal of Science* **1864**, *27*, 294.
- [56] T. L. Anderson, *Fracture Mechanics: Fundamentals and Applications*, 3rd

- ed.*, CRC Press, Boca Raton, FL **2005**.
- [57] K. Li, X. L. Gao, G. Subhash, *Int J Solids Struct* **2005**, *42*, 1777.
- [58] A. Ajdari, H. Nayeb-Hashemi, A. Vaziri, *Int J Solids Struct* **2011**, *48*, 506.
- [59] H. X. Zhu, A. H. Windle, *Acta Mater* **2002**, *50*, 1041.
- [60] E.M.C Jones, M.A. Iadicola, *A Good Practices Guide for Digital Image Correlation* **2018**.

*Chapter 2***CONTROL OF MECHANICAL AND FRACTURE PROPERTIES
IN TWO-PHASE MATERIALS REINFORCED BY CONTINUOUS,
IRREGULAR NETWORKS**

T. Magrini, C. Fox, A. Wihardja, A. Kolli & C. Daraio, (2023). “Control of Mechanical and Fracture Properties in Two-Phase Materials Reinforced by Continuous, Irregular Networks”. *Advanced Materials* 36 (6), 2305198.
doi: 10.1002/adma.202305198.

C.F. participated in the design, fabrication, and testing of samples, data analysis and visualization, and in writing and revising the manuscript.

Chapter Abstract

Composites with high strength and high fracture resistance are desirable for structural and protective applications. Most composites, however, suffer from poor damage tolerance and are prone to unpredictable fractures. Understanding the behavior of materials with an irregular reinforcement phase offers fundamental guidelines for tailoring their performance. Here, the fracture nucleation and propagation in two-phase composites is studied as a function of the topology of their irregular microstructures. A stochastic algorithm is used to design the polymeric reinforcing network, achieving independent control of topology and geometry of the microstructure. By tuning the local connectivity of isodense tiles and their assembly into larger structures, the mechanical and fracture properties of the architected composites are tailored at the local and global scale. Finally, combining different reinforcing networks into a spatially determined meso-scale assembly, it is demonstrated how the spatial propagation of fracture in architected composite materials can be designed and controlled a priori.

2.1 Introduction

Composite materials offer many advantages over traditional materials, such as being lightweight while maintaining a high strength and stiffness^[1, 2], but they suffer from lack of toughness and poor damage tolerance^[3-6]. One way to improve their crack response is to tailor the reinforcing phase architecture^[7-10]. Fiber reinforcements, for example, exploit crack bridging between fibers for toughening. Introducing fibers and other high-aspect-ratio reinforcing elements in the design of composite materials often leads to direction-dependent mechanical properties and anisotropic fracture resistance^[11]. Depending on the reinforcing elements' alignment direction, composites can be either toughened by high fracture energy dissipative mechanisms, such as fiber bridging and fiber pullout, or be subject to delamination fractures, which occur at the fiber-matrix interface^[11-14]. On the contrary, randomly distributed inclusions, which primarily toughen the material through microcracking and secondary crack formation, often lead to composite materials with isotropic fracture properties^[15-17]. Developing materials that use multiple toughening mechanisms, like bridging, deflecting, or even arresting the propagation of cracks, has the potential to improve the amount of absorbed fracture energy. This was recently demonstrated in bioinspired architected composites, where the internal microstructure was finely tailored to control crack propagation behavior^[18, 19]. The combination of multiple toughening mechanisms can also be achieved by fabricating composite materials with irregular reinforcing networks^[20, 21]. Irregular microstructures are common in biological structural materials^[22-25] and understanding their behavior during loading and fracture is relevant for the design of architected materials with tailored load-bearing performance. Irregular networks can control the fracture and toughening behavior of materials through the creation of meso-scale structures with different dimensions and orientations that cause multiple fracture nucleation and propagation events. Finally, reinforcing composites with irregular networks allows the creation of materials with direction-independent mechanical properties, a desirable feature in structural and load-

bearing applications. Here, we describe how network coordination influences the global mechanical properties of two-phase materials, like strength, stiffness, and energy dissipated during fracture, as well as the role of local mechanisms on fracture nucleation and propagation. Introducing desired irregular networks as composite reinforcement and achieving a fine control over their assembly across multiple length scales, from the micro- to the centimeter-scale, requires advances in both numerical design and manufacturing. In recent work, machine-learning and data-driven approaches were used to computationally design hierarchical architected materials^[26]. Here, we employ algorithms that “grow” regular and irregular networks^[27] for composite design and use multi-material additive manufacturing processes for fabrication.

2.2 Design of Irregular Reinforcement

To design the stiff reinforcement phase of our two-phase composites, we utilized a virtual growth algorithm (Appendix A.3.1), which tessellates a set of bimaterial tiles on a discretized spatial grid, following a set of connectivity rules^[22]. We used a combination of 2-coordinated tiles ([L] and [-]) and 3-coordinated tiles ([T]) and ensured that each tile had the same volume fraction of stiff reinforcing phase and soft matrix phase (Figure 2.1a, left). We combined these tiles to generate composites with a stiff reinforcing irregular network (white) and a soft elastomeric matrix (black) (Figure 2.1a, right). The virtual growth algorithm ensures continuity between the two phases through modifiable connectivity rules (Figure A.1). Depending on the relative composition of 2- and 3-coordinated tiles, the virtual growth algorithm creates various composites with the same volume fraction of reinforcement, but a large ternary design space (Figure 2.1b). We expect the shape and directional tile connectivity to influence the local deformation mechanisms accessible within the clusters, with [L] shaped tiles showing bending-dominated local deformations and straight [-] tiles showing stretching-dominated behaviors.

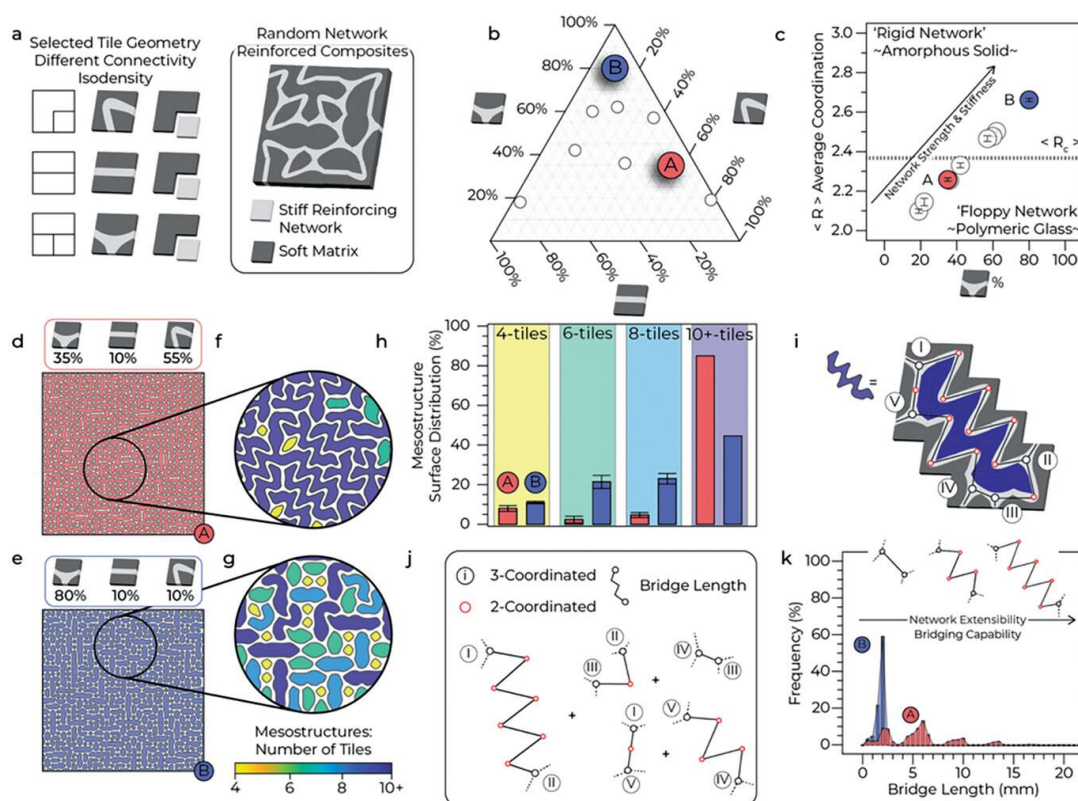


Figure 2.1: Architecture of two-phase materials. (a) Selected isodensity tile geometries and composite assembly. (b) Compositional design space in a ternary diagram. (A) and (B) architectures are represented by red and blue circles, respectively. (c) Average coordination $\langle R \rangle$ as a function of [T] tiles content. (A) and (B) reinforcing networks are represented by red and blue circles, respectively. (d,e) Representative (A) and (B) architectures (d and e, respectively). (f,g) Close-up view of meso-structures that populate (A) and (B) architectures in (d) and (e), respectively. Yellow, green, cyan, and blue represent 4, 6, 8, and 10+ tiles meso-structures, respectively. (h) Meso-structure distributions in (A) (red bars) and (B) architectures (blue bars). (i) Example of meso-structure with labeled coordination and bridges. (j) Expanded version of (i). (k) Comparison of bridge length and their frequency for (A) and (B) architectures (red and blue, respectively).

2.3 Network Characterization

We evaluate the properties of the reinforcing networks using frameworks developed to describe covalent random networks (Appendix A.3.2), at two hierarchical scales. At the global scale, we evaluate the average coordination of the materials at constant density, and at the local scale, we analyze how growth rules affect the

formation of characteristic meso-structures. We evaluate the average coordination $\langle R \rangle$ in the reinforcing networks, accounting for the presence of dangling bonds, unconnected ligaments at the network edges (Figure 2.1c)^[28, 29]. Scaling linearly with the volume fraction of 3-coordinated tiles, we expect $\langle R \rangle$ to influence the global mechanical properties, like strength and stiffness, as reported in other amorphous material systems^[30-32]. To understand the effect of the reinforcing network architecture on the composite properties, we compare two different compositions with significantly different average coordination: (A)-networks (35 [T], 10 [-], 55 [L]), dominated by 2-coordinated tiles and floppy modes; and (B)-networks (80 [T], 10 [-], 10 [L]), dominated by 3-coordinated tiles and that are purely rigid (Figure 2.1b,c, red and blue circles, respectively).

Despite having the same reinforcing and matrix phase volume fractions, (A)- and (B)-network reinforced composites (NRC's) form different local meso-structures, defined as the matrix domains enclosed by reinforcing network (Figure 2.1d,e). While the average coordination of the reinforcing network explains the global mechanical behavior of the materials, studying the meso-structures that pattern each composite is key to understand their local properties. First, the meso-structures are categorized and mapped based on size and number of constitutive tiles (Figure 2.1f,g). Then, their surface distribution is used to indicate the texture of (A)- and (B)-NRC's (Figure 2.1h). Additionally, the number density of each meso-structure (Figure A.2), their angle of orientation (Figure A.3), and the effect that small meso-structures have on their surroundings (Figure A.4) are important descriptors of these architected composites.

We characterize the reinforcing networks by drawing parallels with the concept of network bridges, often used in studying of the mechanical performance of covalent random networks^[28, 29]. A bridge (black solid lines, Figure 2.1i,j) connects two 3-coordinated tiles, considered anchored in the network (I–V white circles, Figure

2.1i,j). It was demonstrated that a bridge composed of six or more 2-coordinated tiles (red circles, Figure 2.1i,j) forms a floppy region within the network^[28, 29]. The presence of floppy domains in a stiff, yet deformable, reinforcing network influences the local mechanical composite performance, resulting in a globally more extensible and deformable material (Figure A.5). In this context, the presence of an incompressible matrix phase is important to prevent large bridge deformations. Because of the different content of 3-coordinated tiles, (A)-NRC's display a multimodal distribution of bridge lengths, which are significantly longer than those of (B)-NRC's (Figure 2.1k).

2.4 Mechanical Properties

Although (A)- and (B)-NRC's have the same volume fraction of reinforcement and matrix phases, the difference in average coordination, bridge length, and different meso-structure populations influence the mechanical properties at both global and local scales. To measure experimentally the mechanical properties of the chosen architectures, we additively manufactured composite samples using a polyjet printer (Stratasys Objet500 Connex3). Recent studies have focused on experimentally determining the mechanical and physical properties of objects printed by polyjet printing and shed light on the relationship between the printing parameters and the final performance of the part^[33-35]. In our study, a stiff viscoelastic resin (VeroWhite Polyjet Resin) and a soft elastomeric resin (TangoBlack Polyjet Resin) were chosen for the reinforcing phase and matrix phase, respectively. Both resins are commercially available, and their constitutive properties fall within ranges reported in literature (Figure A.7)^[18, 36-38]. We combined these two materials in a polymer composite with a volume fraction of reinforcing phase of 0.3. At this volume fraction, we observed that the composites display a desired tradeoff between rigidity and extensibility (Figure A.8), while the reinforcing network thickness is one order of magnitude larger than the polyjet printer resolution limit (Figure A.9). To characterize their mechanical response, we

performed plate tension experiments and confirmed that at the global scale, the purely rigid-like (B)-NRC's achieve higher strength and higher stiffness than the (A)-NRC's (Figure 2.2a,b).

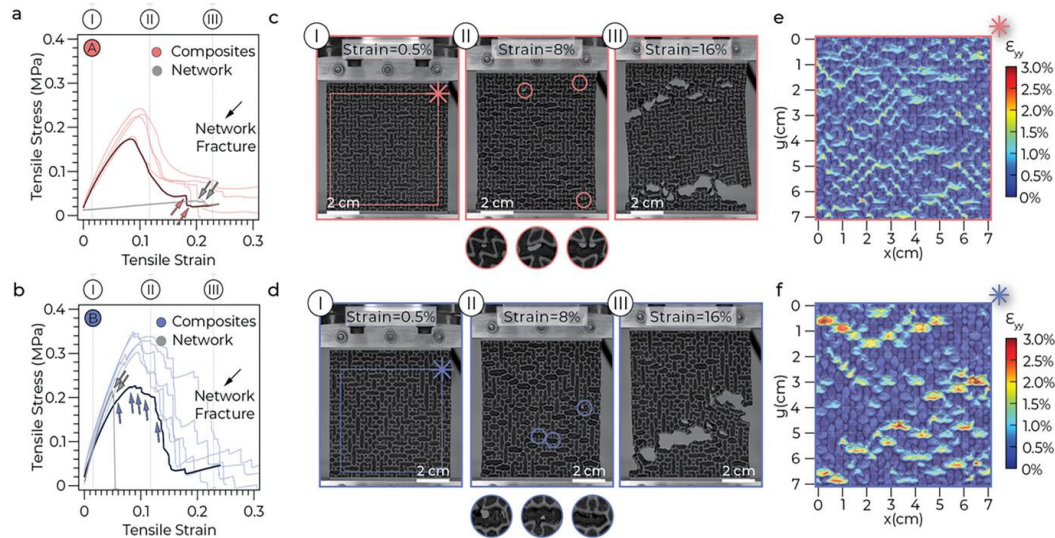


Figure 2.2: Mechanical characterization of composites. (a,b) Engineering stress–strain curves recorded during uniaxial tension tests on plate geometries of (A)-NRC's and (B)-NRC's (red solid lines in a, blue solid lines in b, respectively). The solid black lines in (a,b) represent the response of samples photographed in (c,d), respectively. The solid gray lines in (a,b) represent the response of the same (A)-NRC and (B)-NRC samples, without the matrix phase. Fracture events in the reinforcing phase of (A)-NRC's and (B)-NRC's are indicated by red and blue arrows in (a) and (b), respectively, and in the reinforcing networks by gray arrows (see also Figure A.6). (c,d) Fracture evolution in representative samples of (A)-NRC and (B)-NRC, respectively. The circles indicate the locations within the samples that display the signs of voids growth (circles in (c) and (d), frame II and insets in (c) and (d), frame II, bottom). (e,f) Digital image correlation (DIC) maps of the representative samples of (A)-NRC and (B)-NRC recorded at 0.5% strain (e and f, respectively). The DIC maps refer to the areas of samples highlighted by (*) in frame I of (c) and (d).

Despite a significant difference in the global mechanical properties, the composites display similarities in the local scale mechanisms that determine the initiation and propagation of fractures. Due to the remarkable adhesion properties between the two resins used in this study^[39], fracture initiation does not occur at the interface

between the matrix and the reinforcing network, in either pristine or pre-notched samples, but within the matrix (Figure A.7). Void nucleation in the matrix phase initiates the composite fracture process, similar to the ductile fracture of metals^[40]. Void formation is followed by matrix detachment from the reinforcing network, resulting in steady void growth (Figure 2.2c,d, I to III, respectively). In this propagation phase, the void growth and coalescence are hindered by the reinforcing network bridges, which elongate as the sample undergoes tensile loading. Thus, the average bridge length and extensibility before rupture become paramount, as these characteristics predict the strain of the reinforcing network before failure (Appendix A.3.3). After the sequential failure of the bridges (Figure 2.2a,b, red and blue arrows, respectively), we observe the complete loss of composite integrity.

The local composite architecture becomes key during failure, as strain localization in selected meso-structures leads to fracture nucleation and growth, as confirmed by 2D digital image correlation (DIC) at small strains (Figure 2.2e,f). Therefore, to design composites capable of dissipating the most fracture energy, one must act on both the global and local scale, tailoring the network rigidity and generating local meso-structures, to avoid localized strain fields. To achieve this, we modify the connectivity rules of the growth algorithm.

We changed the connectivity rules of the growth algorithm to increase energy dissipation during fracture in composites. By amending four tile connectivity rules (Figure 2.3a, top; Appendix A.3.4, Figure A.10), we prevented the formation of large floppy domains, which increased network rigidity, stiffness, and strength. The modified networks displayed a purely rigid-like behavior, as shown by their higher average coordination than the original networks (Figure 2.3a, bottom). We tested the effect of the modified reinforcing networks on the composites' mechanical performance and fracture energy dissipation through plate tension experiments. As a result of their higher coordination, modified-(A)-network reinforced composites

(Mod-(A)-NRC's) displayed higher ultimate tensile strength (UTS) and up to 60% increase in tensile stiffness (Figure 2.3b red and gray solid lines, respectively), while modified-(B)-network reinforced composites (Mod-(B)-NRC's) had a 5% reduction in stiffness as a result of the slightly lower average coordination (Figure 2.3e blue and gray solid lines, respectively). Although each composite begins failure at $\approx 10\%$ tensile strain, the modified designs' damage tolerance dramatically improved. At high tensile strain (up to $\approx 16\%$), the Mod-NRC's carry a load of $\approx 70\text{--}80\%$ their UTS (Figure 2.3c,d,f,g). As a comparison, their original counterparts at the same tensile strain had completely lost any load bearing capabilities, due to presence of sample-scale cracks and coalesced voids, resulting from the extensive failure of the reinforcing phase. Conventional calculations of the stress intensity factor and local stress concentration field require making assumptions based on continuum mechanics: for composite materials, the reinforcing feature sizes must be small compared to the size of the singularity zone, and the non-linear damage must be confined to a small region within the singularity zone^[40]. In our irregular composites, these conditions are not satisfied; meso-structures sizes are in the order of several mm (Figure A.2) and crack nucleation occurs in multiple locations within the microstructure (Figure 2.2c,d; Figure 2.3d,g). In the present study, to highlight how these simple modifications to the reinforcing networks influence significantly the energy dissipated during fracture, we measured the modulus of toughness (MOT), taken as the area under the stress–strain curve. Modifying the reinforcing networks in (A) and (B) composites improved the total dissipated energy during fracture of up to $\approx 130\%$ and $\approx 60\%$, respectively (Figure 2.3b,e, top).

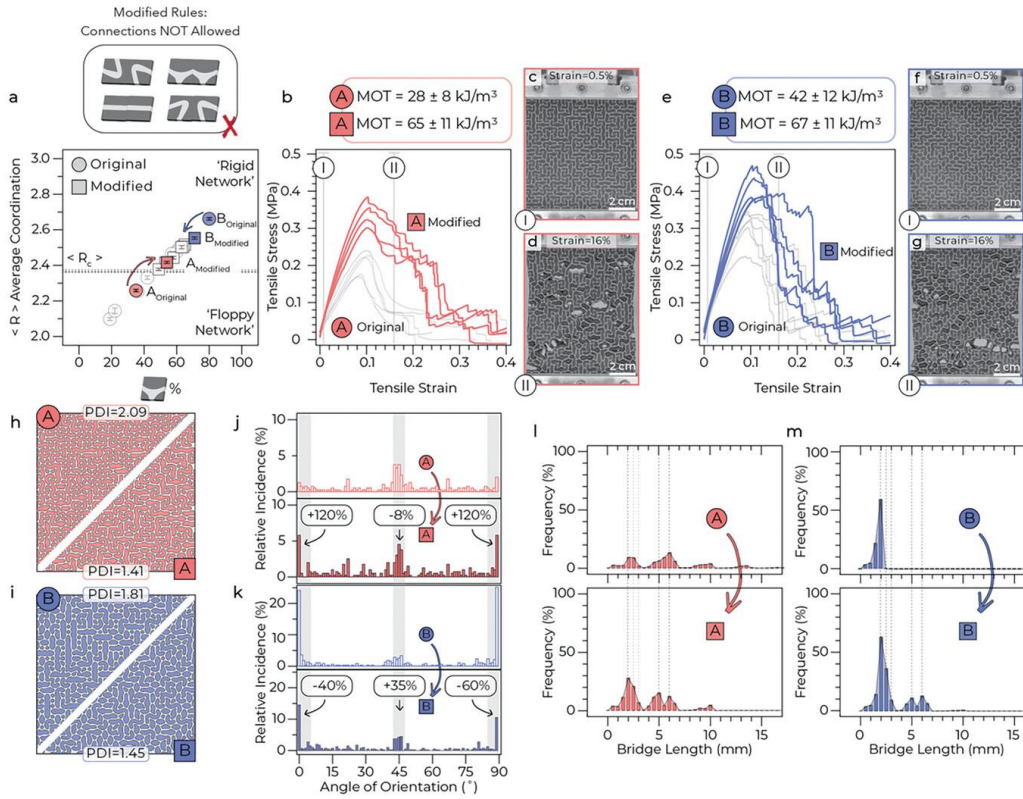


Figure 2.3: Modified composites and their performance. (a) Modifications of connectivity rules and average coordination number as a function of [T] tiles (top and bottom, respectively). (b) Engineering stress–strain diagram of Mod-(A)-NRC's (red solid lines) and of original (A)-NRC's (gray solid lines). The modulus of toughness (MOT) is reported for both composites at the top of the diagram. (c,d) Fracture evolution in representative Mod-(A)-NRC at 0.5% and 16% strain (c and d, respectively). (e) Engineering stress–strain diagram of Mod-(B)-NRC's (blue solid lines) and of the original (B)-NRC's (gray solid lines). The MOT is reported for both composites at the top of the diagram. (f,g) Fracture evolution in representative Mod-(B)-NRC at 0.5% and 16% strain (f and g, respectively). (h,i) Modification of microstructure of (A)- and (B)-networks (h and i, respectively) and measured polydispersity index (PDI) for each network. (j,k) Variation in relative meso-structure orientation distribution of (A) and (B)-networks (j and k, respectively). (l) Frequency of bridge lengths for (A)- and Mod-(A)-networks (top and bottom, respectively). (m) Frequency of bridge lengths for (B)- and Mod-(B)-networks (top and bottom, respectively).

Considering only global scale descriptors, like the average reinforcing network coordination, is insufficient to explain the higher strength of Mod-(B)-NRC's

compared to (B)-NRC's. Thus, we evaluated the modified designs at the local scale, to investigate the effect that simple modifications of the connectivity rules had on the meso-structures. First, we notice by visual inspection that the modified composites (Figure 2.3h,i, bottom) have a significantly different internal structure than their original counterparts (Figure 2.3h,i, top). The modified architectures feature a more homogeneous distribution of meso-structures, which are quantified through the polydispersity index (PDI) (Figure 2.3h,i; Appendix A.3.5). The decrease in PDI by 33% for (A)-NRC's and by 20% for (B)-NRC's, confirms that more stringent connectivity rules homogenize and coarsen the meso-structures sizes (Figure A.11). Furthermore, the modified composites feature meso-structures that display a more homogeneous angle of orientation with respect to their original counterparts (Figure 2.3j,k). As a result of the more homogeneous size and orientation distribution of domains, the modified composites are subject to a more homogeneous distribution of the deformation during loading, preventing high strain localization (Figure A.12) and leading to the multiple uniformly distributed void nucleation sites in the matrix (Figure A.3d,g). Finally, we evaluated the effect of the modifications on bridges length distributions. In Mod-(A)-NRC's, the increase in short bridges confirms that the newly generated networks are more constrained and thus rigid, compared to their original counterparts (Figure 2.3l). Conversely, Mod-(B)-networks have a distribution of bridge lengths that shifts toward larger sizes and becomes multimodal, becoming like those of (A)-networks, suggesting the generation of reinforcing networks with higher local extensibility and hence, higher bridging capability (Figure 2.3m).

We developed a method to control crack trajectory in network reinforced composites by creating hierarchical microstructures that combine local rules, meso-scale assemblies, and macroscale connectivity networks at a constant density. We drew inspiration from biological composites like mother-of-pearl^[41-45] and cortical bone^[46-48], which deflect incoming cracks and dissipate fracture energy. Our meso-

scale assemblies feature rational designs of “strong and tough” network portions combined with “soft” network portions. We created two laminate configurations with complementary meso-scale arrangements (Figure 2.4a I and b I, respectively) and found that the (A)-NRC's domains carry most of the strain regardless of their spatial arrangement. For an applied 0.5% strain, (A)-NRC's domains are subject to ~0.8% strain whereas Mod-(B)-NRC's domains experience as little as 0.3% strain (Figure 2.4c,d). We can thus control the fracture trajectory through domain assembly, since fracture nucleates (Figure 2.4a II,b II) and propagates (Figure 2.4a III,b III) in “soft” domains. These properties are also consistent with crack propagation observed in single edge notch tension tests (SENT) (Figure A.7). We take inspiration from the cross section of cortical bone, composed of tightly packed osteons enveloped by the cement lines, specifically designed to arrest and guide incoming cracks on tortuous trajectories^[49-51] (Figure 2.4e). In our cortical bone-inspired assembly, we embedded strong and tough osteon-inspired high coordination domains in a floppy and low coordination matrix domain (Figure 2.4f). At 7% strain, it is already visible how the strain localizes in the floppy portions of the composite (Figure 2.4g), leading to fracture nucleation in the central matrix area (left side, Figure 2.4h), that is then arrested as it approaches the opposite osteon-domain (right side, Figure 2.4h). Meanwhile, crack nucleation above and below the plane of propagation initiates the desired process of renucleation and redirection of the fracture, critical to deflect its trajectory (red arrows, Figure 2.4h) and to successfully shield the osteon domains (Figure 2.4i).

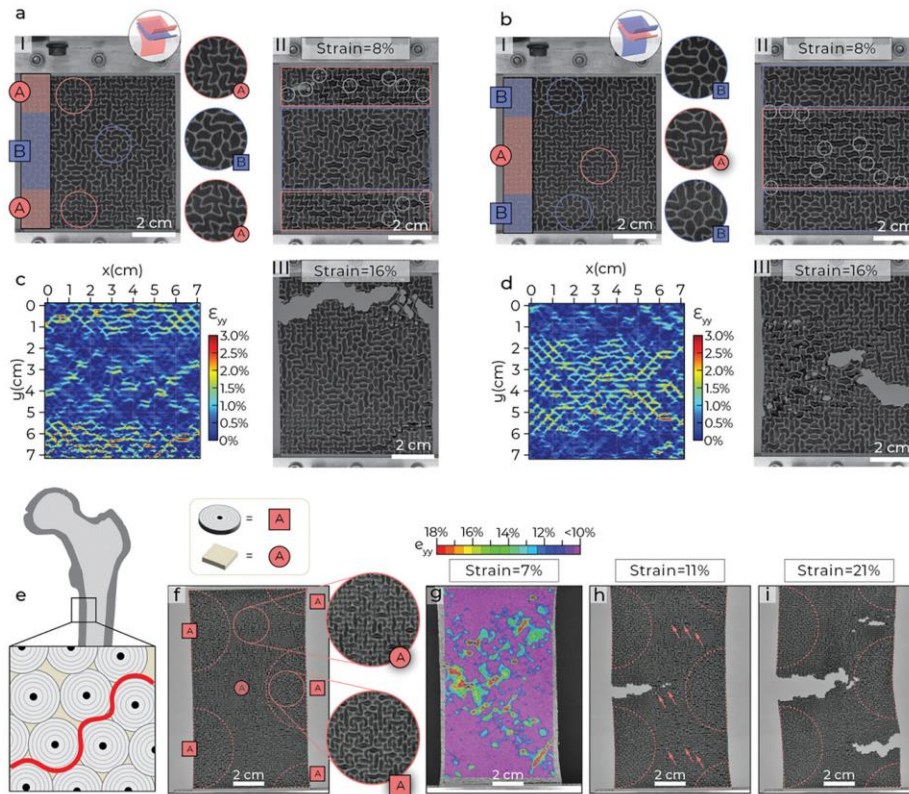


Figure 2.4: Multiarchitecture meso-scale assemblies. (a,b) Laminate assemblies: (A), Mod-(B), (A) and Mod-(B), (A), Mod-(B) (a and b, respectively). The insets highlight differences in reinforcing architecture. Fracture evolution (I, II, III (a) and (b), respectively). (c,d) DIC maps at 0.5% strain in laminate assemblies. (e) Sketch of cross section of cortical bone. (f) Cortical bone inspired meso-scale assembly. Mod-(A) constitutes osteon-inspired features (dashed red semicircles), (A) constitutes the matrix phase. (g) DIC map at 7% strain and highlighting strain distribution in cortical bone inspired assembly. (h,i) Fracture evolution at 11% and 21% strain (h and i, respectively).

2.5 Conclusions

In this study, we developed architected composite materials that exhibit a high degree of hierarchical order through material design. By utilizing a virtual growth algorithm, we manipulated the local connectivity between isodensity tiles, resulting in the formation of larger meso-structures, which were merged to create sample-sized assemblies with predetermined spatial arrangements. This approach enabled tailoring the mechanical and fracture properties of the architected composites, at

the local and global scales. We envision that the use of different sets of starting tiles and the combination of different reinforcing and matrix phases, will allow for fine-tuning the activation of desired reinforcement and fracture energy dissipation mechanisms. Building on our proof-of-concept observations, we hypothesize that controlling the spatial arrangement and continuity between the soft and stiff phases can be used to prevent interfacial failure, while their intentional design can facilitate the precise spatial distribution of fractures in architected composites.

Acknowledgements

The authors thank P. Arakelian, K. Liu, T. Zhou, C. McMahan, and J. Boddapati for the fruitful discussions. The authors acknowledge MURI ARO W911NF-22-2-0109 for the financial support. T.M. acknowledges the Swiss National Science Foundation for the financial support (SNSF Postdoc.Mobility Fellowship, P500PT_203197/1).

BIBLIOGRAPHY

- [1] R. F. Gibson, *Compos. Struct.* **2010**, 92, 2793.
- [2] J. Fan, J. Njuguna, *Lightweight Composite Structures in Transport*, Elsevier **2016**, pp. 3–34.
- [3] B. Budiansky, J. W. Hutchinson, A. G. Evans, *J. Mech. Phys. Solids* **1986**, 34, 167.
- [4] A. G. Atkins, *Nature* **1974**, 252, 116.
- [5] F. M. Monticeli, F. R. Fuga, M. V. Donadon, *Thin-Walled Struct.* **2023**, 187, 110742.
- [6] R. O. Ritchie, *Nat. Mater.* **2011**, 10, 817.
- [7] M. Maurizi, B. W. Edwards, C. Gao, J. R. Greer, F. Berto, *Extreme Mech. Lett.* **2022**, 56, 1.
- [8] K. Wu, Z. Song, S. Zhang, Y. Ni, S. Cai, X. Gong, L. He, S.-H. Yu, *Proc. Natl. Acad. Sci.* **2020**, 117, 15465.
- [9] K. M. Conway, C. Kunka, B. C. White, G. J. Pataky, B. L. Boyce, *Mater. Des.* **2021**, 205, 1.
- [10] M. Sistaninia, R. Kasberger, O. Kolednik, *Compos. Struct.* **2018**, 185, 113.
- [11] L. K. Jain, R. C. Wetherhold, *Acta Metall. Mater.* **1992**, 40, 1135.
- [12] D. A. Norman, R. E. Robertson, *J. Appl. Polym. Sci.* **2003**, 90, pp. 2740.
- [13] A. C. Garg, *Eng. Fract. Mech.* **1988**, 29, 127.
- [14] J. P. Lucas, *Eng. Fract. Mech.* **1992**, 42, 543.
- [15] Y. Mao, J. W. Coenen, J. Riesch, S. Sistla, J. Almanstötter, J. Reiser, A. Terra, C. Chen, Y. Wu, L. Raumann, T. Höschen, H. Gietl, R. Neu, C. Linsmeier, C. Broeckmann, *Nucl. Fusion* **2019**, 59, 086034.
- [16] S. K. Gaggar, L. J. Broutman, *Am. Chem. Soc., Div. Org. Coatings Plast. Chem.* **1974**, 34, 354.

- [17] G. C. Jacob, J. M. Starbuck, J. F. Fellers, S. Simunovic, R. G. Boeman, *J. Appl. Polym. Sci.* **2006**, 100, 695.
- [18] Z. Jia, L. Wang, *Acta Mater.* **2019**, 173, 61.
- [19] L. S. Dimas, G. H. Bratzel, I. Eylon, M. J. Buehler, *Adv. Funct. Mater.* **2013**, 23, 4629.
- [20] T. F. W. Van Nuland, J. A. W. Van Dommelen, M. G. D. Geers, *Comput. Mater. Sci.* **2021**, 186, 109947.
- [21] Z. Hooshmand-Ahoor, M. G. Tarantino, K. Danas, *Mech. Mater.* **2022**, 173, 104432.
- [22] R. A. Metzler, F. Barthelat, J. J. Wilker, *Adv. Funct. Mater.* **2019**, 29, 1805734.
- [23] K. Robson Brown, D. Bacheva, R. S. Trask, *J. R. Soc. Interfaces* **2019**, 16, 20180965.
- [24] M. Jentzsch, M. C. Badstöber, F. Umlas, T. Speck, *Front. Mater.* **2022**, 9.
- [25] W. J. Whitehouse, *J. Microsc.* 1974, 101, 153.
- [26] M. J. Buehler, *Modelling Simul. Mater. Sci. Eng.* **2023**, 31 054001.
- [27] K. Liu, R. Sun, C. Daraio, *Science* **2022**.
- [28] M. F. Thorpe, *J. Non Cryst. Solids* **1983**, 57, 355.
- [29] M. F. Thorpe, D. J. Jacobs, N. V. Chubynsky, A. J. Rader, *Rigidity Theory and Applications*, IOS Press, Amsterdam **1999**, p. 239.
- [30] Tong, S. Sengupta, H. Tanaka, *Nat. Commun.* **2020**, 11, 4863.
- [31] F. Fan, S. Huang, H. Yang, M. Raju, D. Datta, V. B. Shenoy, A. C. T. Van Duin, S. Zhang, T. Zhu, *Modelling Simul. Mater. Sci. Eng.* **2013**, 21, 074002.
- [32] C. Meade, R. Jeanloz, *Science* **1988**, 241, 1072.
- [33] J. Mueller, K. Shea, C. Daraio, *Mater. Des.* **2015**, 86, 902.
- [34] L. J. Tan, W. Zhu, K. Zhou, *Adv. Funct. Mater.* **2020**, 30, 2003062.
- [35] A. Pilipovic, P. Raos, M. Sercer, *Int. J. Adv. Manuf. Technol.* **2009**, 40, 105.
- [36] J. Ryan, C. Dizon, A. H. Espera, Q. Chen, R. C. Advincula, *Addit. Manuf.* **2018**, 20, 44.
- [37] D. Bell, T. Siegmund, *Addit. Manuf.* **2018**, 21, 658.

- [38] V. Slesarenko, S. Rudykh, *Int. J. Eng. Sci.* **2018**, 123, 62.
- [39] R. J. Nash, Y. Li, *Eng. Fract. Mech.* **2021**, 253, 107912.
- [40] T. L. Anderson, *Fracture Mechanics: Fundamentals and Applications, 3rd ed.*, CRC Press, Boca Raton, FL **2005**.
- [41] T. Magrini, F. Bouville, A. R. Studart, *Open Ceram.* **2021**, 6, 100109.
- [42] F. Barthelat, H. Tang, P. Zavattieri, C. Li, H. Espinosa, *J. Mech. Phys. Solids* **2007**, 55, 306.
- [43] F. Barthelat, *Bioinspir. Biomim.* **2010**, 5, 035001.
- [44] J. W. Pro, F. Barthelat, *MRS Bull.* **2019**, 44, 46.
- [45] F. Barthelat, Z. Yin, M. J. Buehler, *Nat. Rev. Mater.* **2016**, 1, 16007.
- [46] R. O. Ritchie, *Philos. Trans. R. Soc., A* **2021**, 379, 20200437.
- [47] E. A. Zimmermann, B. Busse, R. O. Ritchie, *Bonekey Rep.* **2015**, 4, 743.
- [48] K. J. Koester, J. W. Ager, R. O. Ritchie, *Nat. Mater.* **2008**, 7, 672.
- [49] T. Magrini, R. Libanori, A. Kan, A. R. Studart, *Rev. Bras. Ensino Fis.* **2021**, 43, 1.
- [50] R. B. Cook, P. Zioupos, *J. Biomech.* **2009**, 42, 2054.
- [51] R. Rabiei, S. Bekah, F. Barthelat, *Acta Biomater.* **2010**, 6, 4081.

*Chapter 3*FRACTURE CHARACTERIZATION OF BIOINSPIRED
IRREGULAR NETWORK REINFORCED COMPOSITES

C. Fox, T. Magrini, & C. Daraio, (2024). “Fracture Characterization of Bioinspired Irregular Network Reinforced Composites” (In Review).

doi: 10.48550/arXiv.2410.09061.

C.F participated in the conceptualization, design, fabrication, and testing of samples, data analysis and visualization, and in writing and revising the manuscript.

Chapter Abstract

The mechanical behavior of composite materials is significantly influenced by their structure and constituent materials. One emerging class of composite materials is irregular network reinforced composites (NRC's), whose reinforcing phase is generated by a stochastic algorithm. Although design of the reinforcing phase network offers tailorable control over both the global mechanical properties, like stiffness and strength, and the local properties, like fracture nucleation and propagation, the fracture properties of irregular NRC's has not yet been fully characterized. This is because both the irregular reinforcing structure and choice of matrix phase material significantly affect the fracture response, often resulting in diffuse damage, associated with multiple crack nucleation locations. Here, we propose irregular polymer NRC's whose matrix phase has a similar stiffness but half the strength of the reinforcing phase, which allows the structure of the reinforcing phase to control the fracture response, while still forming and maintaining a primary crack. Across a range of network coordination numbers, we obtain J-integral and R-curve measurements, and we determine that low coordination polymer NRC's primarily dissipate fracture energy through plastic zone formation, while high coordination polymer NRC's primarily dissipate energy through crack extension. Finally, we determine that there are two critical length

scales to characterize and tailor the fracture response of the composites across the coordination numbers: (i) the size of the plastic zone, and (ii) the size and geometry of the structural features, defined as the areas enclosed by the reinforcing network.

3.1 Introduction

Architected materials often draw inspiration from the structure of biological materials to achieve desirable properties such as high stiffness and strength^[1–3], good energy dissipation^[3–6], and high fracture toughness^[2,7–13]. These bioinspired materials also often feature two or more phases^[6,7,13–16], as biological materials are typically composite materials, such as bone^[17–20] or nacre^[21,22], with mechanical properties superior to that of their constitutive elements. Although most bioinspired composite materials feature repeating structural patterns^[7,8,23–26], many biological materials have a non-periodic structure^[24,27–29], indicating that evolution may favor irregularity as a way to optimize function^[27].

To explore the role of irregularity, virtual growth algorithms (VGA) have been developed to imitate the stochastic growth process of biological material structures^[30,31]. These algorithms generate a continuous irregular network by assembling a set of building blocks according to local connectivity rules, and studies have been conducted to determine the relationship between the structure and function of these networks^[30–32], including for polymer composite materials^[3,10], whose reinforcing phase is generated by the VGA. It has been shown that controlling the average network coordination^[33,34], defined as the number of branches in each building block, primarily influences the stiffness and strength of the materials^[3,10,31,35], while controlling the connectivity rules determines the formation of specific structural features, defined as the areas enclosed by the reinforcing network^[3,10].

However, despite the large design space offered by the choice of building blocks and their connectivity rules, polymer composites reinforced by stiff irregular networks with a compliant matrix display the same fracture behavior^[10]. Fracture begins with the nucleation of voids in the compliant matrix, similar to what is observed in ductile metals^[36], followed by bridging of the reinforcing phase, similar to what occurs in fiber reinforced composites^[37–40]. During fracture bridging, the most extensible portions of the reinforcing phase deform in the direction of the applied load, until they undergo local yielding followed by sequential strut failure^[10]. The sequential failure of the reinforcing phase causes the coalescence of the large-scale voids, leading to the overall loss of structural integrity in the composites^[10].

Previous efforts have shown how to nucleate and guide the fracture path^[10], but the fracture properties of irregular network reinforced composites have not yet been fully characterized. To better understand the role of the reinforcing phase during fracture, we generate centimeter-scale polymer composite materials (with millimeter scale features), whose matrix phase has a similar stiffness but half the strength of the reinforcing phase. This prevents the diffuse nucleation of voids across the sample and maintains a primary crack, making fracture characterization measurements possible, while still allowing the reinforcing phase to significantly influence the fracture response. Across a range of coordinations from 2.3 to 2.8, we determine that there are two critical length scales necessary to understand and describe the fracture response of the composites: (i) the plastic zone size, and (ii) the structural feature size (and geometry). We then show how to tailor the tradeoff between plastic zone size and primary crack extension using the coordination number and its effect on the structural feature populations ahead of the crack tip.

3.2 Material and Methods

We generate the irregular reinforcing phase of the polymer composite samples using a VGA^[30]. This computer-assisted material design tool generates the irregular samples on a square grid from a set of three tile types, with coordination numbers of either two, for (-) tiles and (L) tiles, or three, for (T) tiles (Figure 3.1a). Using tile frequency hints and a set of connectivity rules (Figure 3.1b), the VGA assembles the tiles into continuous irregular networks (Figure 3.1c), with a characteristic length defined as one tile, which is equivalent to the smallest possible structural feature that can be formed, with a size of 1 mm (Figure 3.1c). We generate samples with an average coordination that ranges from 2.3 to 2.8 (Figure 3.1d), which spans the transition from floppy to rigid behavior while maintaining percolation^[33,41]. The 2.3 coordination samples are composed of 5% (-) tiles, 65% (L) tiles, and 30% (T) tiles, the 2.5 coordination samples are composed of 5% (-) tiles, 45% (L) tiles, and 50% (T) tiles, and the 2.8 coordination samples are composed of 10% (-) tiles, 10% (L) tiles, and 80% (T) tiles, with equally represented two-fold ((-) tiles) or four-fold rotations ((L) and (T) tiles). To determine the sample size needed for testing, we determine the minimum number of tiles required for the network to be representative of the coordination number's population of structural features by finding an exponential fit and looking for when the exponential fit parameters converge as the sample size increases (Figure 3.1j, 1k). We find that samples of 30x30 tiles are sufficiently representative (Figure 3.1f-i), but we also note that networks with higher coordination reach a plateau more quickly than lower coordination ones, as the structural feature size depends on the coordination number (Figure 3.1k, Appendix B.2.1).

To fabricate our polymer composite samples for single edge notch plate tension tests, we first choose the volume fraction of the reinforcing phase in each tile, with values of 20% for 2-coordination tiles and 30% for 3-coordination tiles, corresponding to a branch width of 0.2 mm. We then add a matrix phase with a

similar stiffness (~ 1 GPa)^[9,10,42,43], but half the strength of the reinforcing phase (Figure 3.1e) to fill the remaining space in each tile. We use a Polyjet printer (Stratasys Objet500 Connex3) to additively manufacture the composite materials using a commercially available photoresin (VeroWhite Polyjet Resin, Stratasys) for the reinforcing network, and a compatible photoresin with lower strength (Stratasys Grey60 Polyjet Resin) for the matrix (Figure 3.1e). Furthermore, the composite materials have a strong adhesion between phases, key to avoid delamination during fracture testing.

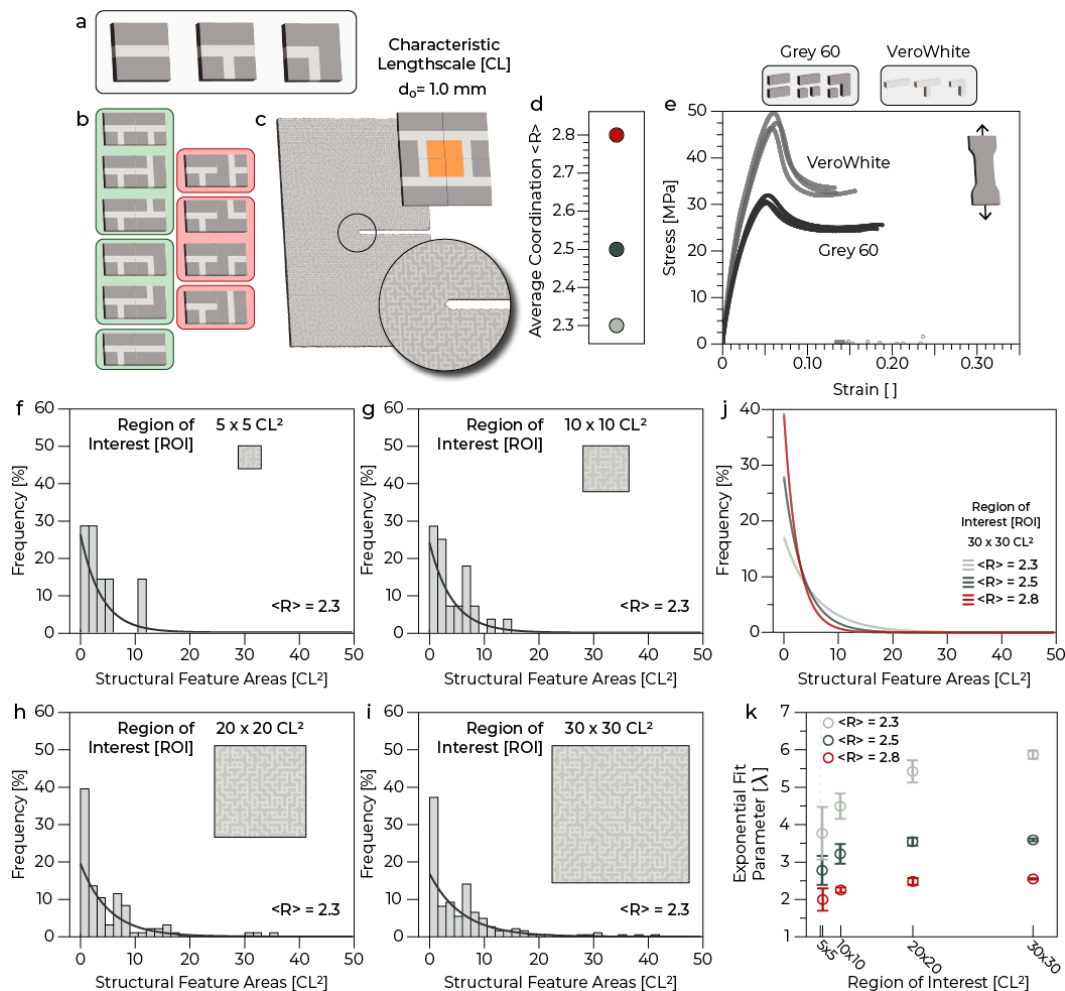


Figure 3.1: Material and structural characterization. (a) VGA tiles and coordination numbers. (b) VGA connectivity rules, green is allowed, red is not allowed. (c)

Fracture samples with characteristic length scale. (d) Average coordination number. (e) Constitutive uniaxial stress-strain plot for reinforcing and matrix phase materials. (f-i) Frequency of 2.3 coordination structural feature areas for 5x5, 10x10, 20x20, and 30x30 tiles. (j) Exponential fits of structural feature areas for 2.3, 2.5 and 2.8 coordination samples with 30x30 tiles. (k) Exponential fit parameters for increasing sizes of sample regions of interest.

3.3 Results and Discussion

3.3.1 Single Edge Notch Plate Tension Fracture Tests

We conduct single edge notch plate tension fracture tests on composite samples of 9x6 cm, corresponding to 90x60 tiles (or characteristic lengths), with a thickness of 1mm and an initial crack of length 3 cm, which we sharpen with a razor blade prior to testing. Grip areas of height 3 cm, manufactured from the same photoresin as the reinforcing phase, are added during printing to the top and bottom of the sample. We use an Instron E3000 (Instron, USA) equipped with a 5 kN load cell to apply a tensile load at a rate of 2 mm/min and we test three different samples for each coordination, repeating one of these samples three times to verify that the same structure fractures self-consistently. We compare our results to samples exclusively composed of the matrix and reinforcing phases (Figure 3.2a,e), and similar to the bulk materials, the composite samples maintain one primary crack, which initiates and propagates through both phases as the tensile loading is applied. This is the consequence of the relatively low mismatch in mechanical properties between the reinforcing and matrix phase polymers, which prevents crack arrest at the interface [44]. Nonetheless, despite having similar volume fractions of reinforcing phase across the coordination numbers, with values of 23%, 25% and 28% for 2.3, 2.5, and 2.8 coordinations, respectively, the force-displacement curves (Figure 3.2b-d) display significant variations. Among composite samples, 2.3 coordination samples fail at the highest global strain, while 2.8 coordination samples fail at the lowest global strain (Figure 3. 2b,d). The measured strain-to-failure values are in between the recorded strain-to-failure values for the bulk materials (Figure 3.2a,e). To explain these variations, we track the strain fields ahead of the crack tip using 2D

digital image correlation. We spray paint the samples with matte white paint and apply matte black speckles of diameter 0.1-0.3 mm and then use VIC-2D (Correlated Solutions, USA) to analyze the Lagrangian strain fields. Unlike previous studies featuring composites with a soft elastomeric matrix, which are prone to multiple void nucleation sites and diffuse damage across the entire sample [10] (Figure B.1), we observe the formation of a single plastic zone across all samples. Assuming that plastic yielding begins when the maximum principal strain value exceeds the yield strain from the constitutive uniaxial stress-strain data, we apply a threshold and track the size of the plastic zone with respect to the sequential events: yield, crack initiation, and sample failure (Figure 3.2f-j). Most importantly, we note that the plastic zone in all samples develops to be over one order of magnitude larger than the structural features.

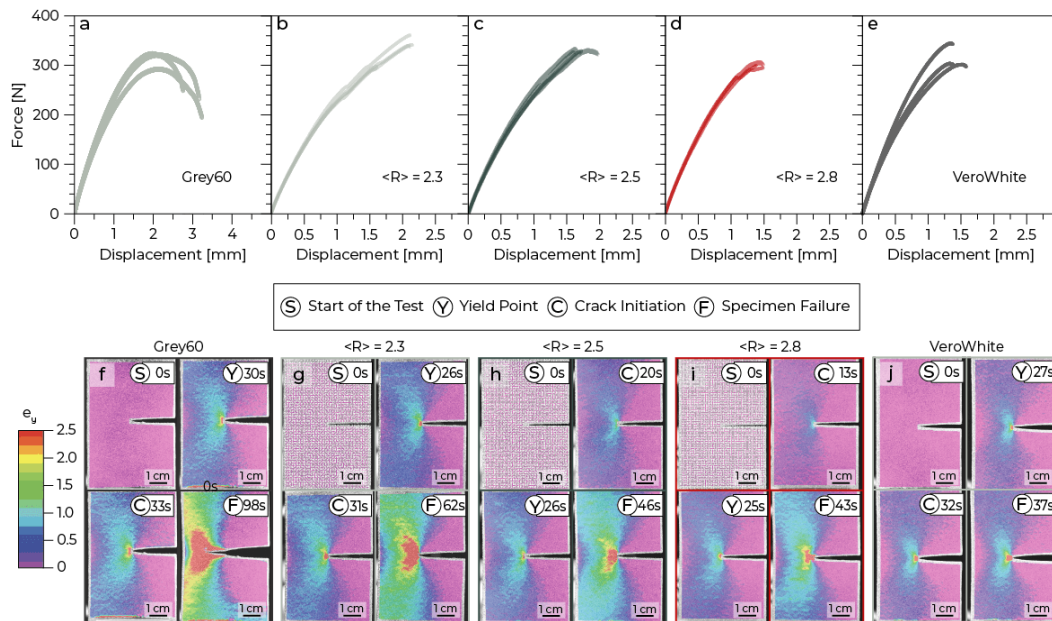


Figure 3.2: Mechanical characterization and DIC images of plastic zone growth for bulk material and composite samples. (a-e) Force-displacement plots for bulk and composite samples. (f-j) 2D DIC strain maps of bulk and composite samples with plasticity threshold in red and time stamps.

3.3.2 Fracture Behavior of the Composites: Plastic Zone Formation and Crack Extension

Although the plastic zone begins to develop at approximately the same global displacement in all samples, we observe that the maximum size of the plastic zone reached by each coordination increases non-linearly with coordination number (Figure 3.3a; Figure B.2). By tracking the amount of crack extension with respect to the global displacement applied, using the image processing software, FIJI [45], we also observe that lower coordination samples have less crack extension despite reaching a higher global strain. Indeed, the 2.3 coordination samples do not exceed 1.4 ± 0.2 mm of crack extension, while 2.8 coordination samples reach up to 3.5 ± 0.8 mm of crack extension before their sudden failure (Figure 3.3b). This tradeoff between plastic zone size, crack extension, and global strain-to-failure is also reflected in the J-integrals for each sample. We define the J-integral for an edge cracked sample as:

$$J = \frac{\eta U}{Bb}, \quad (1)$$

where η is a dimensionless constant, U is the area under the force displacement curve, B is the sample thickness, and b is the uncracked length^[36] (Figure 3.3b, inset). The J-integral can also be written as a sum of its elastic and plastic components:

$$J = J_e + J_p, \quad (2)$$

$$J_e = \frac{\eta_e U_e}{Bb}, \quad (3)$$

$$J_p = \frac{\eta_p U_p}{Bb}, \quad (4)$$

where e and p refer to the elastic and plastic components, respectively [36]. By extracting the elastic and plastic components of the J-integral incrementally (Figure B.3), we observe the tradeoff between recoverable and irrecoverable deformation within the samples, as the contribution to the normalized elastic J-integral increases as the coordination number increases, while the contribution to the normalized plastic J-integral decreases as the coordination number increases (Figure 3.3c).

We then obtain the R-curves for each coordination by plotting the normalized J-integrals as a function of crack extension (Figure 3.3d). Regardless of their coordination, all samples exhibit a rising trend, although the shape of each R-curve varies significantly across the coordination numbers (Figure 3.3d). The 2.3 coordination samples have a higher critical J-integral value, J_c , at which the crack begins to grow, while the higher coordination samples show an average decrease in the critical J_c of 32.6% and 61.2% for 2.5 and 2.8 coordinations, respectively. After initiation, the 2.3 coordination samples all exhibit subcritical crack extension of a few characteristic lengths before reaching a saturation point, during which the crack arrests and the plastic zone grows until the sample reaches a maximum J-integral value, J_m , and the sample fails suddenly (Figure 3.3d, left). In contrast, the 2.5 coordination samples all exhibit simultaneous crack extension and plastic zone growth before sample failure, reaching a 16.1% lower average J_m than the 2.3 coordination samples (Figure 3.3d, center). However, unlike the lower coordinations, the 2.8 coordination samples reach a saturation point in plastic zone size, allowing for several characteristic lengths of crack extension before sample failure, and reaching the lowest average J_m , 29.4% lower than the 2.3 samples (Figure 3.3d, right). We then compare the composite materials with the bulk materials of the reinforcing and matrix phases. The bulk material of the matrix phase displays a larger plastic zone area than the 2.3 coordination samples and has a constantly rising R-curve with simultaneous crack extension. In contrast, the bulk material of the reinforcing phase displays a smaller plastic zone area than the 2.8

coordination samples, with a very short R-curve, as the sample fails at very low global strain with little crack extension (Figure B.4).

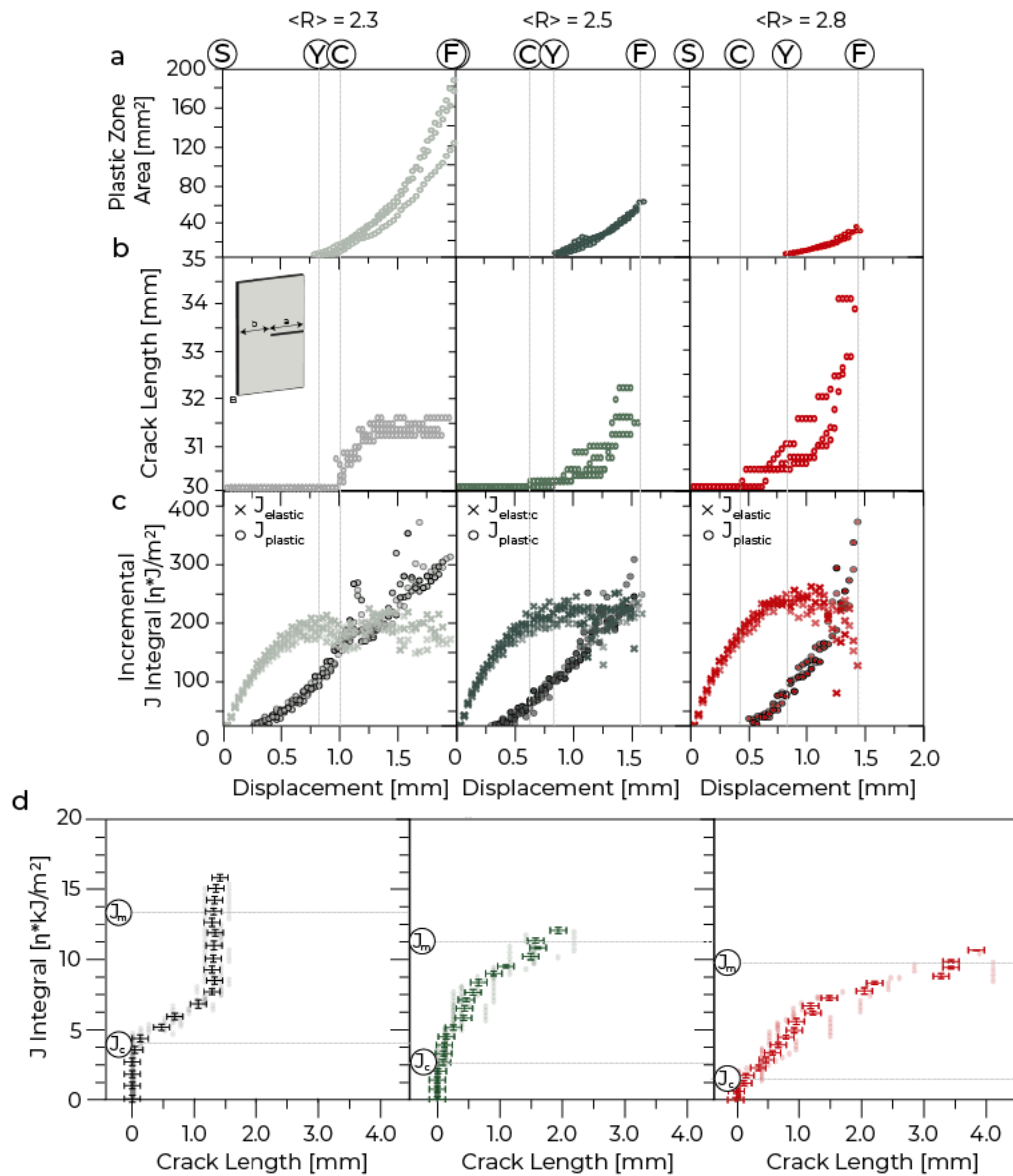


Figure 3.3: Plastic zone size, crack extension length, J-integrals and R-curves for composite material samples. S corresponds to start of test, Y corresponds to yielding, C corresponds to crack initiation, F corresponds to failure. (a) Plastic zone area as a function of displacement for 2.3, 2.5, and 2.8 coordination samples. (b) Crack extension length as a function of displacement for 2.3, 2.5, and 2.8 coordination samples, with inset showing single edge notch plate tension sample

dimensions. (c) Incremental elastic J-integrals (η_e normalized) and plastic J-integrals (η_p normalized) as a function of displacement for 2.3, 2.5, and 2.8 coordination samples. (d) R-curves for 2.3, 2.5, and 2.8 coordination samples.

3.3.3 Effect of Structural Features

Although the plastic zone size is the critical length scale to understand and describe the global fracture behavior (R-curves) of the samples, it is also necessary to consider a second length scale: the relative size and distribution of the structural features. Structural features are composed of groups of tiles which form different populations as a function of coordination number, resulting in plastic zone shape variations across the coordination numbers (Figure 3.4a). Lower coordination numbers form more polydisperse structural features with a wide range of sizes, from one characteristic length squared up to tens of characteristic lengths squared, resulting in more extensible composite materials, while higher coordination numbers form more monodisperse structural features that are smaller, resulting in stiffer composite materials (Figure 3.4a; Figure B.5).

In order to characterize the structural features, we describe their size in terms of their bridge lengths, defined as the distances between (T) tiles (Figure 3.4b), and we note that the bridge lengths for each coordination are on the same order of magnitude as the characteristic length of 1 mm, which is at least one order of magnitude lower than that of the plastic zones (Figure 3.4c). It is this relative size ratio, coupled with the reinforcing phase's higher strength, that results in a deformation which not only follows the shape of the local individual structural features ahead of the crack tip, but also globally the characteristic plastic zone shape from linear elastic fracture mechanics ^[36] (Figure 3.4a).

Given that the strain field immediately ahead of the crack tip follows the shape of the local structural features (Figure 3.4a), it is important to examine the orientation

and geometry of these local features (Figure 3.4d,e) to explain why higher coordination samples have greater crack extension. In order to generate higher coordination numbers, because they are stochastically generated on a square grid, samples are forced to form many smaller linear structural features that are aligned in the direction of the primary crack, at 0° (Figure 3.4f). These linear features (Figure 3.4e, red) can be more easily split apart, allowing for more crack extension at lower global strains. In contrast, lower coordination samples have fewer reinforcing interfaces to pass through than high coordination samples, and instead form many larger complex structural features that are at an angle to the primary crack, greater than 0° (Figure 3.4f). It is more difficult for the crack to proceed through these extensible diagonal features (Figure 3.4e, gray, green), resulting in crack arrest and allowing the sample to instead dissipate energy through the formation of a large plastic zone.

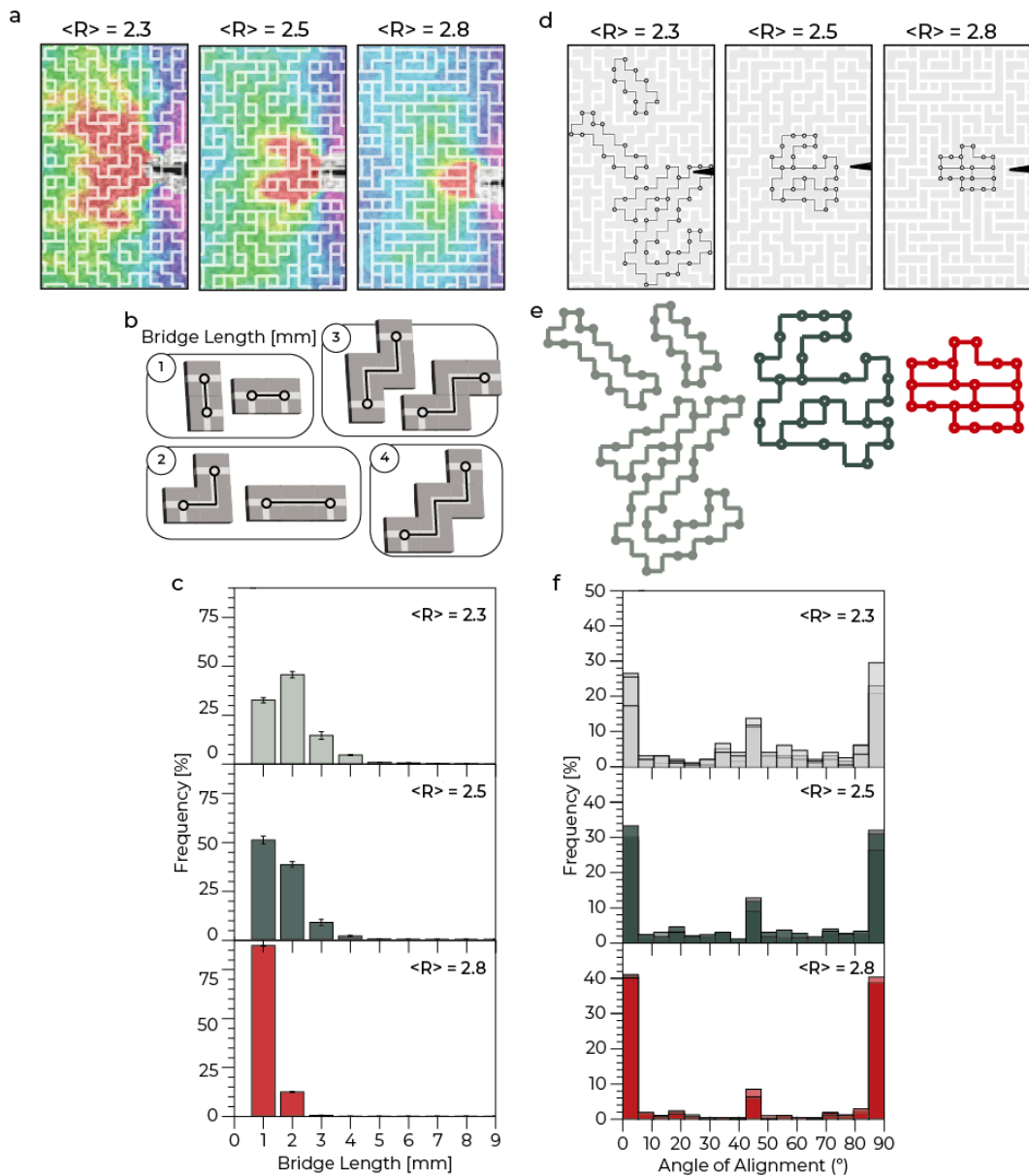


Figure 3.4: Structural feature analysis. (a) Zoomed images of maximum plastic zone area for 2.3, 2.5, and 2.8 coordination samples with overlaid map of structural features. (b) Sample bridges for lengths of 1, 2, 3, and 4 mm (characteristic lengths). (c) Distributions of bridge lengths for 2.3, 2.5, and 2.8 coordination samples. (d) Samples with highlighted structural features ahead of the crack tip that contribute to the plastic zone shape for 2.3, 2.5, and 2.8 coordination samples. (e) Sample structural features with their constitutive bridges for 2.3, 2.5, and 2.8 coordination samples (gray, green, red, respectively). (f) Distributions of angles of alignment of structural features for 2.3, 2.5, and 2.8 coordination samples.

3.3.4 Plastic Zone Tailoring

With the two critical length scales in mind (the size of the plastic zone that is able to develop, and the population of structural features composing a given coordination number), we then seek to control the fracture response of the composite materials by spatially tailoring the coordination number. We create laminated assemblies with 25% high coordination and 75% low coordination regions in the sample (high-R edge) and then the inverse, with 25% low coordination and 75% high coordination regions (low-R edge) and perform the same single edge notch plate tension tests (Figure 3.5a). We observe that the low-R edge makes it possible for the development of a significantly larger plastic zone in the 2.8 coordination region than the 100% 2.8 coordination samples previously discussed (Figure 3.5b,c). In contrast, the high-R edge prevents the formation of as large of a plastic zone in the 2.3 coordination region as observed in the 100% 2.3 coordination samples previously discussed (Figure 3.5b,d). This ‘flipping’ effect is likely the result of the similarity in the matrix and reinforcing phase stiffnesses, which allows the entire structure to simultaneously engage in the deformation, prior to and during plastic zone formation. It is also important to note the effect of the interface where the low coordination region transitions to the high coordination region, and vice versa, which is only one characteristic length wide. This transition line causes the vertical flattening of the plastic zone in the high-R edge sample, as the population of structural features abruptly transitions from larger and more extensible to smaller and less extensible (Figure 3.5d). In contrast, the low-R edge sample transitions from smaller structural features to larger structural features, allowing for greater extensibility and a larger plastic zone ahead of the crack (Figure 3.5c).

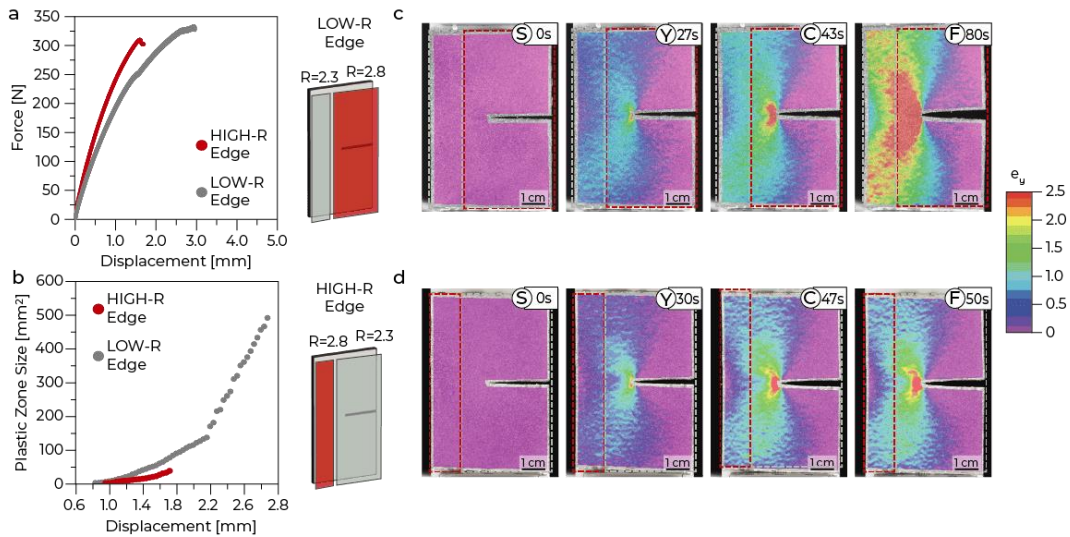


Figure 3.5: Tailoring the plastic zone. (a) 2.3 coordination and 2.8 coordination edge sample force-displacement plot. (b) Plastic zone size growth for 2.3 and 2.8 coordination edge sample. (c) 2D DIC strain maps for 2.3 coordination edge sample. (d) 2D DIC strain maps for 2.8 coordination edge sample.

3.4 Conclusions

We study the fracture behavior of nearly isodense bioinspired polymer composites with irregular network reinforcing phases. The composites feature a matrix phase with a similar stiffness but half the strength of the reinforcing phase, allowing for the formation and extension of a primary crack and therefore J-integral and R-curve measurements. We compare the effect of coordination number, a global scale descriptor, to the mechanical properties of the reinforcing phase, through measurements of plastic zone size and crack extension. We observe that low coordination samples dissipate fracture energy through the formation of a large plastic zone, and fail at higher global strain, while high coordination samples dissipate energy through crack extension, and fail at lower global strain. We determine that there are two critical length scales that explain the fracture response of the polymer composites and the variations across the coordination numbers: (i) the size of the plastic zone, and (ii) the size and geometry of the structural features.

Finally, we discuss how to tailor the tradeoff between plastic zone size and primary crack extension using the coordination number and its effect on the structural feature populations ahead of the crack tip.

Acknowledgements

The authors acknowledge F. Bouville, V. Vitelli, and D. Kammer for fruitful discussions. The authors thank P. Arakelian for the experimental assistance. C.F. and C.D. acknowledge MURI ARO W911NF-22-2-0109 for the financial support.

BIBLIOGRAPHY

- [1] Y. Zhang, M. T. Hsieh, L. Valdevit, *Compos Struct* **2021**, 263, 113693.
- [2] J. Jung, A. Chen, G. X. Gu, *Materials Today* **2024**.
- [3] C. Fox, K. Chen, M. Antonini, T. Magrini, C. Daraio, *Advanced Materials* **2024**, 2405567.
- [4] Z. Zhuang, Z. Qian, X. Wang, X. Xu, B. Chen, G. Song, X. Liu, L. Ren, L. Ren, *Advanced Science* **2023**.
- [5] G. X. Gu, M. Takaffoli, M. J. Buehler, *Advanced Materials* **2017**, 29, 1700060.
- [6] F. Li, C. Yu, J. Zhong, C. Zhao, *Mechanics of Advanced Materials and Structures* **2024**.
- [7] T. Magrini, F. Bouville, A. Lauria, H. Le Ferrand, T. P. Niebel, A. R. Studart, *Nature Communications* 2019 10:1 **2019**, 10, 1.
- [8] T. Magrini, A. Senol, R. Style, F. Bouville, A. R. Studart, *J Mech Phys Solids* **2022**, 159, 104750.
- [9] Z. Jia, L. Wang, *Acta Mater* **2019**, 173, 61.
- [10] T. Magrini, C. Fox, A. Wihardja, A. Kolli, C. Daraio, *Advanced Materials* **2023**, 2305198.
- [11] L. S. Dimas, G. H. Bratzel, I. Eylon, M. J. Buehler, *Adv Funct Mater* **2013**, 23, 4629.
- [12] H. Dai, W. Dai, Z. Hu, W. Zhang, G. Zhang, R. Guo, *Advanced Science* **2023**, 10.
- [13] G. X. Gu, F. Libonati, S. D. Wettermark, M. J. Buehler, *J Mech Behav Biomed Mater* **2017**, 76, 135.
- [14] F. Libonati, A. E. Vellwock, F. Ielmini, D. Abliz, G. Ziegmann, L. Vergani, *Scientific Reports* 2019 9:1 **2019**, 9, 1.

- [15] F. Libonati, C. Colombo, L. Vergani, *Fatigue Fract Eng Mater Struct* **2014**, *37*, 772.
- [16] H. D. Espinosa, J. E. Rim, F. Barthelat, M. J. Buehler, *Prog Mater Sci* **2009**, *54*, 1059.
- [17] T. M. Keaveny, E. F. Morgan, G. L. Niebur, O. C. Yeh, *Annu. Rev. Bioeng.* **2003**, *3*, 307.
- [18] W. J. Whitehouse, *J Microsc* **1974**, *101*, 153.
- [19] T. Magrini, R. Libanori, A. Kan, A. R. Studart, *Revista Brasileira de Ensino de Fisica* **2021**, *43*, 1.
- [20] M. E. Launey, M. J. Buehler, R. O. Ritchie, *Annu Rev Mater Res* **2010**, *40*, 25.
- [21] M. A. Meyers, A. Y. M. Lin, P. Y. Chen, J. Muiyco, *J Mech Behav Biomed Mater* **2008**, *1*, 76.
- [22] A. P. J. Ackson, J. F. V Vincent, R. M. T. Uner, *Proc R Soc Lond B Biol Sci* **1988**, *234*, 415.
- [23] G. X. Gu, I. Su, S. Sharma, J. L. Voros, Z. Qin, M. J. Buehler, *J Biomech Eng* **2016**, *138*, 0210061.
- [24] A. R. Studart, *Advanced Materials* **2012**, *24*, 5024.
- [25] M. Li, N. Zhao, M. Wang, X. Dai, H. Bai, *Adv Funct Mater* **2022**.
- [26] D. Gao, P. Chen, G. Lu, H. Yang, *Mater Today Commun* **2023**, *35*, 106031.
- [27] R. A. Metzler, F. Barthelat, J. J. Wilker, *Adv Funct Mater* **2019**, *29*, 1805734.
- [28] M. Jentsch, S. Becker, M. Thielen, T. Speck, *Plants 2022, Vol. 11, Page 991* **2022**, *11*, 991.
- [29] M. Jentsch, V. Albiez, T. C. Kardamakis, T. Speck, *Soft Matter* **2024**, *20*, 2804.
- [30] K. Liu, R. Sun, C. Daraio, *Science* **2022**, *377*, 975.
- [31] Y. Jia, K. Liu, X. S. Zhang, *J Mech Phys Solids* **2024**, *192*, 105787.
- [32] Y. Jia, K. Liu, X. S. Zhang, *Comput Methods Appl Mech Eng* **2024**, *425*, 116864.

- [33] M. F. Thorpe, *J Non Cryst Solids* **1983**, 57, 355.
- [34] M. Thorpe, P. Duxbury, *Rigidity Theory and Applications* **2002**, DOI 10.1007/B115749.
- [35] Y. H. Zhou, Y. F. Zheng, Y. Q. Zhang, H. A. Wu, C. Liu, *Extreme Mech Lett* **2024**, 70, 102196.
- [36] T. L. Anderson, *Fracture Mechanics: Fundamentals and Applications, Fourth Edition* **2017**, 1.
- [37] R. Khan, *Compos Struct* **2019**, 229, 111418.
- [38] C. H. Chen, R. R. Chang, P. H. Jeng, *Mechanics of Materials* **1995**, 20, 165.
- [39] S. Nemat-Nasser, M. Hori, *Mechanics of Materials* **1987**, 6, 245.
- [40] M. Sakai, T. Miyajima, M. Inagaki, *Compos Sci Technol* **1991**, 40, 231.
- [41] *Rigidity Theory and Applications* **2002**.
- [42] J. R. C. Dizon, A. H. Espera, Q. Chen, R. C. Advincula, *Addit Manuf* **2018**, 20, 44.
- [43] V. Slesarenko, S. Rudykh, *Int J Eng Sci* **2018**, 123, 62.
- [44] O. Kolednik, J. Predan, F. D. Fischer, P. Fratzl, *Acta Mater* **2014**, 68, 279.
- [45] C. A. Schneider, W. S. Rasband, K. W. Eliceiri, *Nature Methods* 2012 9:7 **2012**, 9, 671.

*Chapter 4***MECHANICAL AND TEMPORAL RESPONSE OF HIGH-COORDINATED IRREGULAR NETWORK REINFORCED COMPOSITES**

C. Fox, K. Bastawros, T. Magrini & C. Daraio, (2025). “Mechanical and Temporal Response of High-Coordinated Irregular Network Reinforced Composites” (In Preparation).

C.F. participated in the conceptualization, design, fabrication, and testing of samples, data analysis and visualization, and in writing and revising the manuscript.

Chapter Abstract

Irregular architected materials offer a wide design space of mechanical properties beyond that of typical periodic architected materials. However, these irregular materials are often completely stochastic, offering little control over the structure-to-property relationships. Here, we show that intentional design of irregular materials, using topology and geometry, leads to control of the mechanical response. We demonstrate this experimentally using additively manufactured two-phase polymer composites, which we generate using a hexagonal virtual growth algorithm (hexa-VGA). The hexa-VGA tessellates a finite set of hexagonal tiles into an irregular network according to coordination number, defined as the average number of connections per network node, with values from one to six. The network then forms the stiff reinforcing phase of the composites, while the space enclosed by the network is filled with a soft matrix. Through plate tension tests, we show that the coordination number determines the mechanical response, allowing us to achieve temporal variations in the fracture response as well as improved damage tolerance.

4.1 Introduction

Architected materials offer a wide range of mechanical properties through the careful design of their structure and the choice of their constitutive materials. Truss and shell-based materials, for example, offer a way to achieve high stiffness and strength while maintaining low weight^[1-4], while architected composites offer higher toughness than their constitutive bulk materials^[5-8]. These materials often rely on periodicity to achieve their properties, with repeating unit cells which can be tessellated to form an effectively bulk material across a range of different length scales^[4,7,9,10]. Although periodic architected materials are easier to fabricate and analyze^[2,3], researchers have recently begun to explore the design space of irregular architected materials^[11-24]. These irregular materials are generated using a wide variety of methods, including spinodal decomposition^[19-21], Voronoi tessellations^[22-24], and virtual growth algorithms^[25-27], which stochastically arrange sets of tiles into irregular networks. It has been shown that these irregular architected materials can provide desirable mechanical performances, such as superior damage tolerance^[28], tailorable stiffness, strength and fracture toughness^[16,17,25,26,29,30], as well as improved energy absorption^[18,19].

To further expand the design space of irregular architected materials, we present here irregular network reinforced composites generated using a hexagonal virtual growth algorithm. Inspired by the stochastic assembly of natural structures, the algorithm grows a network from a set of nodes on a hexagonal grid, with up to 6-sided connectivity for each node. The generated network can be defined by a coordination number, which is the average number of connections per node^[31,32]. The higher degree of possible connectivity allows us to study the transition from bending-dominated to stretching-dominated irregular structures, as defined by the Maxwell number^[33], using the coordination number as the input parameter to span the design space. The virtual growth algorithm also provides precise control over both reinforcing network geometry, defined as the shape of structural features

enclosed by the network, and the network topology, defined as the network connectivity, allowing us to decouple the effects of these parameters on the mechanical response. Through study of additively manufactured polymer composites, we demonstrate that the coordination number is the most relevant predictor of global mechanical properties in these irregular architected materials. We then go one step further to show how irregularity can influence the temporal evolution of fractures, and improve damage tolerance in both bending- and stretching-dominated irregular network reinforced composites.

4.2 Material Design, Generation and Characterization

4.2.1 Sample Generation

We generate our samples using a hexagonal virtual growth algorithm (hexa-VGA), which assembles a network from a set of nodes placed on a hexagonal grid^[34]. Each node has up to 6-sided connectivity and the hexa-VGA generates samples by first defining a list of all possible lines in the network which connect the nodes. The hexa-VGA then selects an arbitrary endpoint and uses the input parameter of coordination number, defined as the average number of connections per node, to assign X lines per node with a “positive” status, while the remaining lines are assigned a “negative” status. Once all lines for a given node are assigned, the hexa-VGA removes the endpoint from the list of available nodes, checks if any of the six neighboring endpoints are free endpoints, and repeats the process. If there are no free neighboring endpoints, a random endpoint is selected, and the process continues until all lines have been assigned a status. Given the underlying hexagonal grid and 6-sided connectivity of the network, we can therefore define a set of 63 geometrically or rotationally unique tiles, which tessellate to form continuous networks (Figure 4.1a, b).

Using the coordination number as a design parameter for the hexa-VGA, we study a range of networks, from coordination $2X$ to coordination $6X$. To understand the

effect of locally-varying geometry and topology on the global mechanical response, we compare homogenous and non-homogenous distributions of network node connectivity (Figure 4.1c). Homogeneous (H) networks are composed primarily of tiles of their coordination number, while the non-homogeneous (nH) networks are composed of different tiles, which average to the same coordination number. For example, we study homogeneous networks with coordination $3X$ composed of only tiles with coordination $3X$ (H3_3X). We also study non-homogeneous networks with coordination $3X$, either composed of $2X$ and $4X$ tiles (nH3_24X), or composed of $1X$ and $5X$ tiles (nH3_15X). Furthermore, we study homogenous networks with coordination $4X$ (H4_4X), as well as non-homogeneous networks composed of $3X$ and $5X$ tiles (nH4_35X), and of $1X$ and $5X$ tiles (nH4_15X). The $3X$ and $4X$ coordination samples also mark the transition point from bending-dominated to stretching-dominated 2D lattices, as defined by the Maxwell number^[33],

$$M = b - 2j + 3, \quad (1)$$

where b is the number of struts between nodes of coordination 3 or greater, and j is the number of these tiles. It is therefore possible for samples to have the same coordination number and same average structural feature areas (Figure 4.1d), while the Maxwell number varies significantly as a result of topological variations (Figure 4.1e).

To fabricate our irregular composite materials for testing, we use a Polyjet printer (Stratasys Objet500 Connex3), and we select a stiff viscoelastic resin (VeroWhite Polyjet Resin) for the reinforcing network phase and a soft elastomeric resin (TangoBlack Polyjet Resin) for the matrix phase. Both resins are commercially available, and their constitutive properties (Figure C.1) fall within ranges reported in literature^[35–37]. We print the irregular network reinforced composites in a plate

tension geometry, with a width of 5 cm, thickness of 3 cm, and a height of 10 cm, with grips of height 3.75 cm. For consistency, we design all samples with 25 hexagonal tiles across and a constant width of the reinforcing network of 0.5 mm, which is an order of magnitude greater than the minimum printer resolution^[38]. As a result of maintaining a constant network width, the volume fraction of the different samples increases linearly with increasing coordination, with a value of 0.23 ± 0.001 for 2X samples up to a value of 0.57 ± 0.001 for 6X samples.

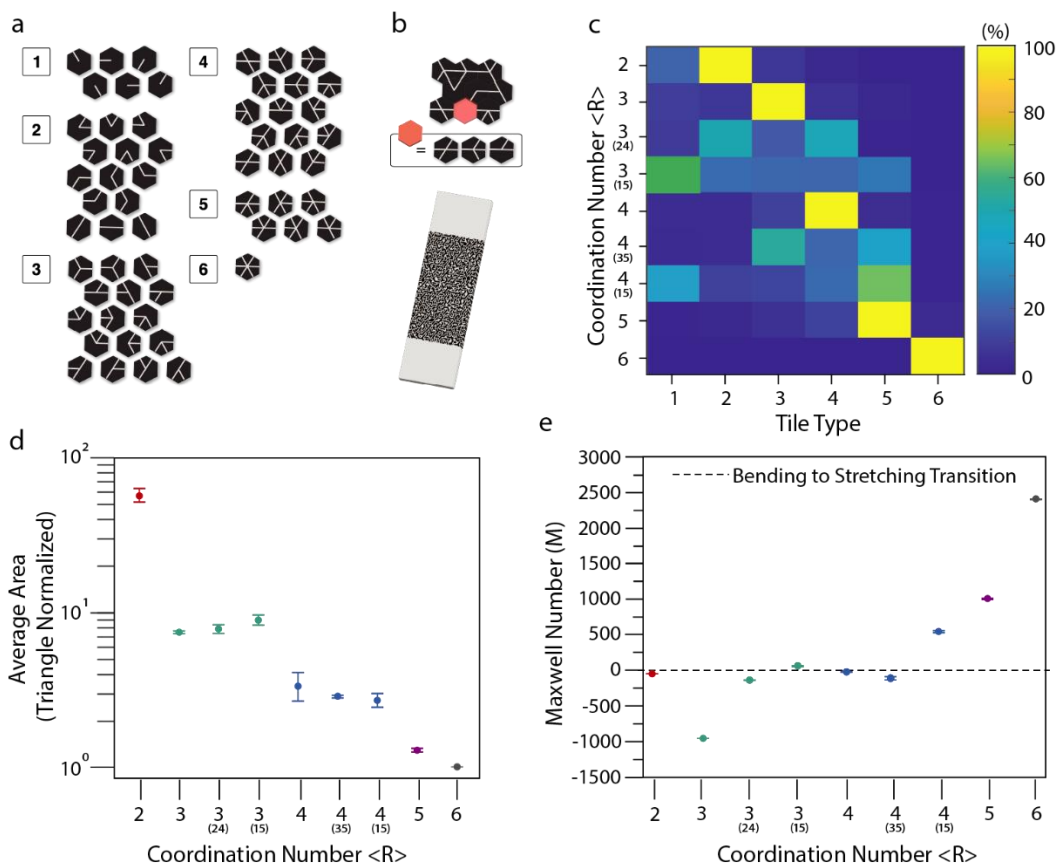


Figure 4.1: Hexa-VGA generated sample design and structure characterization. (a) Hexa-VGA tiles. (b) Example hexa-VGA network generation and plate tension sample. (c) Tile distributions for each coordination and topology type. (d) Average area as a function of coordination number. (e) Maxwell number as a function of coordination number.

4.2.2 Structural Characterization

To characterize the differences in structure as a result of both coordination number and topology, we first look at how the structural features are arranged. We can define a feature by its centroid, which is calculated using `regionprops` in MATLAB (MathWorks, USA). We can then measure the distribution of these centroids using a radial distribution function (RDF), defined as:

$$g(r) = \frac{\langle \rho(r) \rangle}{\rho_o}, \quad (2)$$

where $g(r)$ is the radial density at a radius, r , $\rho(r)$ is the local feature density at radius, r , and ρ_o is the feature density of the entire structure (Figure 4.2a, inset). We observe that 6X coordination has a periodic radial density, with peaks and valleys at constant intervals, indicative of long-range order^[39]. As the coordination number decreases, the structure becomes less ordered, with less distinct frequencies, as a result of the larger design space permitted by the possible feature geometries and sizes (Figure 4.2a-e; Figure C.2).

We then quantify the distribution of structural feature areas using `regionprops` in MATLAB (MathWorks, USA). These distributions are effectively a proxy for the Fourier transform of the RDF's, showing the trend of a single frequency for 6X and then wider distributions of frequencies as coordination number decreases (Figure 4.2f-n). The distributions also widen as topology becomes more inhomogeneous in iso-coordination samples. This trend can be observed when comparing H3_3X to nH3_24X and to nH3_15X (Figure 4.2g-i), as well as when comparing H4_4X to nH4_35X and to nH4_15X (Figure 4.2j-l). For comparison, all areas are plotted as triangle normalized, as a triangle formed by three connecting adjacent nodes is the smallest feature that the hexa-VGA can form (Figure 4.2o). To summarize these structural feature distribution trends, we then quantify the polydispersity index

(PDI)^[40,41] of the structural feature areas. The PDI indicates the distribution spread of populations of structural features, and its values range from 1 in samples with coordination 6X, where all features are identical, up to 4.3 ± 0.9 for 2X, where the largest possible features can form (Figure 2p).

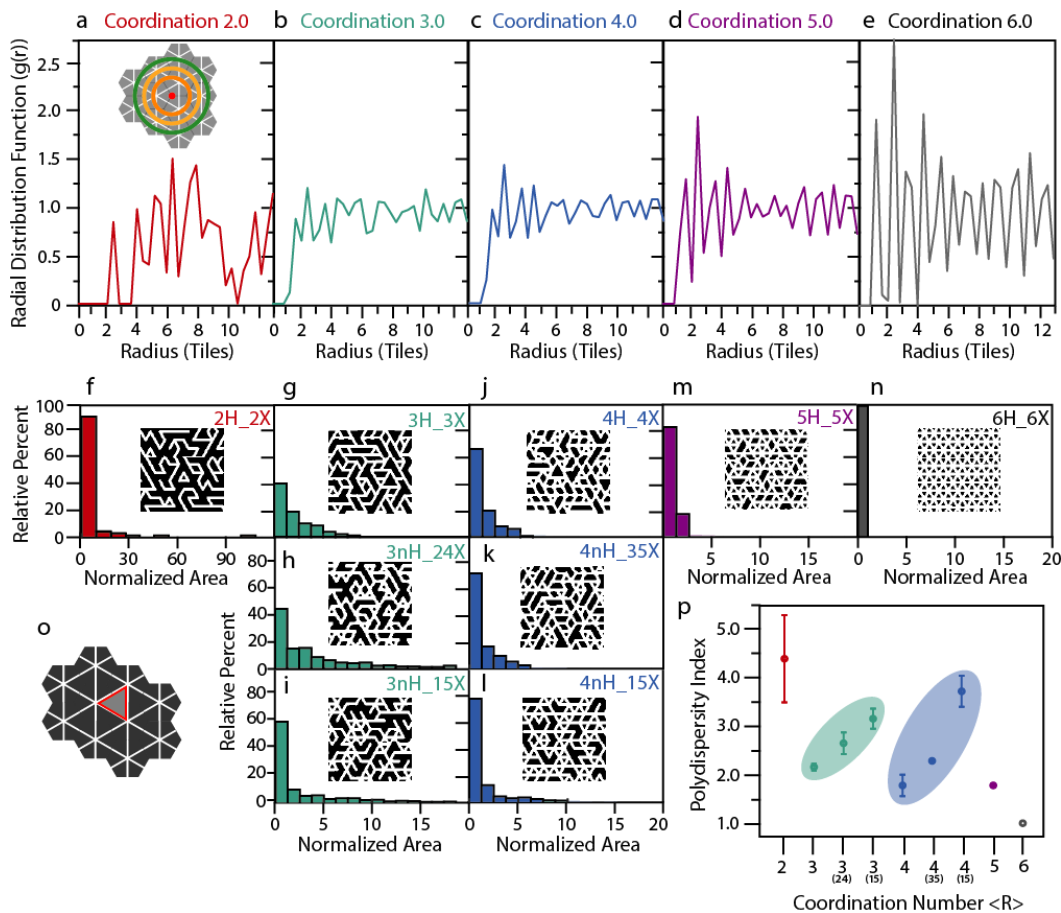


Figure 4.2: Geometry characterization of reinforcing network phase. (a-e) Radial distribution functions for homogeneous coordination samples. (f-n) Structural feature area distributions for all coordination samples. (o) Example of triangle normalized area. (p) Polydispersity index (PDI) as a function of coordination number for all coordination samples.

4.3 Results and Discussion

4.3.1 Homogenous Topology Tensile Plate Tension Tests

We conduct plate tension tests on the composites to understand the effect of coordination number and topology on the mechanical response across the bending to stretching-dominated regimes. We use an Instron E3000 with a 5 kN load cell and fix the samples with clamps at the top and bottom, and then we load the samples at a quasi-static rate of 2 mm/min until failure, defined as the point when samples lose all load-bearing capacity.

We first look at the homogeneous topology cases from 2X to 6X. Lower coordination samples show a more ductile response, with larger values of strain-to-failure, while higher coordination samples show lower values of strain-to-failure, but higher strength (Figure 4.3a-e). This tradeoff is partly due to the volume fraction of the reinforcing phase, which linearly increases with coordination number, and partly due to the mechanisms of deformation. At lower coordinations (less than 4X), the composites are primarily bending-dominated, while at higher coordinations, the samples are primarily stretching-dominated, and become stiffer and stronger. We also observe that 6X displays a nearly perfect elastic-plastic response, similar to that of the bulk VeroWhite material^[17] (Figure C.1), indicating that the reinforcing phase is dominating the response (Figure 4.3e). At lower coordinations, even those still in the stretching-dominated regime, the composites are affected by the elastomeric properties of the incompressible matrix material (Figure C.1) displaying a more extensible response and longer time from the first drop in load (as a result of local fractures in the reinforcing network), to complete loss of load-bearing capacity (Figure 4.3a-c).

We also conduct 2D digital image correlation (DIC) to understand how strain is accommodated in the materials during loading. We first spray paint the samples with flat white paint and then speckle with flat black paint to achieve an average speckle size of 0.1 to 0.3 mm. We calculate the Lagrangian strain fields using VIC-2D DIC software (Correlated Solutions, USA), with a subset size of 27 and a step

size of 2. DIC maps at 2% global strain highlight that the strain becomes more uniformly distributed across the samples with increasing coordination number (Figure 4.3f-j). These results are in agreement with the trend quantified by the RDF's that demonstrated an increased homogeneity in reinforcing network arrangement with increasing coordination (Figure 4.2a-e).

Finally, we compare the volume fraction equivalent samples for each coordination to see the effect of different structural arrangements of reinforcing phases (i.e. irregular and periodic). We generate 6H_6X coordination samples with varying structural feature sizes to match the volume fraction of the 2H_2X, 3H_3X, 4H_4X and 5H_5X. These samples (6H_2Vf, 6H_3Vf, 6H_4Vf, 6H_5Vf) show a similar mechanical response to the original 6H_6X samples, as they are stretching-dominated with an elastic-plastic loading profile, followed by a sudden failure and loss of load bearing capacity (Figure 4.3k). Unlike the irregular equivalents, these periodic samples do not undergo local failure events with the sawtooth drops in load observed in the irregular equivalents, particularly at higher coordinations, including 4H_4X and 5H_5X. The periodic equivalents also do not reach as high of strain-to-failure values, although this comes at the expense of the ultimate tensile strength, which is higher for the periodic equivalents (Figure 4.3k).

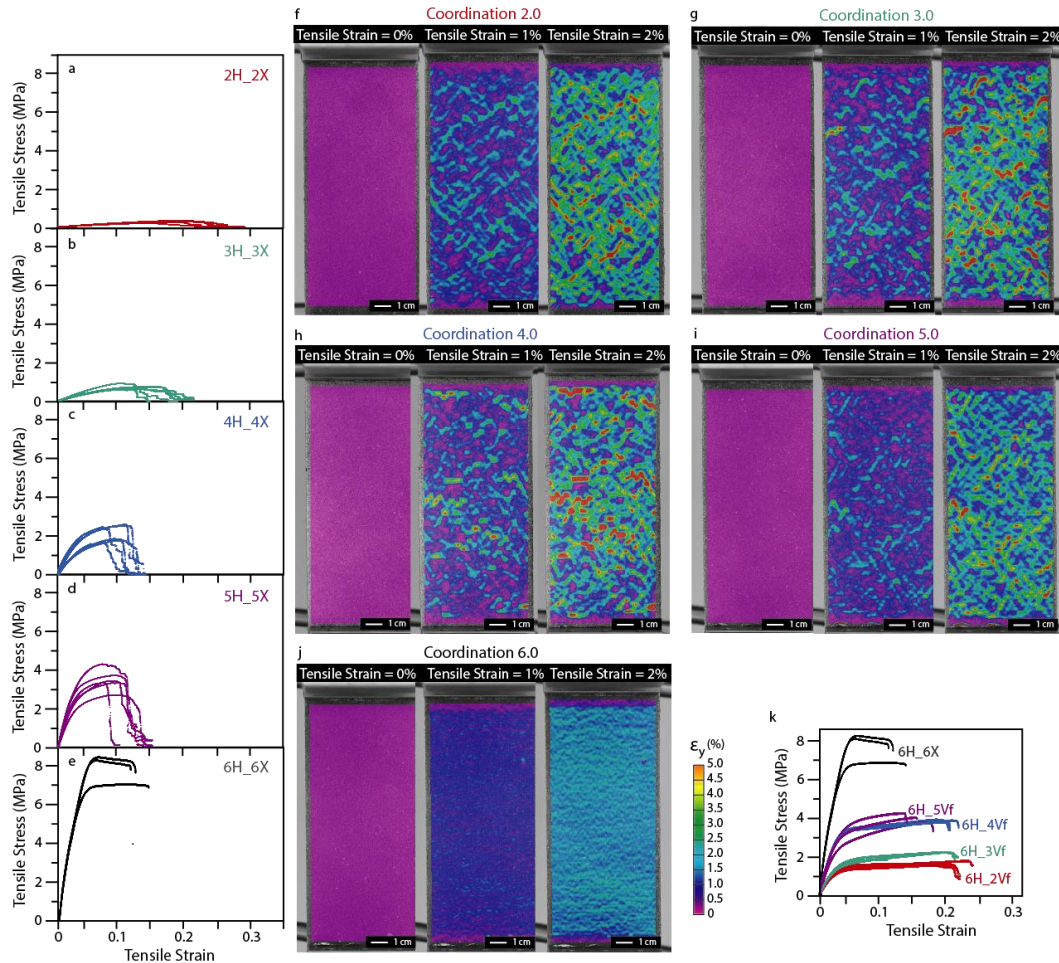


Figure 4.3: Tensile testing of irregular network reinforced composites. (a-e) Tensile stress-strain response of 2H_2X, 3H_3X, 4H_4X, 5H_5X, and 6H_6X coordination samples. (f-j) Example 2D DIC ϵ_y strain fields for each sample from 0 to 2% global tensile strain. (k) Tensile stress-strain response of volume fraction equivalent samples.

4.3.2 Inhomogeneous Topology Tensile Plate Tension Tests

We then explore the effect of varying the topology in iso-coordination samples, effectively decreasing the homogeneity of the structures. To achieve this, we test composites with coordination numbers of 3X and 4X, but vary the topology for each, studying 3H_3X, 3nH_24X, 3nH_15X, 4H_4X, 4nH_35X and 4nH_15X. Due to the variations in topology, the Maxwell number varies significantly,

indicating that 3H_3X, 3nH_24X, 4H_4X and 4nH_35X are in the bending-dominated regime, while 3X(15) and 4X(15) cross the transition to the stretching-dominated regime (Figure 4.1e). We conduct the same plate tension tests as previously described and observe variations in the stress-strain response (Figure 4.4a, b). Samples with greater inhomogeneity and greater PDI appear slightly stiffer and stronger, particularly for 3nH_15X, compared to 3H_3X, and for 4nH_15X, compared to 4H_4X (Figure 4.4a,b, black lines). However, this variation in stiffness is influenced by the volume fraction and by the sample generation method. Indeed, more inhomogeneous topologies result in more constraints during tessellation in the hexa-VGA, as more dissimilar nodes must connect. As a result, nodes grow extra connections to ensure that the sample is one continuous network. This leads to a slightly higher volume fraction of reinforcing phase in the more inhomogeneous samples. These topological variations also cause geometric variations, resulting in more polydisperse structural features, which tend to accommodate strain in more local regions (Figure 4.4c-h). To quantify this effect, we measure the modulus of toughness (MOT), defined as the area under the stress-strain curve, to indicate how much energy the samples can dissipate, and normalize the MOT by the sample volume fraction. We observe that the normalized MOT correlates linearly with the volume fraction variations across the coordination numbers (Figure 4.4i,j), even for bending-dominated composites. This indicates that although the samples accommodate strain differently, the stochastic nature of the irregular network reinforcing phase indicates that the coordination number is the most important parameter for determining the global mechanical response.

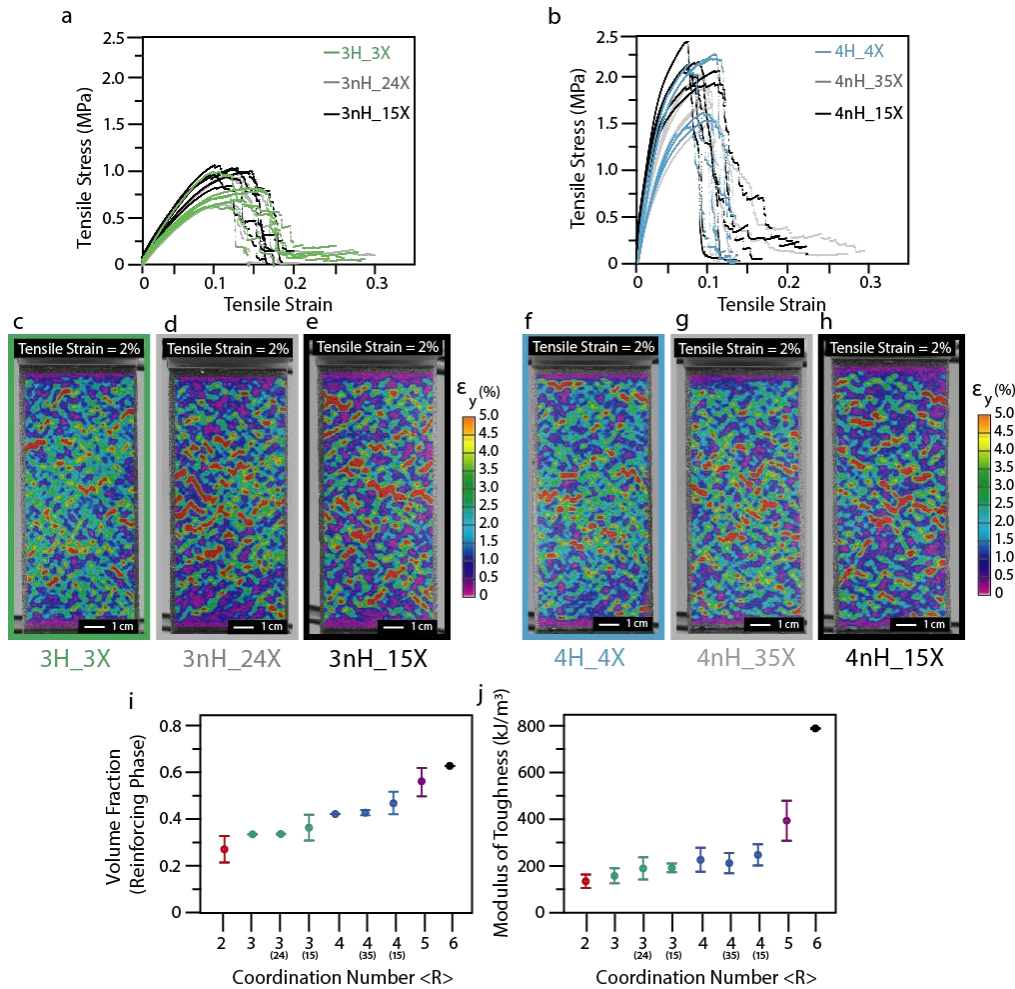


Figure 4.4: Characterizing the effect of inhomogeneous topology on irregular network composites. (a) Tensile stress-strain response of 3H_3X, 3nH_24X and 3nH_15X samples. (b) Tensile stress-strain response of 4H_4X, 4nH_35X and 4nH_15X samples. (c-e) Example 2D DIC ϵ_y strain fields for 3H_3X, 3nH_24X and 3nH_15X samples at 2% global tensile strain. (f-h) Example 2D DIC ϵ_y strain fields for 4H_4X, 4nH_35X and 4nH_15X samples at 2% global tensile strain. (i) Volume fraction of reinforcing phase as a function of coordination number. (j) Modulus of toughness (MOT) (volume fraction normalized) as a function of coordination number.

4.3.3 Fracture and Temporal Response of the Composites

We then study the large strain regime, when the materials begin to fracture. In this regime, we investigate the temporal component of the materials' mechanical

response to tensile loading as a function of irregularity. We use the image processing software, FIJI, to measure the amount of crack surface opened (Figure 4.5a-c) under tensile strain (Figure 4.5d-h, Figure C.3), and we observe that coordination number and time-to-failure are inversely related (Figure 4.5i). It is important to note that cracks do not initiate at the interface between the two phases, due to their high interfacial toughness^[42], but instead nucleate in the matrix phase and then propagate to the reinforcing phase. Lower coordination samples tend to nucleate cracks sooner than higher coordination samples and open a larger amount of total crack area, with as much as 2.38 ± 0.92 times the original cross section opened for 2H_2X (Figure 4.5j). This is a result of the bending-dominated response of the network, which can continue to elongate after the adjacent matrix phase fractures, with up to 8.67 ± 0.36 times longer from first crack nucleation to loss of load-bearing capacity in the samples for 2H_2X when compared with 6H_6X (Figure 4.5i).

In contrast, although higher coordination samples also initiate cracks first in the matrix phase and then the reinforcing phase, these samples open up less cross section area, with 5H_5X only opening up 2.07 ± 0.42 times the original cross section of area, while 6H_6X opens up one crack across the entire cross section, although the Poisson ratio reduces this value below the original 300 mm^2 cross section. These higher coordination samples also fail more quickly after the first crack nucleation, with 5H_5X losing all load-bearing capacity 1.53 ± 0.09 times faster than 2H_2X, and 1.94 ± 0.41 times faster than 3H_3X. This trend is even more pronounced for the periodic 6H_6X case, which loses all load-bearing capacity within just 28.67 ± 2.31 seconds after crack nucleation, an order of magnitude faster than all other samples (Figure 4.5i). This trend for the periodic case is independent of volume fraction, as shown by the equivalent 2X, 3X, 4X, and 5X volume fraction samples with 6X coordination (Figure 4.5d-h, dashed lines).

Across both the bending and stretching-dominated regimes, the arrangement of the reinforcing phase into an irregular network instead of a periodic network provides a significant temporal benefit, preventing sudden loss of load-bearing capacity. We measure the average crack area opening rate and observe that higher coordinations tend to have a higher rate, with 6H_6X having the fastest rate of nearly 10 mm^2 per second (Figure 4.5k). This is likely the result of the load-bearing pathways in the irregular composites, which reach a wider radius of node connections, creating a more diffuse structural response^[43]. In contrast, the periodic equivalents have nodes which are only connected to the nodes closest to themselves. Although these periodic network materials can withstand a higher load, once one node fails, the load bearing capacity drops suddenly and adjacent nodes quickly fail in succession as one crack propagates across the entire sample. The comparison between the periodic and irregular 5X coordination samples demonstrate this best, showing that, although they remain in the stretching-dominated regime, only a small amount of irregularity results in significantly higher strain-to-failure and damage tolerance, as the composites are able to maintain load bearing capacity after crack nucleation and propagation (Figure 4.5b,c). Instead of failing suddenly, these samples nucleate many crack locations, with up to 2.95 ± 0.87 times the original cross section of crack surface area distributed across the sample, preventing site coalescence (Figure 4.5j).

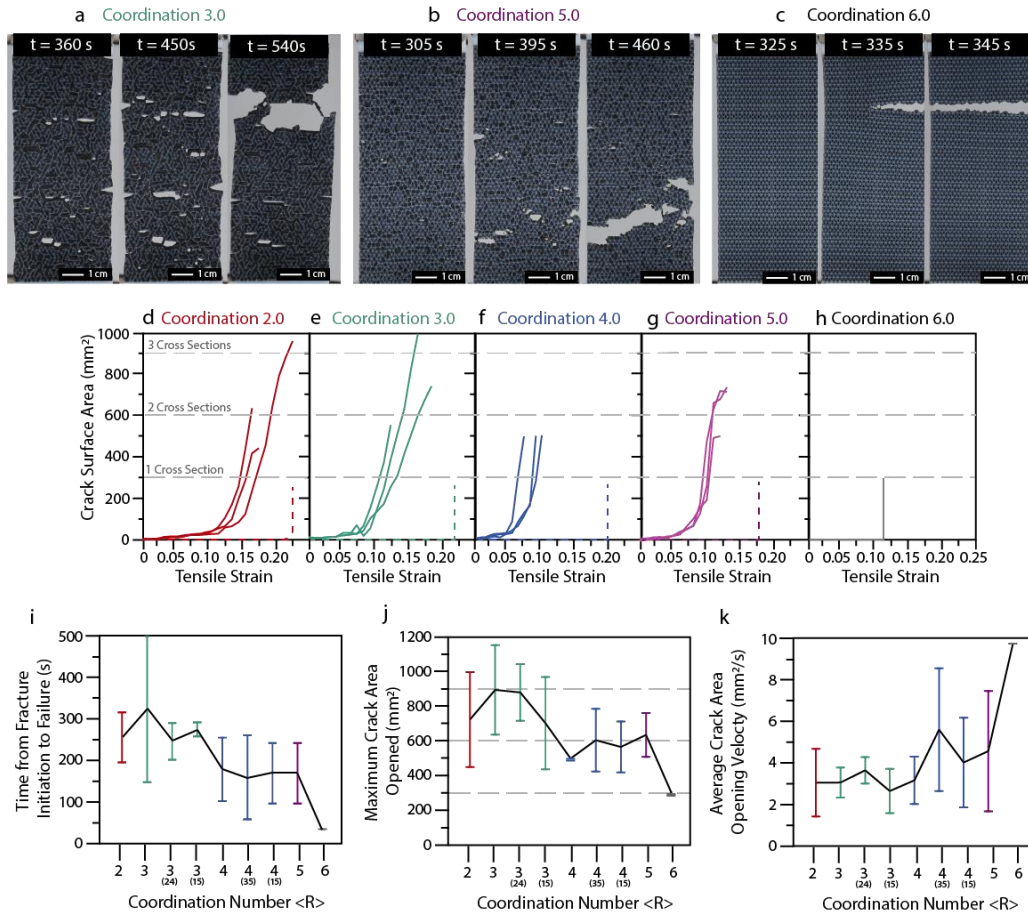


Figure 4.5: Temporal characterization of irregular network composite fracture response. (a-c) Time evolution of crack nucleation and propagation for example 3H_3X, 5H_5X, and 6H_6X composites. (d-h) Crack surface area opened as a function of tensile strain for homogeneous coordination samples, dashed lines show periodic volume fraction equivalent 6H_6X samples. (i) Time from fracture initiation to complete loss of load-bearing capacity in all samples. (j) Maximum crack area opened. (k) Average crack area opening rate for all samples.

4.4 Conclusions

We presented architected network reinforced composite materials and explored the role of irregularity and topology on their mechanical performance. We generated the materials using a hexagonal virtual growth algorithm to achieve control over the topology, using the average network coordination number as an input parameter and varying the local topology to achieve various structural feature polydispersities.

We observed that the effect of local topology variations in iso-coordination samples was less influential on the global mechanical response than the average coordination number. We also observed that introducing irregularity leads to improved damage tolerance across both the bending and stretching-dominated regimes. Irregular composites were able to maintain more load bearing capacity even after cracks nucleated and propagated, as the nucleation sites were more dispersed when compared with periodic equivalents. We also showed that this dispersed fracture response leads to variations in the temporal response, which can be controlled as a function of coordination number to achieve an improved mechanical response when compared with periodic equivalents.

Acknowledgements

The authors thank P. Arakelian for the experimental assistance. C.F. and C.D. acknowledge MURI ARO W911NF-22-2-0109 for the financial support. T. M. acknowledges Dr. R. Style for fruitful discussions.

BIBLIOGRAPHY

- [1] V. S. Deshpande, M. F. Ashby, N. A. Fleck, *Acta Mater* **2001**, *49*, 1035.
- [2] L. J. Gibson, M. F. Ashby, *Proc R Soc Lond A Math Phys Sci* **1982**, *382*, 43.
- [3] L. J. Gibson, M. F. Ashby, G. S. Schajer, C. I. Robertson, *Proceedings of the Royal Society of London. A. Mathematical and Physical Sciences* **1982**, *382*, 25.
- [4] M. R. O'Masta, L. Dong, L. St-Pierre, H. N. G. Wadley, V. S. Deshpande, *J Mech Phys Solids* **2017**, *98*, 271.
- [5] J. Jung, A. Chen, G. X. Gu, *Materials Today* **2024**.
- [6] G. X. Gu, M. Takaffoli, M. J. Buehler, *Advanced Materials* **2017**, *29*.
- [7] T. Magrini, A. Senol, R. Style, F. Bouville, A. R. Studart, *J Mech Phys Solids* **2022**, *159*, 104750.
- [8] T. Li, Y. Chen, L. Wang, *Compos Sci Technol* **2018**, *167*, 251.
- [9] V. S. Deshpande, N. A. Fleck, M. F. Ashby, *J Mech Phys Solids* **2001**, *49*, 1747.
- [10] L. R. Meza, S. Das, J. R. Greer, *Science* **2014**, *345*, 1322.
- [11] I. Christodoulou, P. J. Tan, *Eng Fract Mech* **2013**, *104*, 140.
- [12] W. Chen, S. Watts, J. A. Jackson, W. L. Smith, D. A. Tortorelli, C. M. Spadaccini, *Sci Adv* **2019**, *5*.
- [13] S. Fulco, M. K. Budzik, H. Xiao, D. J. Durian, K. T. Turner, *PNAS Nexus* **2025**, *4*.
- [14] S. Choukir, N. Manohara, C. V. Singh, *Appl Mater Today* **2025**, *42*, 102579.
- [15] W. Deng, S. Kumar, A. Vallone, D. M. Kochmann, J. R. Greer, *Advanced Materials* **2024**, *36*, 2308149.
- [16] C. Fox, T. Magrini, C. Daraio, *arXiv*, **2024**, preprint arXiv:2410.09061.
- [17] T. Magrini, C. Fox, A. Wihardja, A. Kolli, C. Daraio, *Advanced Materials* **2023**, *2305198*.

- [18] C. Fox, K. Chen, M. Antonini, T. Magrini, C. Daraio, *Advanced Materials* **2024**, 2405567.
- [19] A. Guell Izard, J. Bauer, C. Crook, V. Turlo, L. Valdevit, A. Guell Izard, J. Bauer, L. Valdevit, C. Crook, V. Turlo, *Small* **2019**, *15*, 1903834.
- [20] M. T. Hsieh, B. Endo, Y. Zhang, J. Bauer, L. Valdevit, *J Mech Phys Solids* **2019**, *125*, 401.
- [21] Y. Zhang, M. T. Hsieh, L. Valdevit, *Compos Struct* **2021**, *263*, 113693.
- [22] G. Wang, L. Shen, J. Zhao, H. Liang, D. Xie, Z. Tian, C. Wang, *ACS Biomaterials* **2018**.
- [23] I. Christodoulou, P. J. Tan, *Eng Fract Mech* **2013**, *104*, 140.
- [24] K. Karapiperis, D. M. Kochmann, *Communications Engineering 2023 2:1* **2023**, *2*, 1.
- [25] K. Liu, R. Sun, C. Daraio, *Science* **2022**, *377*, 975.
- [26] R. Wang, Y. Bian, K. Liu, *J Appl Mech* **2025**, 1.
- [27] Y. Jia, K. Liu, X. S. Zhang, *J Mech Phys Solids* **2024**, *192*, 105787.
- [28] X. Wang, Z. Li, X. Guo, X. Li, Z. Wang, *Extreme Mech Lett* **2024**, *72*, 102227.
- [29] Y. Jia, K. Liu, X. S. Zhang, *Comput Methods Appl Mech Eng* **2024**, *425*, 116864.
- [30] Y. Jia, K. Liu, X. S. Zhang, *J Mech Phys Solids* **2024**, *192*, 105787.
- [31] M. Thorpe, P. Duxbury, *Rigidity Theory and Applications* **2002**.
- [32] M. F. Thorpe, *J Non Cryst Solids* **1983**, *57*, 355.
- [33] J. C. M. F.R.S., *The London, Edinburgh, and Dublin Philosophical Magazine and Journal of Science* **1864**, *27*, 294.
- [34] C. Fox, K. Bastawros, T. Magrini, C. Daraio, *arXiv*, **2025**, preprint arXiv: 2502.18392.
- [35] J. R. C. Dizon, A. H. Espera, Q. Chen, R. C. Advincula, *Addit Manuf* **2018**, *20*, 44.
- [36] D. Bell, T. Siegmund, *Addit Manuf* **2018**, *21*, 658.
- [37] V. Slesarenko, S. Rudykh, *Int J Eng Sci* **2018**, *123*, 62.

- [38] L. Jiaying Tan, W. Zhu, K. Zhou, L. J. Tan, W. Zhu, K. Zhou, *Adv Funct Mater* **2020**, *30*, 2003062.
- [39] A. Brodin, A. Nych, U. Ognysta, B. Lev, V. Nazarenko, M. Skarabot, I. Muševič, *Condens Matter Phys* **2010**, *13*, 1.
- [40] A. Shrivastava, *Introduction to Plastics Engineering* **2018**, 17.
- [41] R. G. Gilbert, M. Hess, A. D. Jenkins, R. G. Jones, P. Kratochvíl, R. F. T. Stepto, *Pure and Applied Chemistry* **2009**, *81*, 351.
- [42] R. J. Nash, Y. Li, *Eng Fract Mech* **2021**, *253*, 107912.
- [43] M. M. Driscoll, B. G. G. Chen, T. H. Beuman, S. Ulrich, S. R. Nagel, V. Vitelli, *Proc Natl Acad Sci* **2016**, *113*, 10813.

*Chapter 5***EXTRACTING GEOMETRY AND TOPOLOGY OF ORANGE PERICARPS FOR THE DESIGN OF BIOINSPIRED ENERGY ABSORBING MATERIALS**

C. Fox, K. Chen, M. Antonini, T. Magrini & C. Daraio, (2024). “Extracting Geometry and Topology of Orange Pericarps for the Design of Bioinspired Energy Absorbing Materials”. *Advanced Materials* 36 (36), 2405567. doi: 10.1002/adma.202405567.

C.F. participated in the conceptualization, design, fabrication, and testing of samples, data analysis and visualization, and in writing and revising the manuscript.

Chapter Abstract

As a result of evolution, many biological materials have developed irregular structures that lead to outstanding mechanical performances, like high stiffness-to-weight ratios and good energy absorption. However, reproducing these irregular biological structures in synthetic materials remains a complex design and fabrication challenge. We present here a bioinspired material design method that characterizes the irregular structure as a network of building blocks, also known as tiles, and rules to connect them. Rather than replicating the biological structure one-to-one, we generate synthetic materials with the same distributions of tiles and connectivity rules as the biological material and we show that these equivalent materials have structure-to-property relationships similar to the biological ones. To demonstrate the method, we study the pericarp of the orange, a member of the citrus family known for its protective, energy-absorbing capabilities. We generate polymer samples and characterize them under quasi-static and dynamic compression and observe spatially-varying stiffness and good energy absorption, as seen in the biological materials. By quantifying which tiles and connectivity rules

locally deform in response to loading, we also determine how to spatially control the stiffness and energy absorption.

5.1 Introduction

Nature provides many examples of materials with desirable mechanical properties, such as high strength^[1–5], high toughness^[4,6–8], and high impact resistance^[2,9–12]. Some of these materials are periodic, like nacre^[1,4], conch shells^[13], and beetle wings^[5], while others have irregular structures, like trabecular bone^[2,9,10] and citrus pericarp^[14,15]. However, periodic bioinspired materials are more widely studied than irregular materials, as they are more easily fabricated via additive manufacturing^[16–22] and studied computationally^[18,19,21,23–25]. Conversely, generating irregular materials often requires complex biomimicking processes such as micro-computed tomography coupled with 3D printing^[26,27], or investment casting^[28,29]. Other approaches include the use of stochastic processes, such as virtual growth algorithms^[30,31], Voronoi tessellations^[32–34] and foaming^[35–40] for irregular materials generation, but these methods are limited in their ability to imitate the biological structure. Indeed, biological materials are often defined by highly complex and geometrically irregular concave and convex internal structures^[3,11,14,41,42], as well as spatial density variation, optimized to respond to specific loading conditions^[2,15,26,42,43].

Here, we propose a bioinspired material design method that characterizes the irregular biological structure by discretizing it into a network of tiles and rules for how to connect them. The set of available tiles and their connectivity rules lead to materials that, in a stochastic sense, have predetermined topology and geometry. Topology is defined as the connectivity between adjacent tiles, and we quantify it for each tile as the topological coordination number, R , defined as the number of branches, connecting to neighbors from the central node^[44]. Geometry is defined as the shape of elements in the structure, and is relevant at different scales: (i) at the

individual tile level and (ii) after tessellation, at the structural feature level, consisting of assemblies of multiple tiles. Tiling and tessellation approaches that generate irregular geometries have already been studied to achieve mechanical properties such as stiffness and strength^[30,45-49], but these approaches often focus on homogenization or have very limited size due to computational costs^[50], whereas our approach seeks to quantify the structure and its structure-to-property relationships at a local tile level that can be spatially controlled and scaled.

To demonstrate the bioinspired material design method, we focus on the pericarp of the orange, a member of the citrus family^[41]. Citrus fruits are known for their thick pericarps, which range from 5-7 mm for oranges and lemons, to 15-20 mm for the citron (the thickest pericarp)^[51]. Regardless of the type of fruit, these thick pericarps consist of an irregular, density-graded foam-like structure, which has evolved for energy absorption and impact resistance, key to protecting the pulp when the ripe fruit falls from the tree^[15,51]. The dense outer layer of the pericarp, known as the flavedo, acts as a protective layer, while the less dense internal region, known as the albedo, provides energy absorption due to the presence of large, compressible intercellular spaces^[15]. Furthermore, vascular bundles throughout the structure act as reinforcing elements, providing additional strength and stiffness^[15]. We determine the tiles and connectivity rules of the orange pericarp and then use these as instructions for a computer-aided virtual growth algorithm (VGA)^[30] to generate equivalent synthetic samples with the same tile and connectivity rule distributions as the fruit, which we then additively manufacture. Under quasi-static and dynamic compression, we observe spatially-varying stiffness and energy absorption similar to that of the biological material, indicating that the tiles and connectivity rules are sufficient structural descriptors for the mechanical properties. We then quantify which tiles and connectivity rules produce a particular property

by examining the local deformation to understand how to spatially control the mechanical performance.

5.2 Methods, Results and Discussion

5.2.1 Bioinspired Material Design

We begin with a two-dimensional cross-sectional image of an orange pericarp, acquired transversely from the external surface to approximately 5 mm into the fruit, where the pericarp transitions into the pulp (Figure 5.2a; Figure D.1, Appendix D.2.1). We use the image processing software, FIJI^[52], to skeletonize^[53] the structure into a simplified line form of the original pericarp image (Figure 5.1a). This irregular image skeleton is then broken down using a uniform square grid into a collection of tiles (Figure 5.1b,c). The tile size is determined by taking the largest possible size while ensuring that each tile contains no more than one node, defined here as an intersection point between branches (Figure 5.1b). Although each tile contains a unique portion of the original orange pericarp image, all tiles can be reduced to the simplest set of five tile types (Figure 5.1d). Each tile in the reduced set has the same branch thickness, which was chosen to match the volume fraction of the orange pericarp's structure, so that the branch length to thickness ratio is maintained when the tiles are assembled at any scale. We perform the translation process between the original tiles and the reduced tiles by analyzing the tile perimeter, counting the number branch intersections, and assigning a binary code value to the left (1), top (10), right (100), and bottom (1000), or zero otherwise (Figure 5.1d). By summing the perimeter values for each unique biological tile, we can determine its coordination number^[63], as well as its orientation (Figure 5.1f, Appendix D.2.2). Next, we determine the connectivity rules governing how the tiles are assembled by examining the frequency at which two tiles are adjacent in the biological structure (Figure 5.1e,g, Appendix D.2.2). The frequency of the tiles and the rules that determine their connectivity, two parameters that can be extracted

endocarp and pulp begin. Using the gridded approach on eight different equivalent pericarp images (Figure D.1), we determine that the external region is composed of $20.6 \pm 1.3\%$ of coordination number zero (0-R) tiles, $34.8 \pm 1.2\%$ of coordination number two (2-R) tiles, $34.7 \pm 1.4\%$ of coordination number three (3-R) tiles, and $10.0 \pm 1.0\%$ of coordination number four (4-R) tiles (Figure 5.2d, blue). The internal region is composed of $26.6 \pm 1.6\%$ of 0-R tiles, $36.9 \pm 1.3\%$ of 2-R tiles, $28.2 \pm 1.4\%$ of 3-R tiles, and $8.3 \pm 0.9\%$ of 4-R tiles (Figure 5.2d, orange). Although all connectivity rules occur at some point in the original orange pericarp, the current virtual growth algorithm assembles tiles based on either allowed or disallowed connections. As such, to help with accurately capturing the geometry of the original sample and avoid defects during tessellation, we have a limit for when to keep or remove a connectivity rule. If the connectivity rule appears less than 5% of the time, it is automatically removed, while if it appears less than 15%, it is removed only if either of the two tile coordination types that make up the rule appear in other connectivity rules. In the external region, all connectivity rules are included except between 0-R tiles and 0-R tiles, and between 4-R tiles and 4-R tiles (Figure 5.2e, blue). In the internal region, all connectivity rules are included except between 3-R tiles and 4-R tiles, and 4-R tiles and 4-R tiles (Figure 5.2e, orange). With the tile frequencies and connectivity rules extracted from the two different regions of the orange pericarp, a computer-aided virtual growth algorithm^[30] uses the set of five tile types to generate 50x50 tile samples for the external (VGA-ext) and the internal (VGA-int) regions (Figure 5.2f,g). These samples are then combined together to form the bioinspired equivalent of the orange pericarp (VGA-full): a continuous structure with interface-free, spatially-varying density and structural features, defined as the areas enclosed by cell walls (Figure 5.2h). We 3D print the VGA-generated geometries into a two-phase composite material to create a structure suitable for mechanical testing, image analysis, and strain mapping. We use a polyjet printer (Stratasys Objet500 Connex3), with a stiff viscoelastic resin (Stratasys VeroWhite Polyjet Resin) for the reinforcing structure, and a soft

elastomeric resin (Stratasys TangoBlack Polyjet Resin) for the matrix, both of whose mechanical properties fall within those reported in literature^[54-56].

Although we exactly imitate the topology of the original sample by matching tile percentages, we must also quantify how well the VGA-generated samples' geometry compares with the original orange pericarp. For this, we use two different metrics: density, as a measure of structural feature size, and concavity, as a measure of structural feature shape. We observe that the VGA-generated samples maintain the same density difference between the external and internal regions as the orange pericarp samples, with 3-5% lower density in the internal region as a result of the larger structural features (Figure 5.2i). To compare the concavity of the original samples with the VGA-generated samples, we examine each structural feature, using the bridge length to Euclidean distance ratio, where the bridge length is the length of a structural feature's edge between 3-R and 3-R or 4-R nodes, and the Euclidean distance is the linear distance between the 3-R and 3-R or 4-R nodes (Figure D.2). A ratio value of 1 indicates no concavity, whereas a higher ratio indicates a greater degree of concavity. When compared with the orange pericarp's structural features, the VGA-generated samples are very similar, with average concavity values within 2% for both regions, and with the internal region features having significantly higher concavity than the external region features (Figure 5.2j). We also observe that the orange pericarp and the VGA-generated samples have an isotropic distribution of structural features, which can be shown by examining the orientation of the structural features averaged over several samples to determine how the features are distributed. Using the orientation of an elliptic fit in MATLAB (MathWorks, USA), we observe a uniform distribution of structural feature orientations in the internal region, while the distribution is more bimodal (0° and 180°) in the external region (Figure D.3). This bimodal distribution is due to the extensive presence of small, circular cells, but it is an artefact, as circular cells are inherently isotropic. Although the angles of orientation show a uniform distribution, they are not an independently sufficient metric to confirm an isotropic material

distribution, because they do not consider the effect of feature size. Therefore, we also verify that the orientation angles do not correspond to a certain structural feature size to ensure isotropy. There is no correlation between size and angle in the orange pericarp internal and external regions, or in the VGA-int samples, although there is a slight correlation for angles of 0° , 45° , 90° , and 135° in the VGA-ext samples, due to the four-sided nature of the virtual growth algorithm coupled with higher coordination number resulting in lower polydispersity (Figure D.3). Finally, it should be noted that the internal region VGA samples *individually* are not isotropic because their mechanical response is dominated by a few of the largest features, due to testing size limitations (Figure D.4).

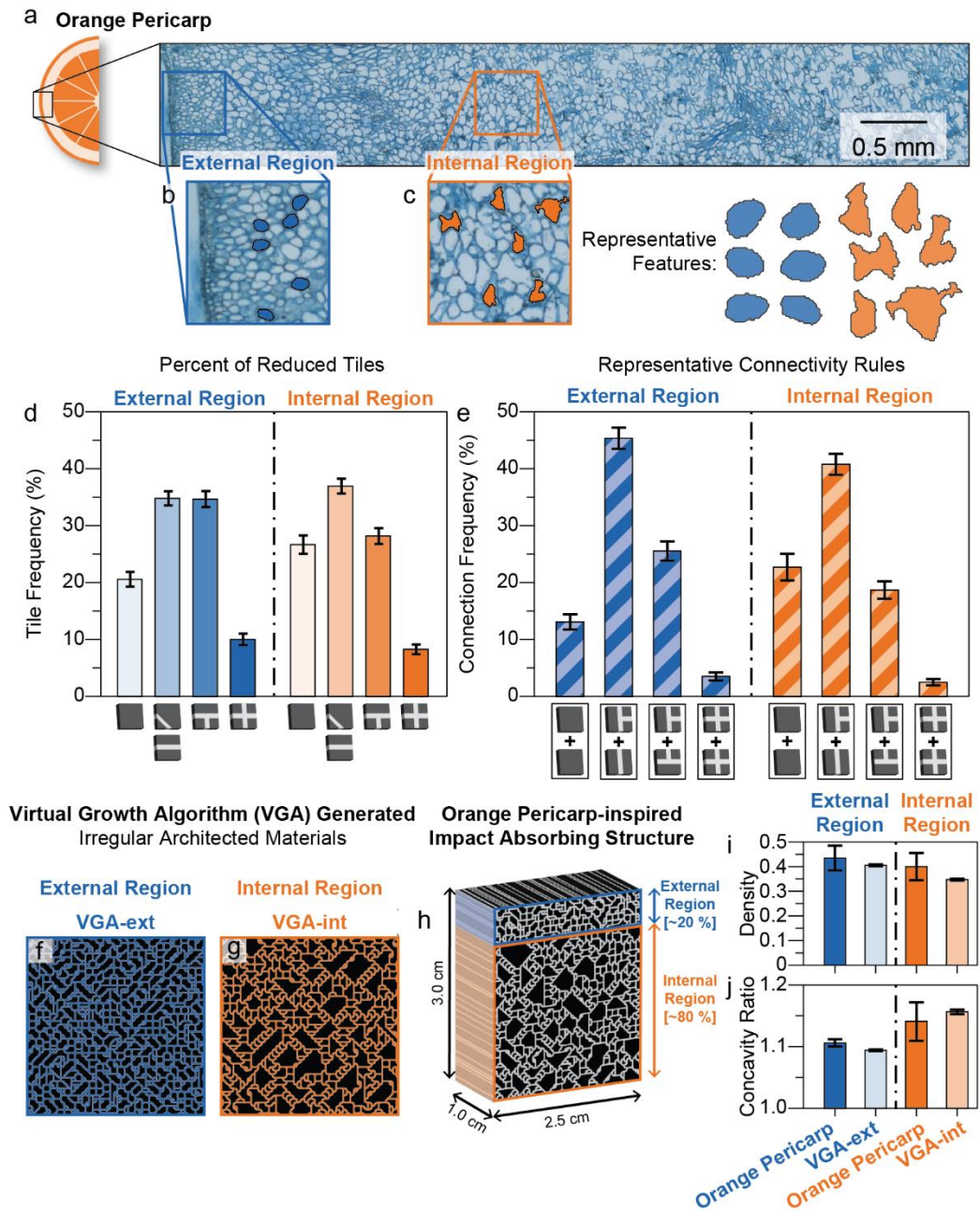


Figure 5.2: Orange pericarp characterization and VGA sample generation. (a) Cross-sectional image of orange pericarp. (b) Representative image of external region. (c) Representative image of internal region. (d) Tile percentages for external and internal regions. (e) Selected connectivity rule percentages for external and internal regions. (f) VGA-generated sample of external region. (g) VGA-generated sample of internal region. (h) 3D-printed composite polymer sample with 80% +

20% external and internal regions, respectively. (i) External and internal region density for orange pericarp and VGA samples. (j) External and internal region concavity ratio for orange pericarp and VGA samples.

5.2.3 Mechanical Characterization: Quasi-static Testing

After establishing the topology and geometry equivalence of the VGA-generated samples with the original orange pericarp samples, we conduct quasi-static compression tests on additively manufactured polymer composite samples (Appendix D.2.3). Like the original orange pericarp, which features a stiff, protective flavedo^[15,41], VGA-ext samples prove to be 116% stiffer than the VGA-int samples (Figure 5.3a,b, respectively) and even when normalized for their difference in density, VGA-int samples prove more compliant, like the energy-absorbing albedo of the orange pericarp^[14,15,51]. The orange pericarp inspired samples, VGA-full, featuring a 20% external and 80% internal composition, have a stiffness that is between the VGA-ext and VGA-int samples (Figure 5.3c). The constitutive stress-strain plots for VGA-full samples with a different composition, featuring 10% external and 90% internal, as well as 50% external and 50% internal, also have an intermediate stiffness (Figure D.6). We also quantify which tiles and connectivity rules are primarily responsible for the stiffness variations by examining the local feature deformation. We do this by quantifying the strain field experienced by each sample up to 10% total strain, using 2D digital image correlation (2D DIC) to identify which features are the stiffest (and undergo the least deformation) and which features are the least stiff (and undergo the most deformation) (Figure 5.3d,e,f, Appendix D.2.4). We then break down these features into their constitutive tiles and connectivity rules and identify which tiles and rules appear in a feature, according to the amount of strain. 2D DIC shows that the strain field in VGA-ext samples is more uniformly distributed, with no region exceeding 15% local strain at a global strain of 10% (Figure 5.3d, III) and that the samples are more homogeneously composed of many smaller stretching-dominated^[31] structural features (Figure 5.3d), like the protective flavedo and reinforcing vascular bundles

of the orange pericarp^[15]. These features are formed by high percentages of high coordination tiles and by limiting large consecutive 0-R and 2-R tile connections, which results in lower polydispersity and local structural feature coordination numbers from ~ 2 up to 3.5 (Figure 5.3d, III, insets). The local structural feature coordination number is calculated from the average of all tiles that compose a given structural feature.

In contrast, VGA-int samples display a significantly more localized strain field, with certain structural features reaching up to 30% local strain, although these local regions of high strain are uniformly distributed across the sample (Figure 5.3e, III, insets). This is in contrast to the periodic and graded honeycomb samples tested under the same loading conditions, which begin to form local shear bands (Figure D.5). We can observe that the VGA-int samples are composed of larger structural features, like the highly compressible, large intercellular spaces of the orange pericarp^[15], formed by higher percentages of low coordination tiles and large consecutive 0-R tile connections, as well as by consecutively aligned tiles (such as 2-R to 2-R, or 3-R to 3-R) or by consecutively repeating two-tile combinations (such as repetitions of the same 2-R to 3-R pair), which prevents the diversion of feature edges (Figure 5.3e, III, insets). This results in local coordination numbers as low as ~ 1.5 , allowing for less stiff bending and buckling mechanisms^[57], as well as higher polydispersity (Figure 5.3e, III, insets). Furthermore, the largest, most deformed structural features have many concave edges, formed by the connection of diagonal 2-R tiles with 3-R tiles, which act as less-constrained joints^[58,59] that can rotate as the feature deforms (Figure 5.3e, III, insets). Finally, the VGA-full sample shows the same trends, with the internal region displaying highly localized strain values up to 30% (Figure 5.3f, III, insets), while the external region never exceeds 15% local strain.

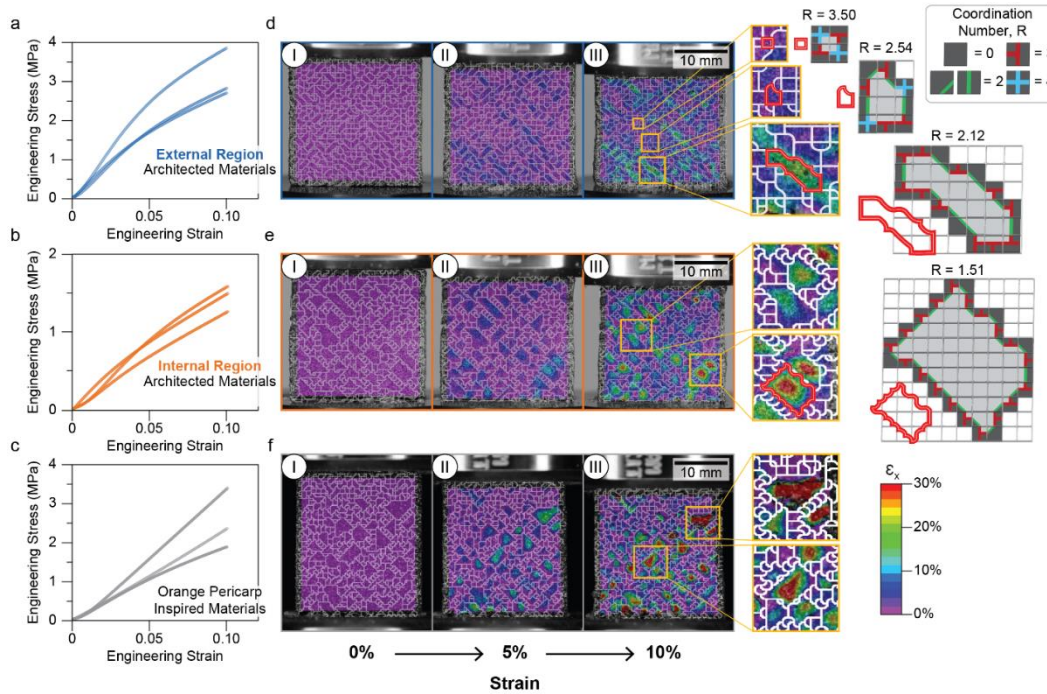


Figure 5.3: Quasi-static compression tests. (a) VGA-ext engineering stress-strain plot for three different samples. (b) VGA-int engineering stress-strain plot for three different samples. (c) VGA-full engineering stress-strain plot for three different samples. (d) Example 2D DIC strain maps for 0%, 5%, and 10% global strain for VGA-ext sample, yellow insets show coordination color coded example structural features. (e) Example 2D DIC strain maps for 0%, 5%, and 10% global strain for VGA-int sample, yellow insets show concave structural features at high strain and coordination color coded example structural feature. (f) Example 2D DIC strain maps for 0%, 5%, and 10% global strain for VGA-full sample, yellow insets show concave structural features at high strain.

5.2.4 Mechanical Characterization: Structural Feature Analysis

We conduct computational simulations of the samples using the COMSOL 2D linear elastic solid mechanics module to gain further understanding of the deformation mechanisms of the individual structural features and their effect on the global mechanical performance under compressive loading (Figure 5.4b,d). To validate the computational results, we first manually track the bending angles of several structural features in the experimentally-tested VGA-generated samples

(Figure 5.4a,c) using the image processing software, FIJI^[52]. Although the experimental samples are composite materials, the simulated bending angle results on just the reinforcing phase are a close match because the matrix phase is significantly less stiff and does not play a significant role in the bending of features at low strain (Figure 5.4e). As the strain increases, the bending angles display varying changes, with some increasing, then decreasing, some remaining relatively constant, while yet others only increase or only decrease (Figure 5.4e). We then computationally study the distributions of all structural features in the samples using the eccentricity in MATLAB (MathWorks, USA) from elliptic fits of each feature as a proxy for bending angle (Figure 5.4f, g, left). We observe that the distribution of eccentricities remains similar across all strains, the result of some features becoming more elongated while others become more circular with increasing strain, making the material locally anisotropic but globally isotropic (Figure 5.4g, left). This is in contrast to the honeycomb, whose distribution shifts up (Figure 5.4g, right) as every feature becomes more elongated with increasing strain.

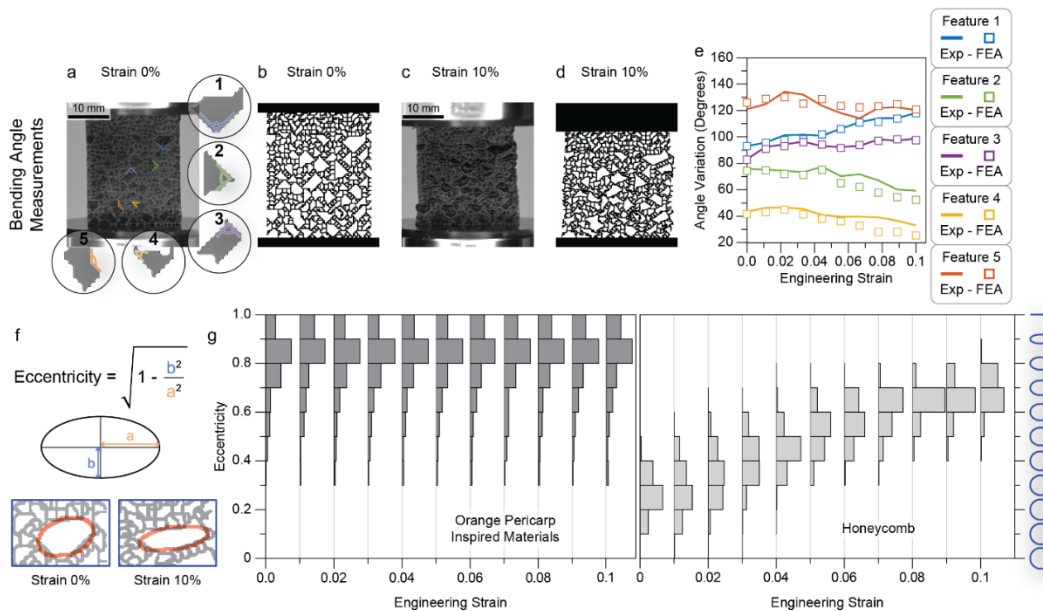


Figure 5.4: Experimental and finite element analysis of changes in structural feature morphology under quasi-static compressive loading. (a,c) Experimental testing of VGA-full structural features from 0% to 10% global strain, insets show example features with example bending angles. (b,d) Finite element analysis of VGA-full reinforcing phase structural features from 0% to 10% global strain. (e) Comparison of experimental and finite element analysis of variations in bending angle of example structural features from 0% to 10% global strain. (f) Defining elliptic fit of structural features and their resulting eccentricity as a way to measure structural feature deformation. (g) Tracking the eccentricity of all structural features from 0% to 10% global strain in the VGA-full reinforcing phase (left) and in honeycomb reinforcing phase (right).

5.2.5 Mechanical Characterization: Dynamic Testing

To characterize the energy absorption capabilities of the VGA-generated samples, drop tower tests at a strain rate of $\sim 100 \text{ s}^{-1}$ are conducted. To quantify the energy absorption capabilities of the VGA-generated materials, we measure the time of contact between the striker and sample, and the coefficient of restitution, defined as the ratio of the average striker velocity 2 ms before and after impact. The velocities are measured using the image processing software, FIJI^[52], by reslicing a vertical line through the center of each image (Figure 5.5a, vertical dashed line). Evaluating the evolution of pixel values over the experiment duration allows us to temporally track the striker position (Figure 5.5b). The VGA-generated samples are tested along with a periodic honeycomb sample and a 20% + 80% graded honeycomb sample, both with the same volume fraction of reinforcing phase as the 20% + 80% VGA-full sample, for comparison. After normalizing for density, we observe that the VGA-ext samples have the highest coefficient of restitution (0.45 ± 0.03), indicating the least amount of energy dissipated (Figure 5.5c), along with the shortest time in contact (Figure 5.5d). Despite having the same volume fraction of reinforcing- and matrix phases, the VGA-full samples have a 7.5% lower coefficient of restitution (0.37 ± 0.02) than their periodic equivalent (0.40 ± 0.01), as well as a 16% longer time in contact, and a 9.8% lower coefficient of restitution (0.41 ± 0.03) than their graded equivalent, as well as a 25% longer time in contact

(Figure 5.5c,d). The similarity in behavior of the periodic honeycomb and the graded honeycomb is because the branch thickness is always maintained, and there is a density difference of less than 10% between the two regions. We also test the 10% and 90% as well as 50% and 50% combination samples of external and internal regions to compare the coefficients of restitution (Figure D.6, Appendix D.2.5). To explain these differences in energy absorption, we observe a positive correlation between structural feature size, overall sample concavity and amount of deformation, noting that higher concavity leads to less constrained strut bending and buckling in the largest structural features (Figure 5.5e,f), like the large, compressible intercellular spaces of the orange pericarp, known for their energy dissipation^[15]. The high percentages of low coordination tiles and consecutively repeating aligned tiles or two-tile combinations are responsible for the large size, while the connection of diagonal 2-R tiles with 3-R tiles are responsible for the high concavity (Figure 5.5g). Indeed, the largest structural features have local coordination numbers as low as 1.28 (Figure 5.5f, I) and concavity ratios as high as 1.17 (Figure 5.5f, IV). To quantify the strain and structural feature deformation, we can also refer back to the quasi-static 2D DIC maps (Figure 5.3d,e,f), as well as the computational results (Figure 5.4e,g) which are valid also at our drop tower strain rate since the striker velocity is between 7-8 m/s and the elastic wave speed in the material is approximately 575 m/s, indicating that drop tower loading occurs slowly enough to reach a state of stress equilibrium (Figure D.7, Appendix D.2.6).

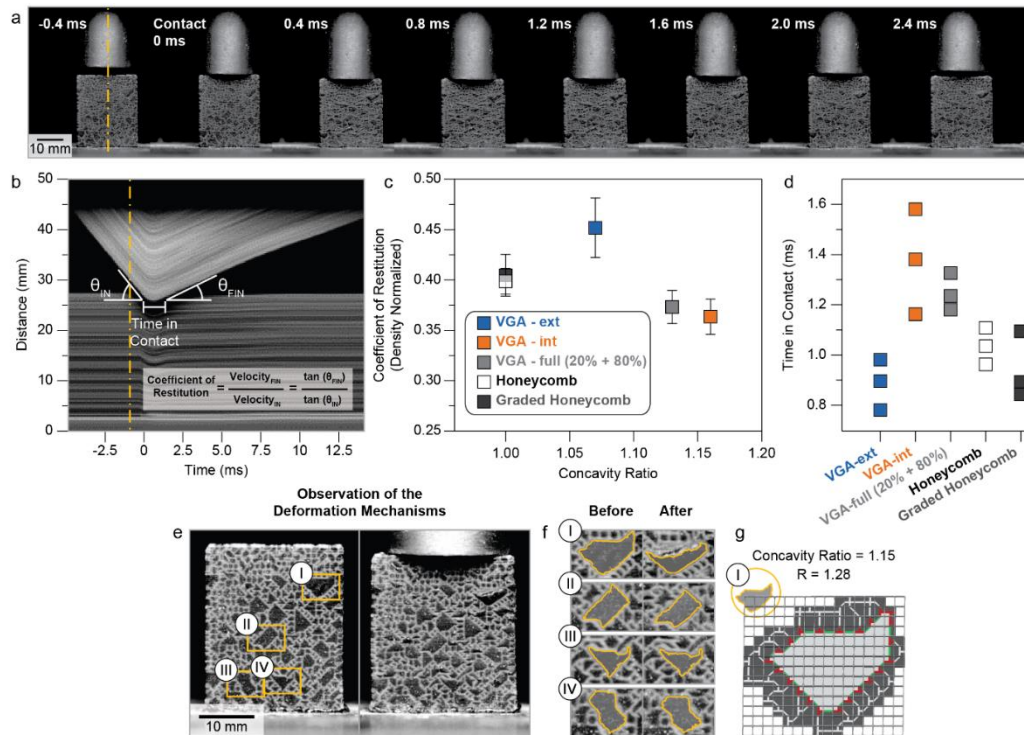


Figure 5.5: Drop tower testing. (a) VGA-full samples before, during and after loading. (b) Time versus distance of resliced striker/sample center axis with time in contact, and angles giving striker initial and final velocities. (c) Coefficient of restitution normalized for density for VGA-ext, VGA-int, VGA-full, and honeycomb polymer composite samples as a function of concavity ratio. (d) Striker time in contact with sample for VGA-ext, VGA-int, VGA-full, and honeycomb polymer composite samples. (e) VGA-full samples before and at maximum strain with highlighted large structural features. (f) Highlighted large structural features before and at maximum strain. (g) Coordination color coded tiling of largest structural feature.

5.3 Conclusions

We present a bioinspired material design method to achieve the desirable mechanical performances of irregular biological materials in synthetic materials. Instead of mimicking the biological structure one-to-one, our synthetic structures match the statistical distributions of features to obtain structure-to-property relationships similar to the biological material. Although this article only explores

the irregular structure of the orange pericarp and its mechanical performance, the method is easily extendable to other irregular biological materials with desirable mechanical properties in 2D and 3D. Furthermore, this method lends itself to spatially-controlled bioinspired materials that combine the tiles and connectivity rules of multiple different materials simultaneously, to locally and globally tailor mechanical properties.

Acknowledgements

The authors thank P. Arakelian, K. Ainger, A. Groetsch, L. Valdevit, and A. Motter for helpful discussions. The authors acknowledge MURI ARO W911NF-22-2-0109 for the financial support. T.M. acknowledges the Swiss National Science Foundation for the financial support (SNSF Postdoc.Mobility Fellowship, P500PT_203197/1).

BIBLIOGRAPHY

- [1] M. A. Meyers, A. Y. M. Lin, P. Y. Chen, J. Muyor, *J Mech Behav Biomed Mater* **2008**, *1*, 76.
- [2] T. M. Keaveny, E. F. Morgan, G. L. Niebur, O. C. Yeh, *Annual Review of Biomedical Engineering* **2003**, *3*, 307.
- [3] T. Magrini, R. Libanori, A. Kan, A. R. Studart, *Revista Brasileira de Ensino de Fisica* **2021**, *43*, 1.
- [4] A. P. J. Ackson, J. F. V Vincent, R. M. T. Uner, *Proc R Soc Lond B Biol Sci* **1988**, *234*, 415.
- [5] J. Chen, J. Xie, Z. Wu, E. M. A. Elbashiry, Y. Lu, *Materials Science and Engineering: C* **2015**, *55*, 605.
- [6] F. Barthelat, H. Tang, P. D. Zavattieri, C. M. Li, H. D. Espinosa, *J Mech Phys Solids* **2007**, *55*, 306.
- [7] I. Jäger, P. Fratzl, *Biophys J* **2000**, *79*, 1737.
- [8] F. Barthelat, R. Rabiei, *J Mech Phys Solids* **2011**, *59*, 829.
- [9] N. H. Hart, S. Nimphius, T. Rantalainen, A. Ireland, A. Siafarikas, R. U. Newton, *J Musculoskelet Neuronal Interact* **2017**, *17*, 114.
- [10] R. Oftadeh, M. Perez-Viloria, J. C. Villa-Camacho, A. Vaziri, A. Nazarian, *J Biomech Eng* **2015**, *137*, 0108021.
- [11] M. Thielen, T. Speck, R. Seidel, *J Mater Sci* **2013**, *48*, 3469.
- [12] M. Thielen, T. Speck, R. Seidel, *J Mater Sci* **2014**, 49.
- [13] S. Kamat, X. Su, R. Ballarini, A. H. Heuer, *Nature* **2000**, *405*, 1036.
- [14] M. Jentsch, S. Becker, M. Thielen, T. Speck, *Plants* **2022**, *11*, 991.
- [15] M. Jentsch, V. Albiez, T. C. Kardamakis, T. Speck, *Soft Matter* **2024**, *20*, 2804.
- [16] T. Magrini, A. Senol, R. Style, F. Bouville, A. R. Studart, *J Mech Phys Solids* **2022**, *159*, 104750.

- [17] T. Magrini, F. Bouville, A. Lauria, H. Le Ferrand, T. P. Niebel, A. R. Studart, *Nature Communications* **2019**, *10*, 1.
- [18] F. Li, C. Yu, J. Zhong, C. Zhao, *Mechanics of Advanced Materials and Structures* **2024**.
- [19] G. X. Gu, M. Takaffoli, M. J. Buehler, *Advanced Materials* **2017**, *29*, 1700060.
- [20] F. Bouville, E. Maire, S. Meille, B. Van De Moortèle, A. J. Stevenson, S. Deville, *Nature Materials* **2014**, *13*, 508.
- [21] S. Lee, D. D. Lim, E. Pegg, G. X. Gu, *Cell Rep Phys Sci* **2022**, *3*, 101152.
- [22] M. Li, N. Zhao, M. Wang, X. Dai, H. Bai, *Adv Funct Mater* **2022**.
- [23] D. Gao, P. Chen, G. Lu, H. Yang, *Mater Today Commun* **2023**, *35*, 106031.
- [24] H. Jiang, Y. Ren, Q. Jin, G. Zhu, Y. Hu, F. Cheng, *Thin-Walled Structures* **2020**, *154*, 106911.
- [25] H. Dai, W. Dai, Z. Hu, W. Zhang, G. Zhang, R. Guo, *Advanced Science* **2023**, *10*.
- [26] N. Kumar, A. Kumar, P. Uniyal, B. Ramalingaiah, S. Sharma, V. G. Goni, S. Aggarwal, S. K. Bhadada, B. Bhushan, *Philosophical Transactions of the Royal Society A* **2020**, 378.
- [27] A. Mao, N. Zhao, Y. Liang, H. Bai, *Advanced Materials* **2021**, 33.
- [28] S. F. Fischer, M. Thielen, R. R. Loprang, R. Seidel, C. Fleck, T. Speck, A. Bührig-Polaczek, *Adv Eng Mater* **2010**, *12*, B658.
- [29] S. F. Fischer, M. Thielen, P. Weiß, R. Seidel, T. Speck, A. Bührig-Polaczek, M. Bünck, *J Mater Sci* **2014**, *49*, 43.
- [30] K. Liu, R. Sun, C. Daraio, *Science* **2022**, *377*, 975.
- [31] T. Magrini, C. Fox, A. Wihardja, A. Kolli, C. Daraio, *Advanced Materials* **2023**, 2305198.
- [32] H. X. Zhu, A. H. Windle, *Acta Mater* **2002**, *50*, 1041.
- [33] H. X. Zhu, J. R. Hobdell, A. H. Windle, *Acta Mater* **2000**, *48*, 4893.
- [34] K. Li, X. L. Gao, J. Wang, *Int J Solids Struct* **2007**, *44*, 5003.

- [35] H. Rhee, M. T. Tucker, W. R. Whittington, M. F. Horstemeyer, H. Lim, *Science and Engineering of Composite Materials* **2015**, 22, 365.
- [36] M. Bianchi, F. Scarpa, C. W. Smith, *Acta Mater* **2010**, 58, 858.
- [37] J. A. Carpenter, Z. Saraw, A. Schwegler, T. Magrini, G. Kuhn, A. Rafsanjani, A. R. Studart, J. A. Carpenter, Z. Saraw, A. Schwegler, T. Magrini, A. R. Studart, G. Kuhn, A. Rafsanjani, *Advanced Materials* **2023**, 35, 2207181.
- [38] A. Dutto, M. Zanini, E. Jeoffroy, E. Tervoort, S. A. Mhatre, Z. B. Seibold, M. Bechthold, A. R. Studart, A. Dutto, E. Tervoort, A. R. Studart, M. Zanini, E. Jeoffroy, S. A. Mhatre, Z. B. Seibold, M. Bechthold, *Adv Mater Technol* **2023**, 8, 2201109.
- [39] Z. Zhuang, Z. Qian, X. Wang, X. Xu, B. Chen, G. Song, X. Liu, L. Ren, L. Ren, *Advanced Science* **2023**.
- [40] J. Zhao, M. Li, J. Chen, W. Gao, H. Bai, *Nano Research* **2023**, 17, 679.
- [41] F. M. Scott, K. C. Baker, *Botanical Gazette* **1947**, 108, 459.
- [42] W. J. Whitehouse, *J Microsc* **1974**, 101, 153.
- [43] H. Zhao, Y. Han, C. Pan, D. Yang, H. Wang, T. Wang, X. Zeng, P. Su, *Micromachines (Basel)* **2021**, 12.
- [44] M. F. Thorpe, *J Non Cryst Solids* **1983**, 57, 355.
- [45] H. Lu, T.-U. Lee, J. Ma, Y. M. Xie, *Eng Struct* **2024**, 304, 117686.
- [46] M. Doškář, J. Zeman, D. Jarušková, J. Novák, *European Journal of Mechanics - A/Solids* **2018**, 70, 280.
- [47] Z. Chen, A. Ogren, C. Daraio, L. C. Brinson, C. Rudin, *Extreme Mech Lett* **2022**, 57, 101895.
- [48] T. Li, Y. Li, *Advanced Materials* **2024**, 2309604.
- [49] J. Jung, A. Chen, G. X. Gu, *Materials Today* **2024**.
- [50] H. Pahlavani, K. Tsifoutis-Kazolis, M. C. Saldivar, P. Mody, J. Zhou, M. J. Mirzaali, A. A. Zadpoor, H. Pahlavani, K. Tsifoutis-Kazolis, M. C. Saldivar, J. Zhou, M. J. Mirzaali, A. A. Zadpoor, P. Mody, *Advanced Materials* **2024**, 36, 2303481.

- [51] M. Jentzsch, M. C. Badstöber, F. Umlas, T. Speck, *Front Mater* **2022**, *9*, 979151.
- [52] C. A. Schneider, W. S. Rasband, K. W. Eliceiri, *Nature Methods* **2012**, *9*, 671.
- [53] I. Arganda-Carreras, R. Fernández-González, A. Muñoz-Barrutia, C. Ortiz-De-Solorzano, *Microsc Res Tech* **2010**, *73*, 1019.
- [54] J. R. C. Dizon, A. H. Espera, Q. Chen, R. C. Advincula, *Addit Manuf* **2018**, *20*, 44.
- [55] D. Bell, T. Siegmund, *Addit Manuf* **2018**, *21*, 658.
- [56] V. Slesarenko, S. Rudykh, *Int J Eng Sci* **2018**, *123*, 62.
- [57] V. S. Deshpande, M. F. Ashby, N. A. Fleck, *Acta Mater* **2001**, *49*, 1035.
- [58] C. R. Calladine, *Int J Solids Struct* **1978**, *14*, 161.
- [59] J. C. M. F.R.S., *The London, Edinburgh, and Dublin Philosophical Magazine and Journal of Science* **1864**, *27*, 294.

*Chapter 6***CONTROLLABLE INTERLOCKING FROM IRREGULARITY IN TWO-PHASE COMPOSITES**

C. Fox, K. Bastawros, T. Magrini & C. Daraio, (2025). “Controllable Interlocking from Irregularity in Two-Phase Composites” *Matter* (Accepted).

doi: 10.48550/arXiv.2502.18392.

C.F. participated in the conceptualization, design, fabrication, and testing of samples, data analysis and visualization, and in writing and revising the manuscript.

Chapter Abstract

Natural materials often feature a combination of soft and stiff phases, arranged to achieve excellent mechanical properties, such as high strength and toughness. Many natural materials have even independently evolved to have similar structures to obtain these properties. For example, interlocking structures are observed in many strong and tough natural materials, across a wide range of length scales. Inspired by these materials, we present a class of two-phase composites with controllable interlocking. The composites feature tessellations of stiff particles connected by a soft matrix and we control the degree of interlocking through irregularity of particle size, geometry and arrangement. We generate the composites through stochastic network growth, using an algorithm which connects a hexagonal grid of nodes according to a coordination number, defined as the average number of connections per node. The generated network forms the soft matrix phase of the composites, while the areas enclosed by the network form the stiff reinforcing particles. At low coordination, composites feature highly polydisperse particles with irregular geometries, which are arranged non-periodically. In response to loading, these particles interlock with each other and primarily rotate and deform to accommodate non-uniform kinematic constraints from adjacent particles. In contrast, higher coordination composites feature more monodisperse particles with

uniform geometries, which collectively slide. We then show how to control the degree of interlocking as a function of coordination number alone, demonstrating how irregularity facilitates controllability.

6.1 Introduction

Nature offers an abundance of materials with excellent mechanical properties, including high stiffness^[1–6], high strength^[2–4,7–11], high toughness^[1,4,5,10,12–15], and good energy absorption^[16–18]. These materials are often composed of stiff and soft phases, arranged to optimize mechanical performance. Many biological materials have even independently evolved to have similar structures across a wide range of length scales^[19]. For example, interlocking structures that provide excellent mechanical performances can be observed in many different biological materials, providing high strength, ductility, and toughness^[19]. In nacre, interlocking occurs as a result of rough, wavy tablets, which jam as they slide past one another^[1,20,21], while in turtle carapaces and cranial bone, interlocking is seen in zigzag bone interfaces, which engage like puzzle pieces for improved bending strength and toughness^[11,14,22]. Interlocking is even seen in stomatopod dactyl clubs, which feature bouligand and herringbone structures that deflect cracks with out-of-plane interlocked layer arrangement^[23,24]. However, mimicking all of these advantageous biological structures for use in bioinspired engineering materials remains a complex design and fabrication challenge.

Here we propose the use of irregularity to generate bioinspired interlocking materials, and we present a class of two-phase composites composed of tessellations of stiff reinforcing particles connected by a soft matrix. Going one step beyond the biological materials, we show that our materials offer control over the degree of interlocking, defined as the kinematic constraints provided by neighboring particles^[25,26], through control of particle size, geometry and

arrangement. We generate the materials using a virtual growth algorithm (VGA), which mimics the growth of stochastic structures observed in nature by assembling simple building blocks into a network according to connectivity rules^[27–31]. To further increase the design space, we present a VGA on a hexagonal grid (hexa-VGA), offering up to 6-sided connectivity. The hexa-VGA begins with a set of nodes on the hexagonal grid and randomly assigns connections from each node until the entire grid is filled, forming a network. We define the average number of connections per node as the coordination number^[32,33], which we use as an input parameter to the hexa-VGA. The generated hexa-VGA network then forms the matrix phase of our composite materials, while the reinforcing particles are formed by the areas enclosed by the matrix.

As a function of coordination, and the resulting particle size, geometry, and arrangement, particles interlock to varying degrees in response to the kinematic constraints provided by neighboring particles. This mechanical performance is reminiscent of not only interlocking biological materials, but also of interlocking engineering materials, which have been previously shown to provide tunable bending stiffness^[34–37], enhanced load-bearing capacity^[36,38–40], and improved toughness^[37,41–45]. However, all of the previous studies on interlocking are all limited by the periodic nature of the interlocking elements, in both the biological materials and the engineering materials. In contrast, our irregular elements (particles) offer a wider design space, with control over the degree of interlocking in response to loading, as a function of coordination number.

6.2 Results and Discussion

6.2.1 Sample Design

To design and generate our samples, we use a hexagonal virtual growth algorithm (hexa-VGA), which stochastically grows a network from a set of nodes on a

hexagonal grid. The hexa-VGA is defined by a coordination number, which is the average number of connections per node (Figure 6.1a). We can therefore define a set of 63 geometrically or rotationally unique hexagonal tiles, which form from the network on the grid (Figure 6.1b,c). To make our polymer composite materials, we additively manufacture the generated network as the soft matrix phase, while the areas enclosed by the network form the stiff reinforcing phase. Further details on the material properties may be found in Appendix E (Figure E.1) and details on generation and fabrication methods may be found in Section 6.4.

To span the available design space, we generate samples with coordinations of 2X, 2.5X, 3X, 3.5X, 4X, 5X, and 6X, which are composed of primarily either 100% the coordination tile type (for integer coordinations) or 50% of the tile type above and 50% of the tile type below (for non-integer coordinations) (Figure 6.1e). The particle size is inversely related to the coordination number, with coordination 2X below the percolation threshold for equilateral triangular networks^[46], resulting in the largest particles (Figure 6.1f). The smallest particle size possible is that of a triangle formed by adjacent lines (Figure 6.1c).

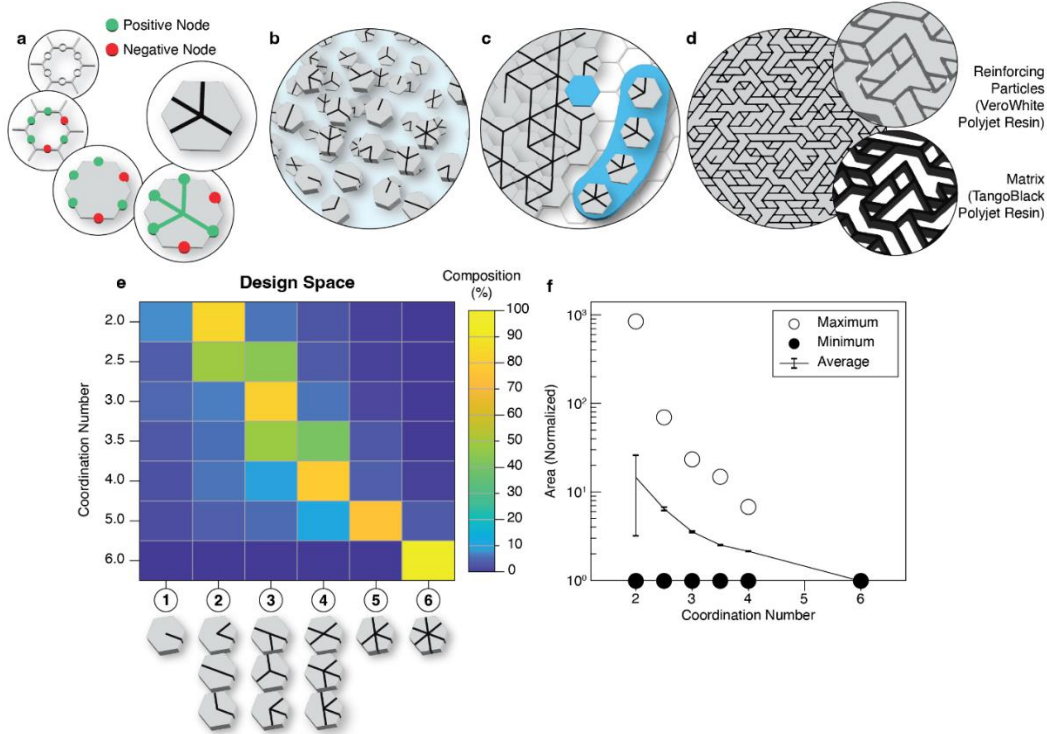


Figure 6.1: Sample generation and characterization of design space. (a) Node identification with positive (green) and negative (red) nodes. (b) Assorted hexagonal tiles. (c) Hexagonal tile connectivity. (d) Composite material generation with reinforcing particles and matrix. (e) Hexa-VGA sample compositions as a function of coordination number. (f) Triangle-normalized particle size distributions as a function of coordination number.

6.2.2 Mechanical Characterization: Cylindrical Contact Loading

Samples are loaded in compression with a cylindrical contact to understand how the structure responds to localized load at displacements up to 3 mm (Figure 6.2a-f). We test three different samples for each coordination (2X, 2.5X, 3X, 3.5X, 4X) and observe that at the lowest coordination, the material behaves similarly to a bulk material, as it falls below the percolation threshold for an equilateral triangular network^[46] and is primarily composed of a few large particles (Figure 6.2a). As coordination number increases, stiffness and strength decrease non-linearly, as a result of both structure and material properties, since the volume fraction of the

reinforcing phase decreases with increasing coordination number (Figure 6.2b-f). To decouple the effect of volume fraction, we test 6X samples with the same volume fraction of reinforcing particles as 2X, 2.5X, 3X, 3.5X, and 4X irregular samples. These equivalent samples are composed of uniform triangular particles of varying sizes, according to the volume fraction of each coordination, and we maintain the same matrix width for all samples. We observe an increase in both stiffness and strength with increasing particle phase volume fraction (Figure E.2), but not as large of an increase in stiffness and strength as observed in the irregular composites (Figure 6.2a-f). These periodic equivalent samples also begin to fail sooner at lower coordinations, resulting in a decrease in measured force, as a result of bands of particles shearing for these periodic materials, rather than their interlocking irregular counterparts.

Given the hexagonal nature of the hexa-VGA used to generate the samples, we examine the effect of orientation by testing samples at 0° (horizontal, blue) and 90° (vertical, red), such that the underlying hexagonal grid is aligned along the widest hexagon direction and the narrowest hexagon direction. At lower coordinations, there is significant anisotropy, with the vertical orientation displaying greater stiffness and strength (Figure 6.2a,b). This trend decreases as coordination number increases (Figure 6.2c-e), until we reach the periodic 6X case, where the vertical orientation reemerges as being stiffer (Figure 6.2f; Figure E.3). This anisotropy effect is likely the result of both particle size, which decreases with coordination, offering a wider range of possible geometries and orientations, while maintaining irregularity at intermediate coordinations, as well as the result of the matrix alignment with respect to the direction of loading, where horizontal alignment allows for greater deformability in the lateral x-direction when loaded from the normal y-direction. We measure the angle of alignment of the particles to quantify this anisotropy. Using `regionprops` in MATLAB (MathWorks, USA) to obtain the angle of orientation, we show that intermediate coordinations have a more uniform

distribution of particle orientations for both alignments, while more extreme coordinations (i.e. 2X and 6X) show more skewed distributions (Figure E.4). These differences in structure and resulting mechanical response (Figure 6.2a-f) offer a way to design materials which primarily deform and fail in a desired direction and with a particular mode, depending on the desired application. For example, it is possible to obtain stronger materials from vertically-aligned lower coordinations which deform primarily through the axial compression of larger vertically-aligned particles, or to obtain weaker materials from horizontally-aligned higher coordinations, which deform through the shearing of smaller diagonally-aligned particles.

We then use 2D digital image correlation (DIC) to track the sample deformation up to 1 mm cylindrical contact displacement (indicated by the gray line in the force-displacement plots). Across the various samples (Figure 6.2g-l, Figure E.5), we observe varying amounts of strain surface area (structural engagement) as a function of coordination number, with intermediate coordinations displaying the largest region of both ϵ_x (Figure 6.2m-r, Figure E.5) and ϵ_y strain (Figure 6.2s-x, Figure E.5).

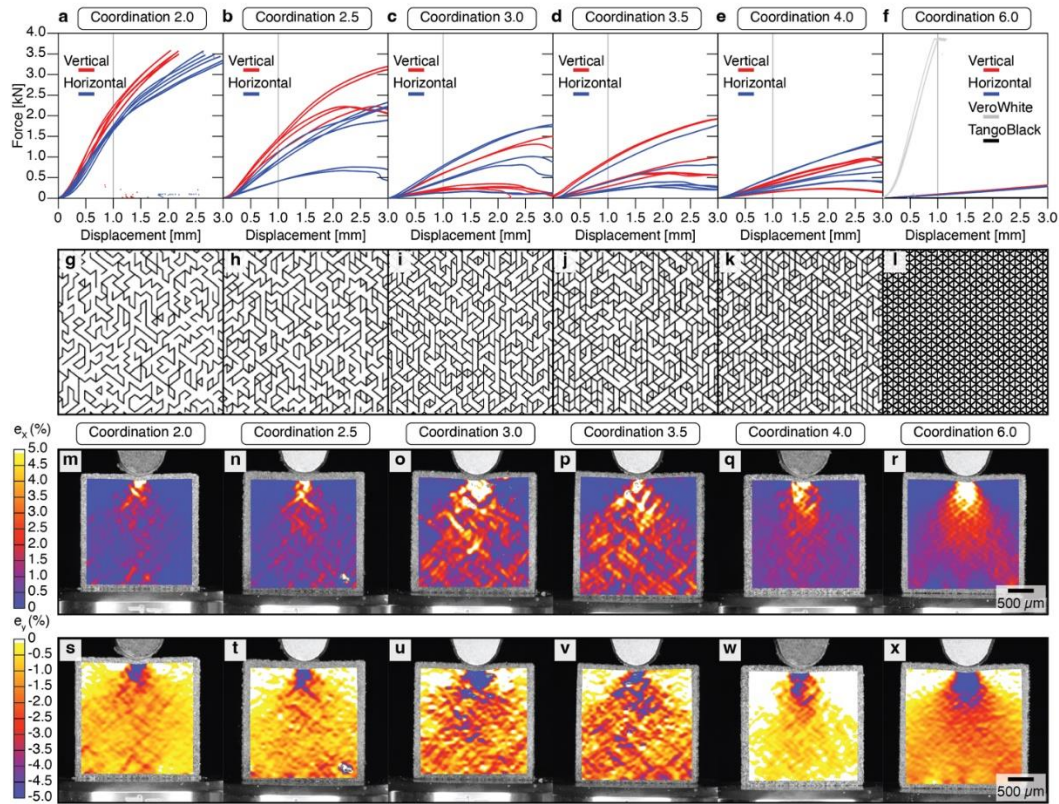


Figure 6.2: Cylindrical contact loading characterization. (a-f) Force-displacement plots for coordinations 2X, 2.5X, 3X, 3.5X, 4X, and 6X, respectively. Red refers to vertical matrix orientation, blue refers to horizontal matrix orientation, gray line highlights 1 mm displacement. (g-l) Selected samples with vertical orientation. (m-r) 2D DIC maps of ϵ_x strain for corresponding selected samples. (s-x) 2D DIC maps of ϵ_y strain for corresponding selected samples.

6.2.3 Mechanical Characterization: Matrix Response

To understand the reason for the non-linear trend in the structural engagement, we first characterize the matrix response as a function of coordination number. The matrix response (i.e. regions of non-zero strain) gives us an indication about how the particles are interacting and how many particles are engaging to accommodate the loading. The strain surface maps can be masked to obtain the strain maps of exclusively the soft matrix (Figure 6.a-c). After normalizing for the volume fraction of matrix in each sample, we observe that matrix engagement (defined as non-zero

matrix strain across the sample surface area) follows the same trend as the overall structure engagement and varies with coordination number. The lowest values occurring at 6X, followed by 2X, and the greatest values occurring around 3X to 3.5X, once we reach a cylindrical contact displacement greater than 0.33 mm, for both ε_x and ε_y strain (Figure 6.2d,e). This peak of matrix engagement is likely the result of particle geometries and arrangement, whose irregularity leads a series of kinematic constraints as particles engage with neighboring particles, distributing strain over a large amount of the sample. We also compare these irregular composites with their periodic counterparts to understand the role of particle interlocking. In response to loading, the 6X equivalent volume fraction samples display exclusively collective sliding behavior, resulting in shear bands forming, similar to that of the original 6X samples (Figure E.6). We then measure the amount of matrix engagement as a function of volume fraction to quantify the extent of the interlocking mechanism and decouple the effect of interlocking from the intrinsic material properties. We observe a nearly linear trend in the amount of matrix engagement in the periodic samples, unlike the trend with a peak around the intermediate coordinations in the irregular samples (Figure E.7). This discrepancy in trends between the periodic and irregular samples can therefore be attributed to the activation of the interlocking mechanism, which are in competition with the collective sliding mechanism in the irregular samples. It is also important to note that the total percent of matrix engagement in the periodic samples is higher than in the irregular samples, especially at lower coordinations, but the number of particles is also greater in the periodic samples. This means that although the total amount of matrix engaged is higher, the number of particles interacting per unit of matrix engagement is actually lower.

To further quantify how the matrix distributes strain across the structure, we also measure the average strain across the sample depth. At 1 mm cylindrical contact displacement, we first convert the strain maps to grayscale values in MATLAB

(MathWorks, USA) and then collapse the strain maps to a vertical line, where darker values indicate greater amounts of strain (Figure 6.2f-k). We observe that intermediate coordinations also display the greatest depth of matrix engagement (Figure 6.2l), with maxima around 3X and 3.5X (Figure 6.2m). This again indicates that these intermediate coordinations engage the largest amount of the composite structure in response to the cylindrical contact loading.

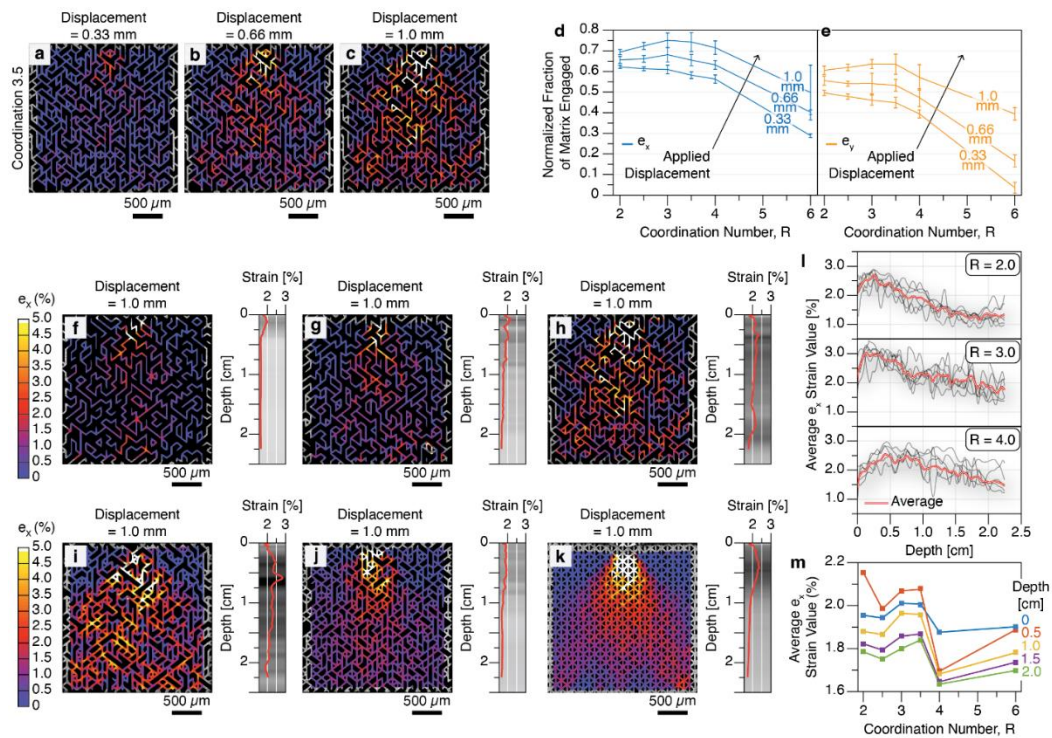


Figure 6.3: Matrix response characterization. (a-c) Example 3.5X matrix ϵ_x strain with increasing cylindrical contact displacement. (d) Volume normalized fraction of matrix engaged as a function of coordination number and cylindrical contact displacement for ϵ_x strain. (e) Volume normalized fraction of matrix engaged as a function of coordination number and cylindrical contact displacement for ϵ_y strain. (f-k) Example 2X, 2.5X, 3X, 3.5X, 4X, and 6X matrix ϵ_x strains at 1 mm cylindrical contact displacement with corresponding horizontally averaged ϵ_x strain values (grayscale bars with line plot average). (l) Average ϵ_x strain value as a function of depth for all 2X, 3X, and 4X coordinations at 1 mm cylindrical contact displacement. (m) Average ϵ_x strain value as a function of coordination number for all 2X, 3X, and 4X coordinations at various sample depths.

6.2.4 Mechanical Characterization: Particle Response

We then examine the particle response to further understand the relationship between coordination number and how the structure accommodates the applied loading. In this study, we focused on the low-strain regime, and therefore it is important to note the tough matrix-particle interface does not fracture during loading^[47] and particles remain adhered to their surrounding matrix phase throughout our analysis.

The 2X samples are primarily composed of a few large particles, given that they are below the percolation threshold, and behave similarly to a bulk material. As the coordination increases and crosses the percolation threshold, particle number increases and particle size decreases, although lower coordinations (3X) still feature highly polydisperse particles with irregular geometries which are often concave (Figure 6.4a). Under cylindrical contact loading, these low-coordination samples deform as individual particles uniquely translate, rotate and deform to accommodate the non-uniform kinematic constraints provided by neighboring particles. We define the degree to which particles are kinematically constrained by neighboring particles as interlocking^[25,38] and the lower coordinations display the greatest amount of interlocking (Figure 6.4a). To quantify the interlocking behavior, individual particle path vectors can be tracked using FIJI TrackMate^[48], and we can then use these vectors to observe how the particles move relative to one another (Figure 6.4b). Greater interlocking results in a particle vector that is more dissimilar to neighboring particle vectors, resulting in a wide distribution of vector angles in a local region (Figure 6.4c). As the coordination increases further to 4X, particle size continues to decrease, and particles become more uniform in both shape and size (Figure 6.4d). In addition to particle-to-particle interlocking, this uniformity results in the activation of mechanisms of collective particle sliding, due to the reduced neighboring particle kinematic constraints in local regions. This mixed mode behavior is reminiscent of nacre, although the interlocking and collective

sliding of nacre's tablets is a sequential deformation response resulting from monodisperse tablets^[1,9,20,49], rather than a simultaneous tradeoff resulting from polydispersity and irregularity. The mixed mode behavior results in a narrower distribution of particle vector angles, as the collectively sliding particles have more similar angles in a local region (Figure 6.4e,f). At 6X coordination, all particles collectively slide, as all particles are convex and periodically arranged, with uniform shape and size (Figure 6.4g,h), and the distribution of particle vector angles becomes much narrower in a local region (Figure 6.4i).

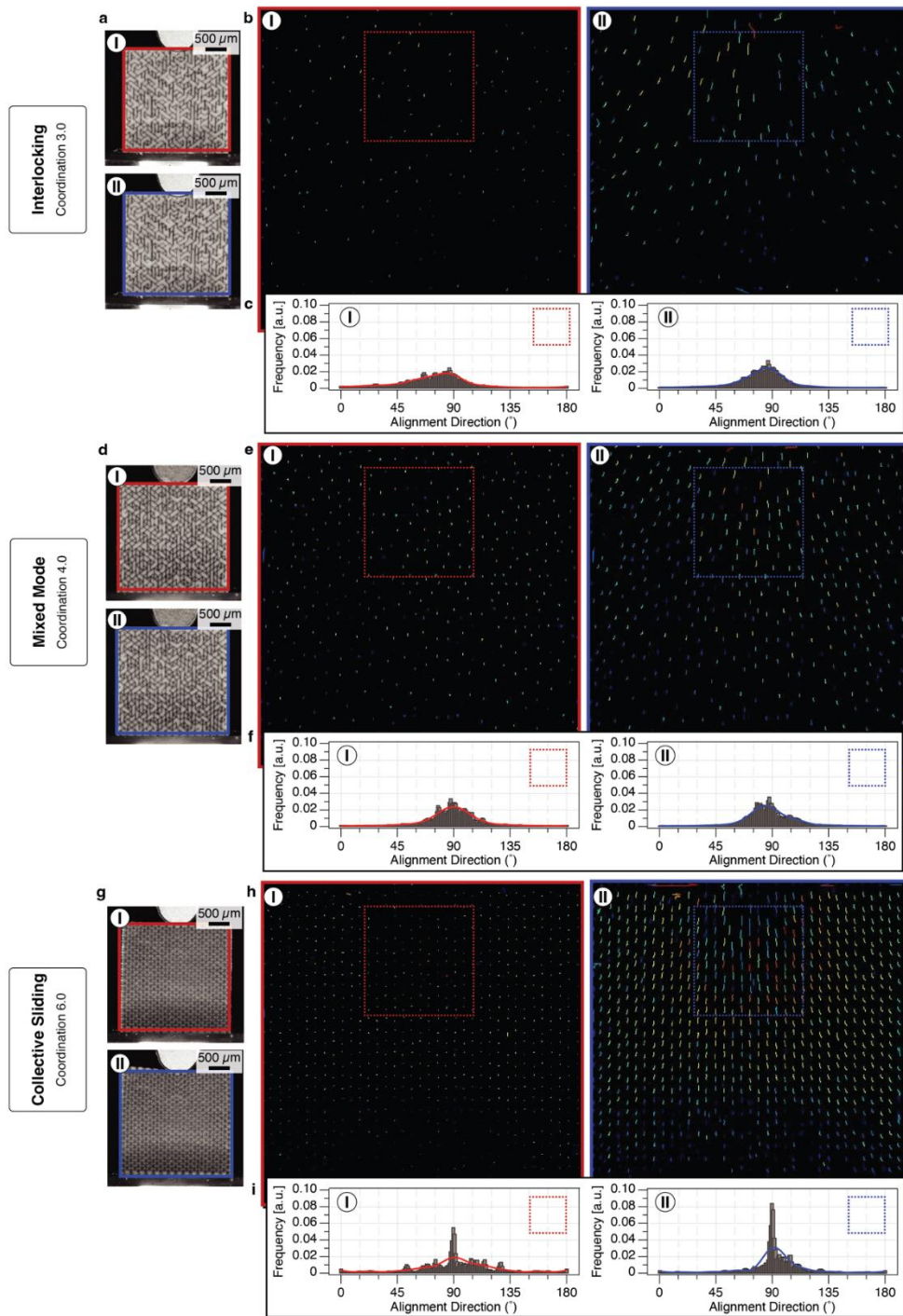


Figure 6.4: Particle response characterization. (a) Example 3X particle image at 0.5 mm (I) and 1 mm (II) cylindrical contact displacement. (b) Corresponding particle vector map at 0.5 mm (I) and at 1 mm (II) displacement. (c) Histogram of

vector map line angle frequencies at 0.5 mm (I) and 1 mm (II) displacement. (d) Example 4X particle image at 0.5 mm (I) and 1 mm (II) displacement. (e) Corresponding particle vector map at 0.5 mm (I) and at 1 mm (II) displacement. (f) Histogram of vector map line angle frequencies at 0.5 mm (I) and 1 mm (II) displacement. (g) Example 6X particle image at 0.5 mm (I) and 1 mm (II) displacement. (h) Corresponding particle vector map at 0.5 mm (I) and at 1 mm (II) displacement. (i) Histogram of vector map line angle frequencies at 0.5 mm (I) and 1 mm (II) displacement.

6.2.5 Mechanical Characterization: Statistical Analysis

To quantify the transition from interlocking to collective sliding behavior in our materials, we examine the statistics behind the particle and matrix arrangement. To reduce interlocking and achieve collective sliding behavior, the matrix must be arranged in continuous straight lines to form planes along which particles can slide. Given an initial matrix orientation on a hexagonal tile, we can therefore determine which subsequent tiles allow the straight line of matrix to continue (Figure 6.5a), and which divert it (Figure 6.5b). With rotational symmetry, regardless of the initial matrix orientation, the tile distributions for continuing or diverting remains the same, resulting in a continuous or discontinuous line of matrix (Figure 6.5c). Given the input parameter of coordination number, which tells us which tile types we have available, we can then calculate the probability of the matrix continuing to determine the average length of matrix lines. We use Bayes theorem,

$$P(R \cap \text{tiling plane}) = \left[\sum_1^i P(\text{tiling plane} | \text{tile type}_i) * P(\text{tile type}_i) \right]^j, \quad (1)$$

where i is the number of tile types, and j is the number of tiles. By placing a threshold at a percent less than 1% likelihood, we can plot the expected length of straight lines of matrix for each coordination type and we can see that the probability increases non-linearly with coordination number (Figure 6.5d). Low coordinations have statistically shorter lines of continuously aligned matrix, resulting in complex geometries that interlock, while higher coordinations have

statistically longer lines, with 6X showing only continuous lines, resulting in collective sliding behavior (Figure 6.5d).

To further understand what gives rise to interlocking behavior and how particles engage with neighboring particles, we also quantify the average number of neighboring particles per particle. Using the Euler characteristic⁵⁰, we determine the number of particles and the number of edges (which correspond to neighbors). The Euler characteristic is defined for a 2D graph as

$$V - E + F = 1, \quad (2)$$

where V is the number of tiles greater than 2X, E is the number of edges, defined as

$$E = \frac{R_c V}{2}, \quad (3)$$

where R_c is the corrected coordination number, found by removing any 2X tiles, which only contribute to the length of the edges but not to the number of edges, and F is the number of particles. F can therefore be rewritten as

$$F = 1 - V\left(1 - \frac{R_c}{2}\right). \quad (4)$$

We then determine the average number of neighboring particles per particle, N (Figure 6.5e):

$$N = \frac{E}{F}. \quad (5)$$

From the Euler characteristic (Equation 2), the maximum average number of neighbors per particle cannot exceed six, and as the corrected coordination number increases above 3X, the maximum number of neighbors per particle decreases, until

we reach a limit of three neighbors at 6X (Figure 6.5f). This follows the trend we observed where the maximum amount of structural engagement occurs at intermediate coordinations. At these coordinations, we have both interlocking particles engaging with a nearly maximum number of neighbors, as well as collectively sliding particles, which easily move in large groups. At these intermediate coordinations, the average particle size also maintains a concave shape, which allows for more kinematic constraints (greater interlocking), formed by more than three triangles (Figure 6.5g). These kinematic constraints then allow the particles to easily distribute the loading to their neighboring particles across the structure.

To find the upper bounds of the design space, we plot together maximum continuous tilings and corresponding neighbors per particle, and we include our tested samples as well as additional samples which were only statistically analyzed (Figure 6.5h). To achieve the greatest degree of interlocking, lower coordinations are desirable, while the lowest degree of interlocking is achieved at 6X, when all particles collectively slide along continuous matrix lines. However, as previously discussed, the greatest amount of structural engagement occurs at intermediate coordinations, when there is a tradeoff between the simultaneous activation of the interlocking and collective sliding mechanisms. It should be noted that the upper limit defined here is for the homogenous case where samples are formed by nearly 100% of their coordination number tile type for integer coordinations or 50% above and 50% below for non-integer coordinations (Figure 6.1e). It is therefore possible to increase the continuous tiling length by forming the same coordination number with other tile compositions that have greater numbers of high coordination tiles, although these may not be feasible to generate using the hexa-VGA.

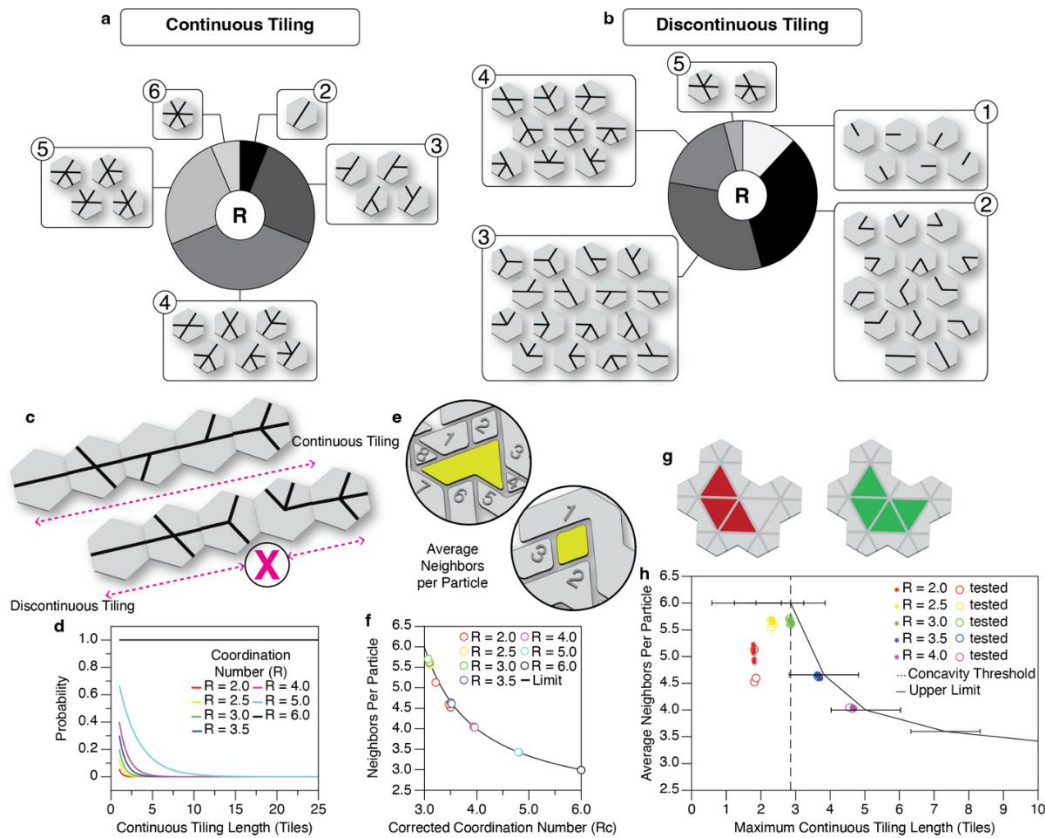


Figure 6.5: Statistical characterization of matrix and particles. (a) Continuous tiles for 60° example matrix plane according to coordination number. (b) Discontinuous tiles for 60° example matrix plane according to coordination number. (c) Example of continuous and discontinuous tiling plane. (d) Probability of continuous tiling as a function of number of tiles for various coordination numbers. (e) Examples of counts of neighboring particles per particle. (f) Neighboring particles per particle as a function of corrected coordination number, solid black line denotes upper limit. (g) Example of convex (red) particle and concave (green) and geometries. (h) Average neighboring particles per particle as a function of maximum continuous tiling, dashed black line denotes concavity threshold, solid black line denotes upper limit.

6.3 Conclusions

We present a class of two-phase composites composed of tessellations of stiff particles connected by a soft matrix. Drawing inspiration from the excellent mechanical performance of interlocking structures observed in many natural materials, our composites feature particle interlocking in response to loading.

Going one step beyond the biological materials, we control the degree of interlocking using irregularity of particle size, geometry, and arrangement. We generate the composites through a hexa-VGA, which stochastically connects a network of nodes on a hexagonal grid according to coordination number. We then use the generated hexa-VGA network as the matrix phase, while the reinforcing particles are formed by the areas enclosed by the matrix. Lower coordinations feature highly polydisperse particles, which interlock as a result of their irregular geometries and non-periodic tessellations. Higher coordinations feature more monodisperse particles, which collectively slide as a result of their more uniform geometries and tessellations. Finally, we show and statistically quantify how to control the tradeoff between these interlocking and sliding mechanisms, with activation of a particular mechanism and the amount of structural engagement controlled by coordination number alone. These findings offer an exciting new research direction, especially for 3D extensions of these 2D findings on controllable interlocking, for new materials with spatially tailorable stiffness, strength, ductility, and toughness.

6.4 Methods

6.4.1 Sample Generation and Fabrication

The hexa-VGA code used to generate the samples is written in Python and may be found at the following link: <https://github.com/basbaskoko/hexaVGA>.

The hexa-VGA generates (irregular) networks by beginning with an equilateral triangular network placed on a hexagonal grid. Lists of unique lines in the network are first defined by their endpoints and then initiated with a status of “neither”. An arbitrary endpoint (a node) is randomly selected, from which, X (out of 6) lines are assigned the status “positive”, while the rest are given the status “negative”. This number X is defined as the coordination number, and we define it on a set of tiles formed by the hexagonal grid. Once a line has been assigned a status, that status

cannot change. After all lines beginning at an endpoint have been assigned a status, that endpoint is removed from the set of “free” endpoints. If any of the neighboring six endpoints are free endpoints, one of them is chosen to have its lines assigned a status. If none of the neighboring endpoints are free endpoints, a random free endpoint is selected, and this process continues until no free endpoints remain and all lines have been assigned a status, resulting in a network of interconnected nodes.

To fabricate our composite samples from the hexa-VGA output network, we first use the network information to create an STL file for the soft matrix, which is made from TangoBlack Polyjet Resin, and then take its negative to form the stiff reinforcing particles, which is made from VeroWhite Polyjet Resin. We conducted simple tension tests to obtain the constitutive stress-strain properties of both resins (Figure E.1) and the mechanical properties of the two phases fall within those reported in literature^[51–53]. Due to printer resolution constraints, we choose a matrix width of 100 μm and a minimum particle width of 1 mm.

It is also important to consider the effect of the sample geometry, given that the fabricated samples have a square shape, while the tiles that tessellate it are hexagonal and therefore cannot perfectly fill the square space, resulting in smaller average edge particle size. However, the number of total tiles is significantly higher than the number of edge tiles, which represent just 18% of the total tile population.

6.4.2 Cylindrical Contact Compression Testing

We use an Instron E3000 with a 5 kN load cell (Instron, USA) to apply compression loading. Samples of 2.5 cm by 2.5 cm by 1 cm are loaded with a cylindrical contact of 1 cm diameter. Testing is conducted for displacements up to 3 mm, which is just prior to fracture. Three different samples are tested for each coordination to ensure consistency across samples.

6.4.3 Digital Image Correlation

To conduct 2D digital image correlation (DIC) on the samples, we apply a layer of matte white paint and then matte black speckles with a diameter of 0.1-0.3 mm to the front face of the samples. During loading, we use a Nikon D750 DSLR camera (Nikon, Japan) with a 120mm lens to take images at a rate of 1 frame per second. We use VIC-2D (Correlated Solutions, USA) to conduct the DIC analysis, using a step size of 2 and a subset size of 29, and obtain the Lagrangian strain fields in the x-direction and y-direction.

Acknowledgements

The authors acknowledge P. Arakelian for experimental assistance. The authors acknowledge MURI ARO W911NF-22-2-0109 for the financial support.

BIBLIOGRAPHY

- [1] F. Barthelat, H. Tang, P. D. Zavattieri, C. M. Li, H. D. Espinosa, *J Mech Phys Solids* **2007**, *55*, 306.
- [2] R. Oftadeh, M. Perez-Viloria, J. C. Villa-Camacho, A. Vaziri, A. Nazarian, *J Biomech Eng* **2015**, *137*, 0108021.
- [3] N. H. Hart, S. Nimphius, T. Rantalainen, A. Ireland, A. Siafarikas, R. U. Newton, *J Musculoskelet Neuronal Interact* **2017**, *17*, 114.
- [4] T. Magrini, R. Libanori, A. Kan, A. R. Studart, *Revista Brasileira de Ensino de Fisica* **2021**, *43*, 1.
- [5] M. E. Launey, M. J. Buehler, R. O. Ritchie, *Annu Rev Mater Res* **2010**, *40*, 25.
- [6] E. Lin, Y. Li, J. C. Weaver, C. Ortiz, M. C. Boyce, *J Mater Res* **2014**, *29*, 1867.
- [7] R. O. Ritchie, *Nature Materials 2011 10:11* **2011**, *10*, 817.
- [8] M. Mirkhalaf, A. K. Dastjerdi, F. Barthelat, *Nature Communications 2014 5:1* **2014**, *5*, 1.
- [9] F. Barthelat, *International Materials Review* **2015**, *60*, 413.
- [10] F. Barthelat, Z. Yin, M. J. Buehler, *Nature Reviews Materials 2016 1:4* **2016**, *1*, 1.
- [11] B. Achrai, B. Bar-On, H. D. Wagner, *J Mech Behav Biomed Mater* **2014**, *30*, 223.
- [12] F. Barthelat, R. Rabiei, *J Mech Phys Solids* **2011**, *59*, 829.
- [13] H. D. Espinosa, J. E. Rim, F. Barthelat, M. J. Buehler, *Prog Mater Sci* **2009**, *54*, 1059.
- [14] I. H. Chen, W. Yang, M. A. Meyers, *Acta Biomater* **2015**, *28*, 2.
- [15] J. Rivera, M. S. Hosseini, D. Restrepo, S. Murata, D. Vasile, D. Y. Parkinson, H. S. Barnard, A. Arakaki, P. Zavattieri, D. Kisailus, *Nature* **2020**, *586*, 543.
- [16] M. Jentzsch, S. Becker, M. Thielen, T. Speck, *Plants 2022, Vol. 11, Page 991* **2022**, *11*, 991.

- [17] M. Thielen, C. N. Z. Schmitt, S. Eckert, T. Speck, R. Seidel, *Bioinspir Biomim* **2013**, *8*.
- [18] N. Lee, M. F. Horstemeyer, H. Rhee, B. Nabors, J. Liao, L. N. Williams, *J R Soc Interface* **2014**, *11*.
- [19] V. Perricone, E. Sarmiento, A. Nguyen, N. C. Hughes, D. Kisailus, *Communications Materials 2024 5:1* **2024**, *5*, 1.
- [20] F. Barthelat, *Bioinspir Biomim* **2010**, *5*.
- [21] H. D. Espinosa, A. L. Juster, F. J. Latourte, O. Y. Loh, D. Gregoire, P. D. Zavattieri, *Nature Communications 2011 2:1* **2011**, *2*, 1.
- [22] T. Miura, C. A. Perlyn, M. Kinboshi, N. Ogihara, M. Kobayashi-Miura, G. M. Morriss-Kay, K. Shiota, *J Anat* **2009**, *215*, 642.
- [23] J. D. Currey, A. Nash, W. Bonfield, *J Mater Sci* **1982**, *17*, 1939.
- [24] L. Amorim, A. Santos, J. P. Nunes, J. C. Viana, *Mater Des* **2021**, *199*, 109336.
- [25] A. V. Dyskin, Y. Estrin, E. Pasternak, *Springer Series in Materials Science* **2019**, *282*, 23.
- [26] Y. Estrin, V. R. Krishnamurthy, E. Akleman, *Journal of Materials Research and Technology* **2021**, *15*, 1165.
- [27] K. Liu, R. Sun, C. Daraio, *Science* **2022**, *377*, 975.
- [28] R. Wang, Y. Bian, K. Liu, *J Appl Mech* **2025**, *1*.
- [29] Y. Jia, K. Liu, X. S. Zhang, *Comput Methods Appl Mech Eng* **2024**, *425*, 116864.
- [30] Y. Jia, K. Liu, X. S. Zhang, *J Mech Phys Solids* **2024**, *192*, 105787.
- [31] C. Fox, K. Chen, M. Antonini, T. Magrini, C. Daraio, *Advanced Materials* **2024**, 2405567.
- [32] M. F. Thorpe, *J Non Cryst Solids* **1983**, *57*, 355.
- [33] M. Thorpe, P. Duxbury, *Rigidity Theory and Applications* **2002**, DOI 10.1007/B115749.
- [34] T. Lu, Z. Zhou, P. Bordeenithikasem, N. Chung, D. F. Franco, J. E. Andrade, C. Daraio, *Extreme Mech Lett* **2024**, *71*, 102212.

- [35] S. Khandelwal, T. Siegmund, R. J. Cipra, J. S. Bolton, *Smart Mater Struct* **2015**, *24*, 045037.
- [36] T. Siegmund, F. Barthelat, R. Cipra, E. Habtour, J. Riddick, *Appl Mech Rev* **2016**, *68*.
- [37] Y. Estrin, Y. Beygelzimer, R. Kulagin, P. Gumbsch, P. Fratzl, Y. Zhu, H. Hahn, *Mater Res Lett* **2021**, *9*, 399.
- [38] Y. Estrin, V. R. Krishnamurthy, E. Akleman, *Journal of Materials Research and Technology* **2021**, *15*, 1165.
- [39] L. Djumas, G. P. Simon, Y. Estrin, A. Molotnikov, *Scientific Reports 2017 7:1* **2017**, *7*, 1.
- [40] S. Feldfogel, K. Karapiperis, J. Andrade, D. S. Kammer, *Int J Solids Struct* **2023**, *269*, 112228.
- [41] A. V. Dyskin, Y. Estrin, A. J. Kanel-Belov, E. Pasternak, *Advanced Engineering Materials* **2001**.
- [42] A. V. Dyskin, Y. Estrin, E. Pasternak, H. C. Khor, A. J. Kanel-Belov, *Adv Eng Mater* **2003**, *5*, 116.
- [43] M. Mirkhalaf, T. Zhou, F. Barthelat, *Proc Natl Acad Sci U S A* **2018**, *115*, 9128.
- [44] J. A. Rosewitz, H. A. Choshali, N. Rahbar, *Cem Concr Compos* **2019**, *96*, 252.
- [45] S. Askarinejad, H. A. Choshali, C. Flavin, N. Rahbar, *Compos Struct* **2018**, *195*, 118.
- [46] M. F. Sykes, ; J W Essam, J. W. Essam, *J Math Phys* **1964**, *5*, 36.
- [47] R. J. Nash, Y. Li, *Eng Fract Mech* **2021**, *253*, 107912.
- [48] D. Ershov, M. S. Phan, J. W. Pylvänäinen, S. U. Rigaud, L. Le Blanc, A. Charles-Orszag, J. R. W. Conway, R. F. Laine, N. H. Roy, D. Bonazzi, G. Duménil, G. Jacquemet, J. Y. Tinevez, *Nature Methods 2022 19:7* **2022**, *19*, 829.
- [49] U. G. K. Wegst, H. Bai, E. Saiz, A. P. Tomsia, R. O. Ritchie, *Nature Materials 2014 14:1* **2014**, *14*, 23.
- [50] L. Euler, *Novi Commentarii academiae scientiarum Petropolitanae* **1758**.

- [51] J. R. C. Dizon, A. H. Espera, Q. Chen, R. C. Advincula, *Addit Manuf* **2018**, 20, 44.
- [52] D. Bell, T. Siegmund, *Addit Manuf* **2018**, 21, 658.
- [53] V. Slesarenko, S. Rudykh, *Int J Eng Sci* **2018**, 123, 62.

Chapter 7

CONCLUSIONS

7.1 Summary of Contributions

This thesis explored the mechanical characterization of irregular architected materials, using topological and geometrical descriptors to understand and control structure-to-property relationships. We first showed how to design and fabricate materials with intentionally architected irregularity using virtual growth algorithms and additive manufacturing. We then explored the characterization of the relationship between the irregular structure and the resulting mechanical properties, investigating both linear and non-linear deformations, including fracture and dynamic impact. Finally, we showed how to tailor these architected materials using irregularity to achieve spatially and temporally controllable mechanical responses.

In Chapter 2, we studied the role of irregular topology and geometry on the mechanical response of the irregular network reinforced polymer composites, including the stiffness, strength, and modulus of toughness. With this understanding of the structure-to-property relationships, we then showed how to modify the network reinforcement at the meso-scale to improve the global mechanical performance, creating assemblies of various network reinforcements with spatially-tuned fracture initiation and propagation. In Chapter 3, we expanded the fracture characterization, obtaining J-integral and R-curve measurements by exploring the role of reinforcement and matrix composition as well as irregular structural feature size and geometry. In Chapter 4, we introduced a hexagonal virtual growth algorithm, which allowed us to explore higher degree topologies. Using this algorithm, we demonstrated how to temporally control the fracture response of the

composites. We also studied the effect of irregularity on damage tolerance, showing that introducing irregularity leads to improved damage tolerance.

We then explored the intersection of irregular materials and bioinspiration. In Chapter 5, we presented a bioinspired materials design method which uses statistical measures of topology and geometry in biological materials in conjunction with stochastic network growth to develop spatially tailorable materials with excellent energy dissipation properties. Finally, in Chapter 6, inspired by tough and strong materials such as nacre and bone, we presented a class of bioinspired interlocking materials, and showed how irregularity gives rise to controllable interlocking in particle-reinforced composites.

7.2 Outlook and Future Research Directions

This thesis primarily explored 2D irregular architected polymer composites and characterized the structure-to-property relationships across both linear and non-linear regimes. Using topological and geometrical measures, we designed and quantified the irregular materials and then showed how to use irregularity to achieve tailorable fracture performance, improve impact absorption, and control deformation mechanisms. With these findings in mind, there are several future research directions to pursue.

First, the virtual growth algorithms used for the chapters of this thesis assembled their irregular structures using a limited set of tiles with simple geometries. Introducing more complex geometries, such as those with greater curvature, variations in strut width, or greater than two phases, could therefore increase the design space, providing a wider range of spatially- and temporally-controllable mechanical performances. Furthermore, the connectivity rules determining the tile assembly are limited to a binary inclusion or exclusion. Introducing tunable control of this parameter (i.e. choosing a percentage of how often to allow a connection)

could also offer a greater degree of control over the design space. The virtual growth algorithms could also be extended to 3D, and indeed some work has already been conducted in this direction to explore 3D truss-based geometries, which are generated using voxels rather than tiles^[1,2]. We envision further expansion of this work beyond the cubic voxel and truss-based designs to other space-filling polyhedral voxels (e.g. hexagonal prism or truncated octahedron), as well as shell-based designs.

We also envision future research on irregular architected materials beyond additively manufactured polymers. While the polymer materials we used have inherent material properties (i.e. Young's modulus, yield strength, and toughness) and display viscoelastic behavior, we studied our irregular structures from a relatively material-agnostic perspective. Therefore, the topological and geometrical measures used to relate structure-to-property relationships could be extended to any class of material across a range of length scales to further develop an understanding of how irregularity gives rise to mechanical performance. Preliminary investigations on additively manufactured metallic network samples show similar deformation localization (for periodic architectures) and delocalization responses (for irregular architectures) (Figure 7.1).

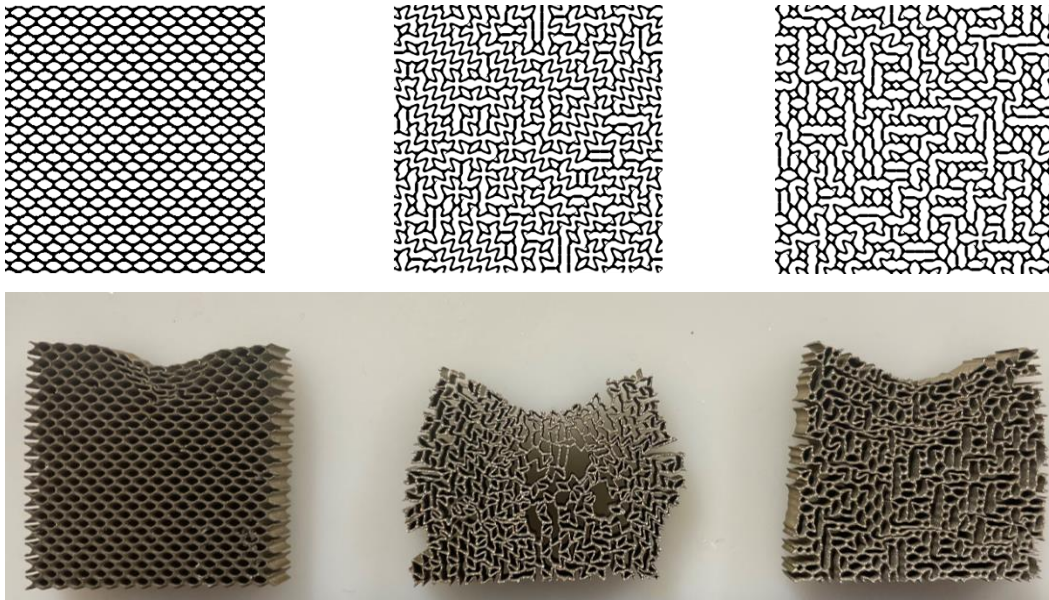


Figure 7.1: Preliminary results of isodensity irregular network metallic samples. (top) VGA-generated periodic (left) and irregular network architectures with low-coordination (center) and high coordination (right). (bottom) Metallic periodic (left) and irregular network samples with low-coordination (center) and high coordination (right).

Another direction that is particularly promising is to extend the idea of controllable interlocking particles to other materials such as ceramics or metals, which have more practical applications, especially under extreme loading conditions. The 2D interlocking materials presented in Chapter 6 could also be extended to 3D in order to design structures with improved toughness, strength, and impact absorption performances. It could also be an interesting direction to explore the use of active materials as one or more of the phases in these irregular materials for the design of spatially or temporally controlled materials which are locally responsive to external stimuli such as light, temperature, or magnetic fields.

Overall, the goal of this thesis was to study the design space of irregular architected materials in order to understand and quantify the relationship between irregularity and mechanical performance. Inspired by the irregular structure of many natural materials, we showed how designing and controlling irregularity allows for spatial

and temporal control of mechanical properties, as well as improved mechanical performances, offering a new design space for future architected materials.

BIBLIOGRAPHY

- [1] Y. Jia, K. Liu, X. S. Zhang, *Comput Methods Appl Mech Eng* **2024**, 425, 116864.
- [2] R. Wang, Y. Bian, K. Liu, *J Appl Mech* **2025**, 1.

*Appendix A***CONTROL OF MECHANICAL AND FRACTURE PROPERTIES
IN TWO-PHASE MATERIALS REINFORCED BY
CONTINUOUS, IRREGULAR NETWORKS****A.1 Experimental Section*****A.1.1 Sample Fabrication***

Samples were generated using the virtual growth algorithm described by Liu et. al.²⁸ and further described in the Section A.3.1. The virtual growth algorithm provides a PNG file of the sample architecture, which is then edited using Adobe Illustrator to smoothen all tile connections, ensuring the same volume fraction of reinforcing phase and matrix phase in each sample. Finally, each phase of the sample is extruded and converted into a separate STL file for printing. The specimens are then printed using a Polyjet printer Stratasys Objet500 Connex3, that has a lateral resolution of 40-85 μm ^[1]. The reinforcing phase and matrix phases are printed from Stratasys VeroWhite Polyjet Resin and Stratasys TangoBlack Polyjet Resin, respectively.

A.1.2 Mechanical Characterization

Uniaxial tension tests were performed on plate geometries of the additively manufactured polymeric composites, with dimensions of 75 mm x 75 mm x 5 mm. An Instron E3000 (Instron, USA) with a 5 kN load cell was used to apply a small preload followed by a quasi-static tensile loading at a rate of 2 mm/min. The measured force and displacements were then used to calculate the tensile engineering stress and strain. The experiments were recorded using a Nikon D750 camera (Nikon, USA) with a Nikkor 120 mm f/4 lens (Nikon, USA) at a rate of 1 frame per second.

A.1.3 Digital Image Correlation

The same camera setup was used to perform 2D digital image correlation (DIC) on equivalent sets of samples. Samples were painted white using flat white spray paint and then speckled using flat black spray paint such that each speckle was approximately 0.1 to 0.3 mm in diameter and would take up approximately 3x3 to 5x5 pixels of each image. VIC-2D digital image correlation software (Correlated Solutions, USA) was used to calculate the displacements and the resulting Lagrangian strain fields across the different substructures, using a subset size of 31 and a step size of 2, which captured the large global deformation while allowing for sufficient resolution of the local deformation.

A.2 Supplementary Figures

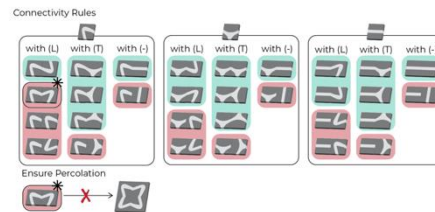


Figure A.1: Connectivity rules for (L), (T) and (-) tiles, with allowed connections (green shade) and prevented connections (red shade).

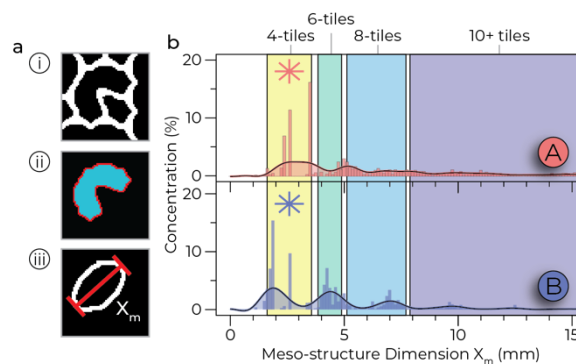


Figure A.2: (a) Meso-structure dimension analysis using elliptic fit to find X_m (meso-structure size), performed by image analysis.² (b) Meso-structure size

distributions for (A) and (B) architectures relating X_m dimension to concentration percent. Yellow, green, cyan, and blue represent 4, 6, 8, and 10+ tiles meso-structures, respectively.

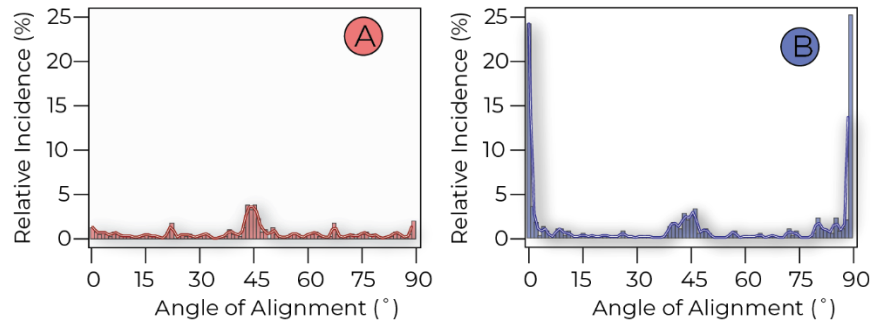


Figure A.3: (a,b) Meso-structure angle distribution in (A) and (B) networks (a and b, respectively).

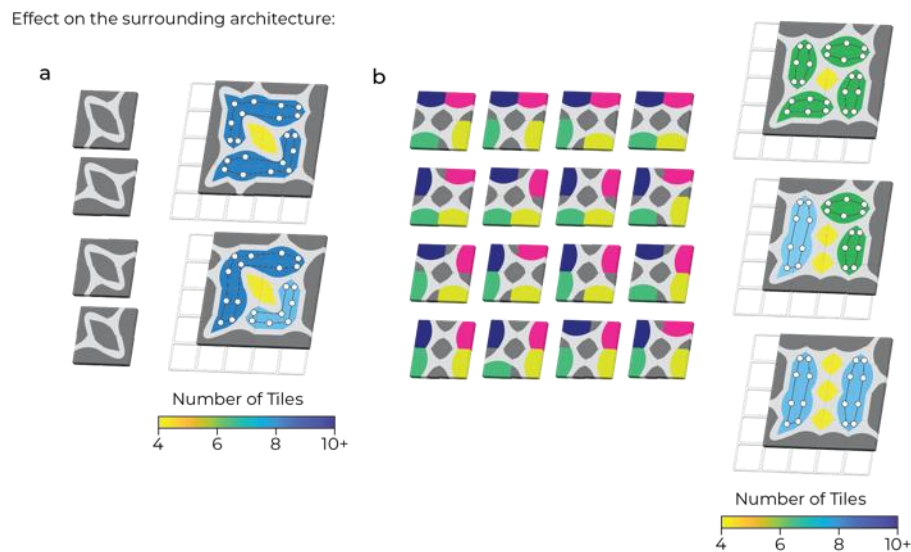


Figure A.4: (a) Meso-structure distributions around (L)-dominated 4-node substructures. (b) Substructure distributions around (T)-dominated architectures.

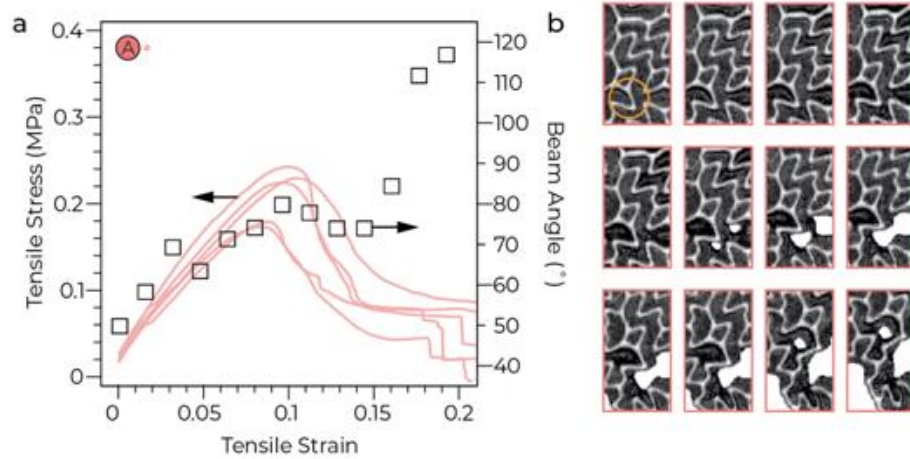


Figure A.5: (a) Engineering tensile strain-stress diagram plotted with opening angle of (L) tile as tensile loading is applied. (b) Progression of (L) tile angle opening under tensile loading.

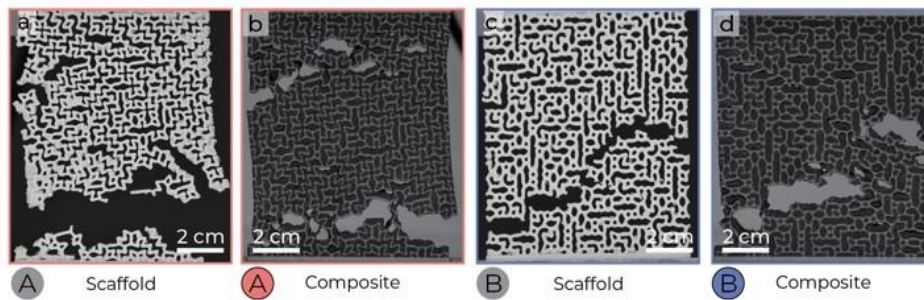


Figure A.6: Comparison of reinforcing network and composite failure locations under tensile loading. (a) (A) reinforcing network and (b) (A)-NRC showing the same failure locations. (c) (B) reinforcing network and (d) (B)-NRC showing the same failure locations.

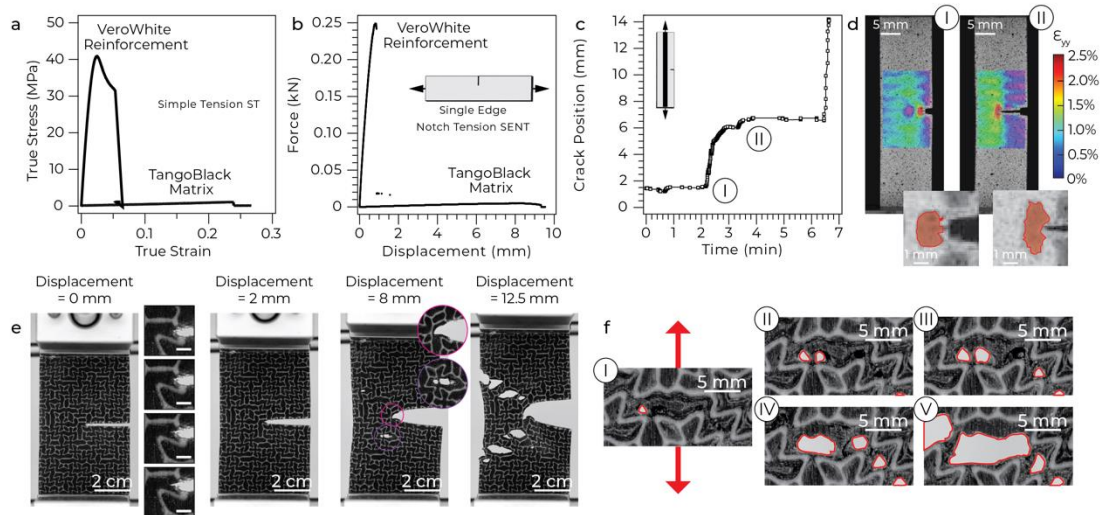


Figure A.7: (a) Simple tension experiment performed on VeroWhite and TangoBlack specimens. (b) Single edge notch tension (SENT) experiment performed on VeroWhite and TangoBlack specimens at a loading rate of 1mm/min. (c) Evolution of the crack position over time during the fracture of a VeroWhite-TangoBlack-VeroWhite specimen, confirming sequential events of crack arrest at the interface (I and II). The crack position has been retrieved by image analysis.² (d) Digital Image Correlation (DIC) maps of the e_{yy} strain during the test reported in (c). The inset confirms the sequential formation of a plastic zone in the VeroWhite portions subject to local yielding, as also observed in literature.^{2,3} (e) Optical photographs during a controlled fracture experiment (SENT geometry) of a network reinforced composite loaded at 1mm/min (initial crack length/specimen width ~ 0.5). Sequential details display the instantaneous propagation of a crack at small displacements internally to the first meso-structure, within the TangoBlack matrix (scale bar = 1 mm). Circular insets highlight the event of fracture arrest at the first soft to hard interface and the nucleation of a void in a nearby meso-structure. (f) Optical photographs highlighting the sequence of craze formation, fibril elongation, and fracture within the TangoBlack matrix phase, internally to a meso-structure.

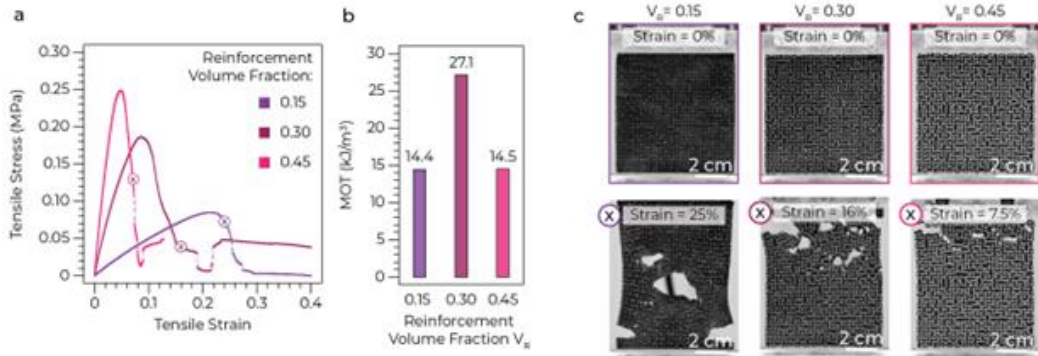


Figure A.8: (a) Stress strain curves recorded on A-NRCs with a different reinforcement volume fraction V_R , ranging from 0.15 to 0.45. (b) Modulus of Toughness (MOT) as a function of the reinforcement volume fraction. (c) Optical photographs depicting the evolution of the fracture in specimens with increasing reinforcement volume fraction 0.15 (left), 0.30 (center), and 0.45 (right).

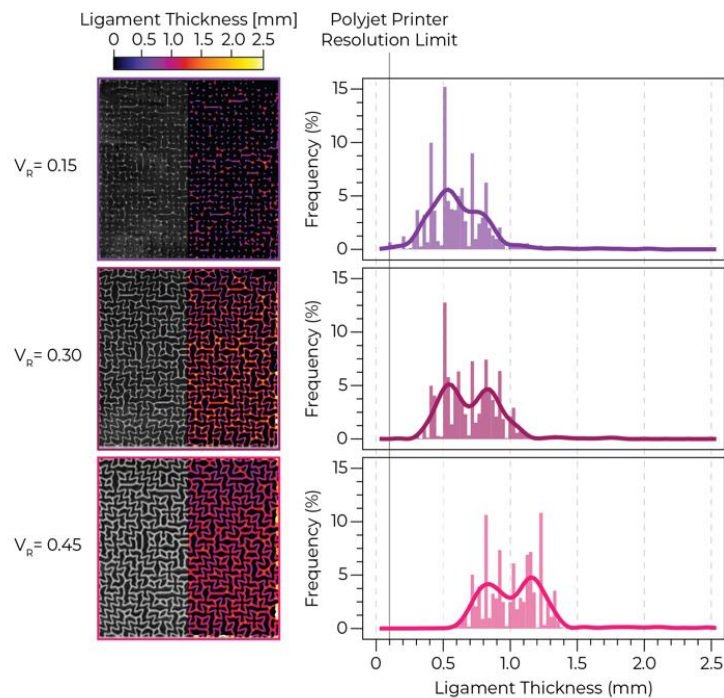


Figure A.9: (Left) Optical photographs of composites with increasing reinforcement volume fraction V_R ranging from 0.15 to 0.45. The ligament thickness map is obtained with the plugin ‘local thickness’³ in the open-source image analysis software Fiji² and it is then overlaid on the images. (Right)

Ligament thickness distribution for each specimen (bars), smoothing of the distributions measured for each specimen (solid lines).

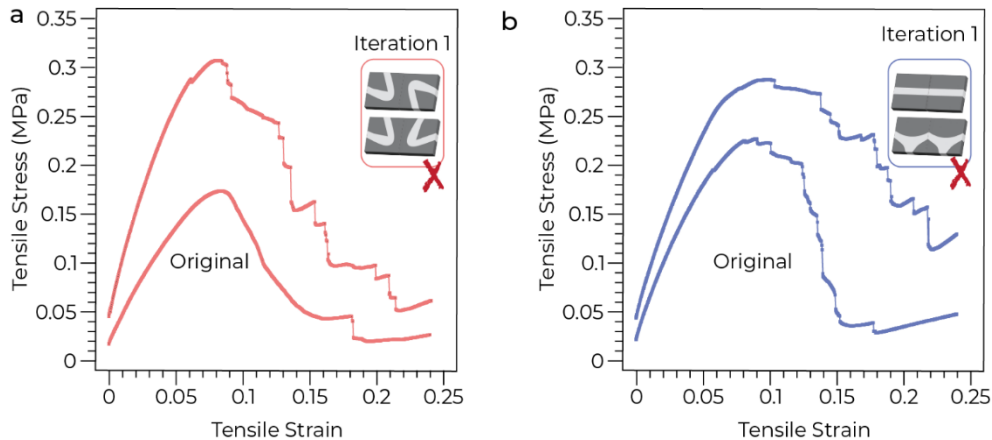


Figure A.10: Engineering tensile stress-strain diagrams showing connectivity rule modification effects. (a) Original (A) architecture (lower curve) comparison with first iteration (upper curve) of connectivity rule modifications as shown in upper right corner. (b) Original (B) architecture (lower curve) comparison with first iteration (upper curve) of connectivity rule modifications as shown in upper right corner.

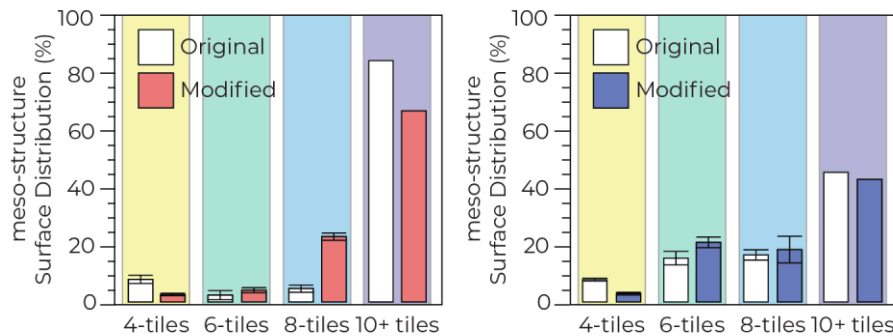


Figure A.11: Variations in distribution of meso-structure sizes for (A)-NRCs and Mod-(A)-NRCs (left) and (B)-NRCs and Mod-(B)-NRCs (right), measured by image analysis.² Yellow, green, cyan, and blue represent 4, 6, 8, and 10+ tiles meso-structures, respectively, before (white bars) and after (red and blue bars) connectivity rule modifications.

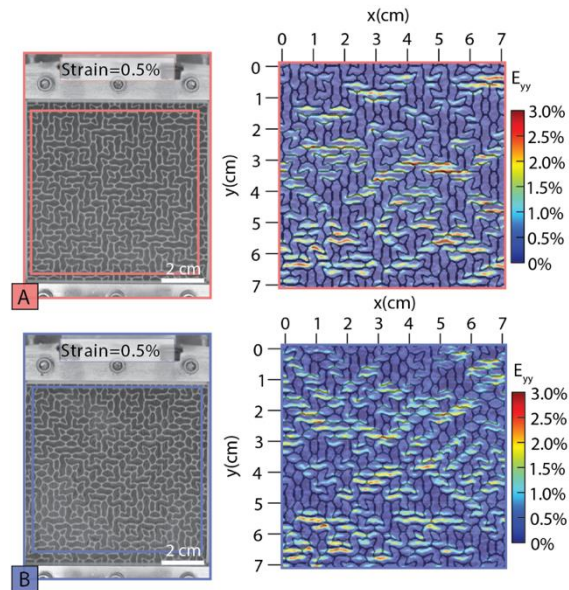


Figure A.12: Images (left) and digital image correlation maps (right) recorded at 0.5% strain of (A)* and (B)* composites (top and bottom, respectively).

A.3 Supplementary Discussion

A.3.1 The Virtual Growth Algorithm

The program used to design the composites iteratively grows irregular materials over a predefined area by selecting spatial sites, defined by two coordinates, and assigning tiles to these coordinates. The entropy of each site, defined as the number of available connections that can still be formed, a number that ranges from 1 to 4, is evaluated, and the sites with the lowest entropy are filled first. The algorithm then randomly selects tiles based on their initial concentration or availability, reported often as ‘frequency hints’ (Figure 1b, left). This parameter is provided as an input by the user. To ensure a smooth growth without local defects or discontinuity between the reinforcing and matrix phases, the connectivity of each tile is governed by a set of connectivity rules, also known as adjacency rules (Figure A.1). As the structure grows and the sites are occupied, each remaining available site can only be occupied by a limited number of tiles, arranged in a limited number of rotational configurations (Figure 2.1b, center). The growth algorithm then

proceeds with the random selection of one of the allowed tiles until it ensures the complete filling of the predefined area (Figure 1b, right). For this study, a specific (L) to (L) connection is not allowed, to prevent the formation of secondary disconnected architectures (Figure A.1).

A.3.2 The Reinforcing Networks

Networks are mathematical models that describe systems of nodes connected by edges. The rules that govern how nodes connect ultimately determine the network's characteristics, distinguishing an irregular network, which follows a set of rules to form an irregular pattern, from a random network, where nodes are connected randomly. Relying on the theoretical frameworks developed for continuous random networks, that describe the relationship between networks architecture and mechanical properties, we can characterize the reinforcing networks generated using the virtual growth algorithm based on their average coordination $\langle R \rangle$, the mean number of connections each node has, and their bridge length, defined as the distance between two nodes. In this context, among the different models developed, covalent networks have been extensively studied to describe amorphous solids and glasses, composed by atoms with different coordination, analogous to our system tiles. The average coordination of covalent networks $\langle R \rangle$ can be measured through constraint counting, estimating the network's stability and identifying floppy modes, independent deformations that occur with no cost in energy. The critical coordination $\langle R_c \rangle$ marks the transition between rigid and floppy behavior and can be used to predict the mechanical behavior of the network.

A.3.3 The Mechanical Behavior of the Reinforcing Networks

To confirm this description of the failure mechanisms in (L)-dominated and (T)-dominated architectures, we performed control experiments on the reinforcing networks and compared the results with the behavior of the composites.

(L)-dominated architectures: the experiments on the reinforcing networks consolidated our description of a transition from a bending- to a stretching-dominated behaviour. As the strain exceeded 20% (figure 3a, grey solid line and grey arrows, and Figure A.6) we observed the sequential fracture of the reinforcing network ligaments. Finally, these experiments allowed us to shed light on the role of the matrix during fracture. The reinforcing networks display a significantly lower strength than the composites: this suggests that the matrix has a key role during loading in resisting against the deformation of the meso-structures, requiring higher forces and thus increasing the total amount of energy that is needed to cause composite failure (Figure 3a, black solid line composite, grey solid line reinforcing network). Nonetheless, the matrix has a marginal role in influencing the trajectory of the cracks, which can almost perfectly overlap between the composite and the reinforcing network.

(T)-dominated architectures: To consolidate our description of their mechanical behavior, we performed control experiments on the reinforcing network of (B) architectures. As expected, they display a primarily stretching-dominated behavior, that features sequential failure events at lower strain values (Figure 2.3b, grey arrows, Figure A.6). As observed in the (L)-dominated architectures, the crack trajectory can almost perfectly overlap between the composite and the reinforcing network.

A.3.4 The Iterative Modification Design Process

With our approach, we display that without changing the shape or the volume fraction of the constitutive tiles, and without any shape optimization, it is possible, simply by changing the rules that govern the connectivity of tiles, to tune the mechanical properties of these architected materials. Although this study focused on improving the energy dissipated during fracture of the architectures, the iterative process of modifying connectivity rules and characterizing the mechanical response

allowed us to identify which set of rules can be modified to increase or to decrease various other mechanical properties. The two specific mechanical properties we examined during the iterative process were strength and strain-to-failure, which combined to give an improved fracture energy dissipation.

We began by removing the most prominent defect in each architecture. The tile distributions are directly responsible for the frequency of the type of defect in each architecture, and the most prominent defect is the one that occurs most often in an architecture. For (A), that was certain (L) to (L) connections, while for (B), certain (T) to (T) connections were the most problematic. Although the modified architectures (A) and (B) were generated using the exact same frequency hints as their original counterparts, the modification of the connectivity rules, and thus the possible substructures that could be formed, influenced their final composition: the modified designs (A_NO LL) and (B_NO TT) have a composition of 50% (T), 19% (L), and 31% (-) and 68% (T), 22% (L), and 10% (-), respectively.

We then performed the same mechanical testing and characterization of the modified (A) and (B) composites as described for the original composites. For both composites, the removal of the most prominent defects resulted in an increase in the modulus of toughness, but the mechanism behind the increase was different for (A) and (B) (Figure A.7). The increase in modulus of toughness for (A) was due to an increase in strength, while the increase in modulus of toughness for (B) was due to an increase in strain-to-failure. From this, we concluded that removal of (L) to (L) connections is responsible for strength and that removal of (T) to (T) and (-) to (-) connections is responsible for strain-to-failure.

To test this hypothesis, we then removed the (-) to (-) connections from (A) to improve its strain-to-failure (resulting in 37% (T), 58% (L), and 5% (-)), and the (L) to (L) connections from (B) (resulting in 83% (T), 9% (L), and 8% (-)) to

improve its strength. We again performed the same mechanical testing and characterization of the newly modified (A) and (B) architectures, and as expected, observed that the removal of (-) to (-) connections improved the strain-to-failure from the original (A) architecture, while removal of (L) to (L) connections improved the strength from the original (B). However, unlike the first modification, the second modifications did not have as great of an impact on the increase in modulus of toughness.

The improvements in strength and strain-to-failure are due to the tile distributions and thus meso-structure populations that result from the connectivity rules applied. Since energy dissipation during fracture is optimized by a combination of strength and strain-to-failure, we then decided to combine all the modulus of toughness improvements into a final set of connectivity rules that were applied to the original (A) and (B) architectures.

A.3.5 The Polydispersity Index (PDI)

Borrowing the concept from the field of polymer science, a measure of the polydispersity of a polymer is the polydispersity index (PDI), defined as the ratio of M_w (weighted average mass) over M_N (number average mass). The parallel between polymers and irregular architected materials is apparent in this case; each tile can be seen as one monomer, and each formed substructure can be seen as one polymer chain. The total amount of tiles (or monomers) is fixed by the total extension of the material and the final assembly will therefore be a collection of differently sized meso-structures (or polymer chains). In this context, we propose here that comparing the PDI of each architecture can be a quick method to evaluate the homogeneity of each architecture. The PDI is calculated following Equation 1:

$$PDI = M_w/M_N, \quad (1)$$

in which M_W and M_N are given by Equation 2 and 3 respectively:

$$M_W = \frac{\sum(\text{Area}^2 * \text{Counts})}{\sum(\text{Area} * \text{Counts})}, \quad (2)$$

$$M_N = \frac{\sum(\text{Area} * \text{Counts})}{\sum(\text{Counts})}. \quad (3)$$

Area is the enclosed area of an n^{th} meso-structure and Counts is the frequency (the number of times) it gets measured.

As it is defined, the PDI is larger than 1.0 and the closer it is to 1.0, the more homogeneous the architecture is. As a result of more stringent connectivity rules, that bias the growth of architectures capable of higher energy dissipation during fracture, we observed across the design space an overall decrease of the PDI, suggesting that the modified architectures become more homogeneous (Table 1).

Table 1:

Architecture #	(T)	(-)	(L)	PDI Original	(T)*	(-)*	(L)*	PDI Modified*
1	62	18	20	1.78	63	18	19	1.41
2	60	29	11	1.81	65	18	17	1.37
3	57	6	37	2.08	64	12	24	1.58
4	42	45	13	1.85	58	22	20	1.39
5	19	2	79	1.80	49	26	25	1.36
6 (A)	35	10	55	2.09	54	19	27	1.41
7	36	28	36	2.27	53	24	21	1.51
8 (B)	80	10	10	1.81	71	11	18	1.45

BIBLIOGRAPHY

- [1] L. Jiaying Tan et al., *Recent Progress on Polymer Materials for Additive Manufacturing* **2020**, doi:10.1002/adfm.202003062.
- [2] J. Schindelin et al., *Nat Methods* **2012**, 9, 676–682.
- [3] T. Hildebrand, P. Rügsegger, *J Microsc.* **1997**, 185, 67–75.
- [4] K. Liu, R. Sun, C. Daraio, *Science* **2022**.
- [5] M. F. Thorpe, *J. Non. Cryst. Solids* **1983**, 57, 355–370.
- [6] M. F. Thorpe, D.J. Jacobs, N.V. Chubynsky, A.J. Rader, *Rigidity Theory and Applications* **1999**, 239–277.

Appendix B

FRACTURE CHARACTERIZATION OF BIOINSPIRED
IRREGULAR NETWORK REINFORCED COMPOSITES

B.1 Supplementary Figures

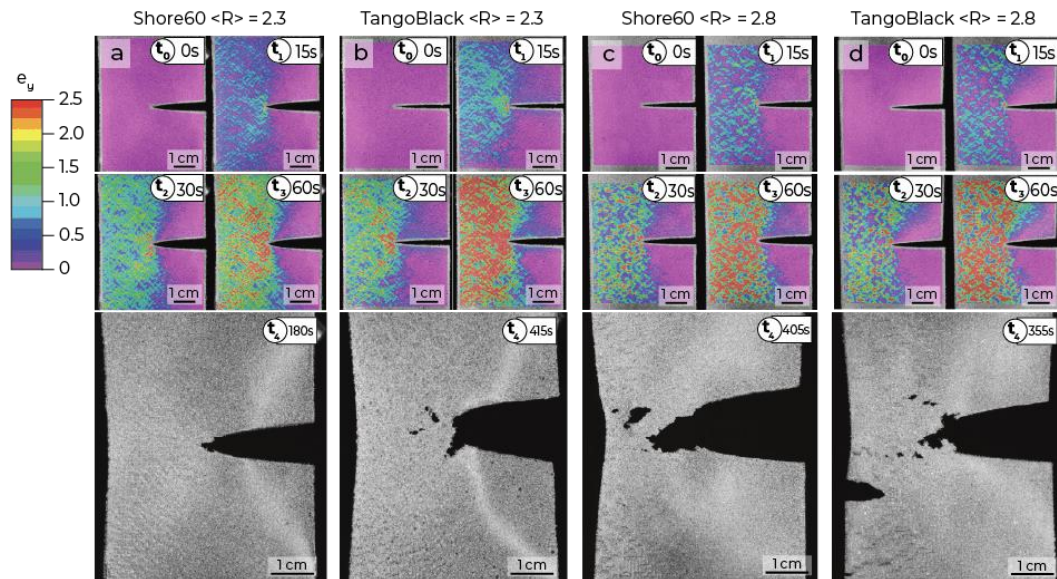


Figure B.1: DIC images and fracture nucleation images for composite samples with different matrix phases. (a) 2D DIC strain maps and fracture nucleation image for 2.3 coordination composite sample with Shore60 matrix. (b) 2D DIC strain maps and fracture nucleation image for 2.3 coordination composite sample with TangoBlack matrix. (c) 2D DIC strain maps and fracture nucleation image for 2.8 coordination composite sample with Shore60 matrix. (d) 2D DIC strain maps and fracture nucleation image for 2.8 coordination composite sample with TangoBlack matrix.

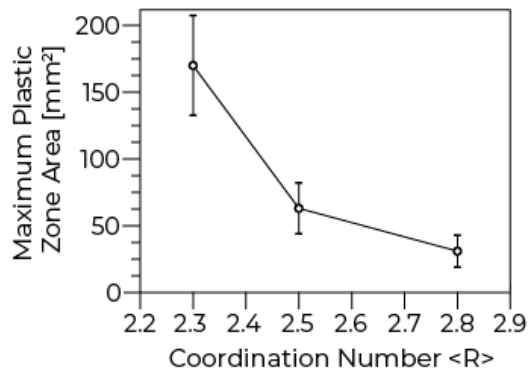


Figure B.2: Maximum plastic zone size reached as a function of coordination number for 2.3, 2.5, and 2.8 samples.

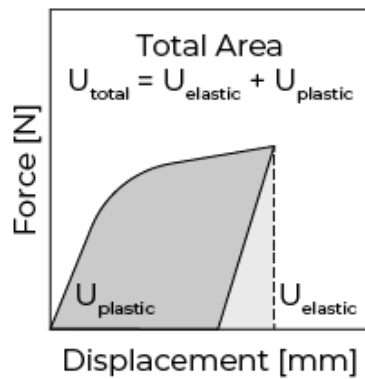


Figure B.3: Calculating the incremental J-integral as elastic and plastic components.

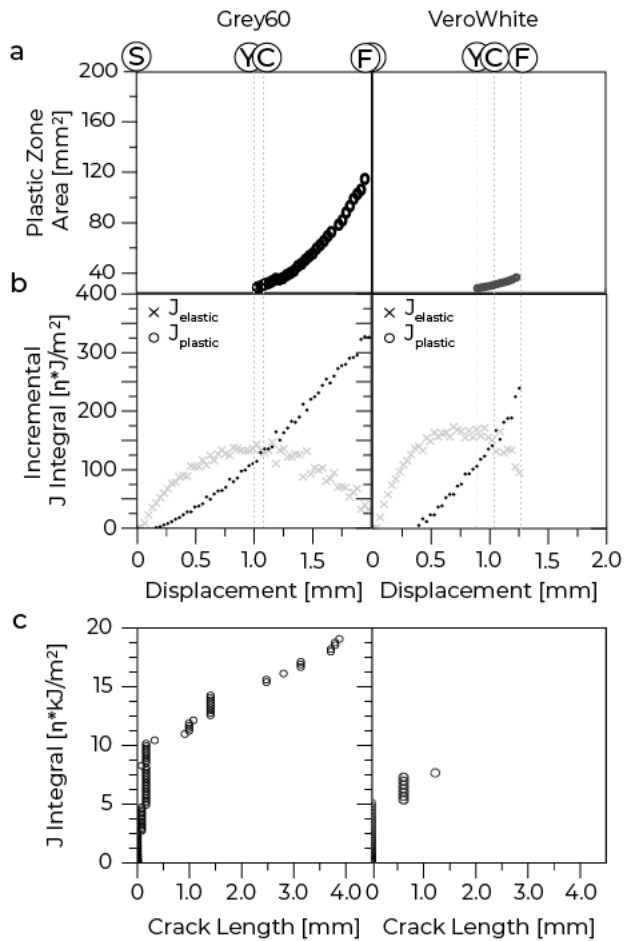


Figure B.4: Plastic zone size, J integral and R-curves for bulk material samples. (a) Plastic zone area as a function of displacement for Grey60 and VeroWhite samples. S corresponds to start of the test, Y corresponds to time at yield, C corresponds to time at crack initiation, F corresponds to time at failure. (b) Incremental elastic J integrals (η_e normalized) and plastic J integrals (η_p normalized) as a function of displacement for Grey60 and VeroWhite samples. (c) R-curves for Grey60 and VeroWhite samples.

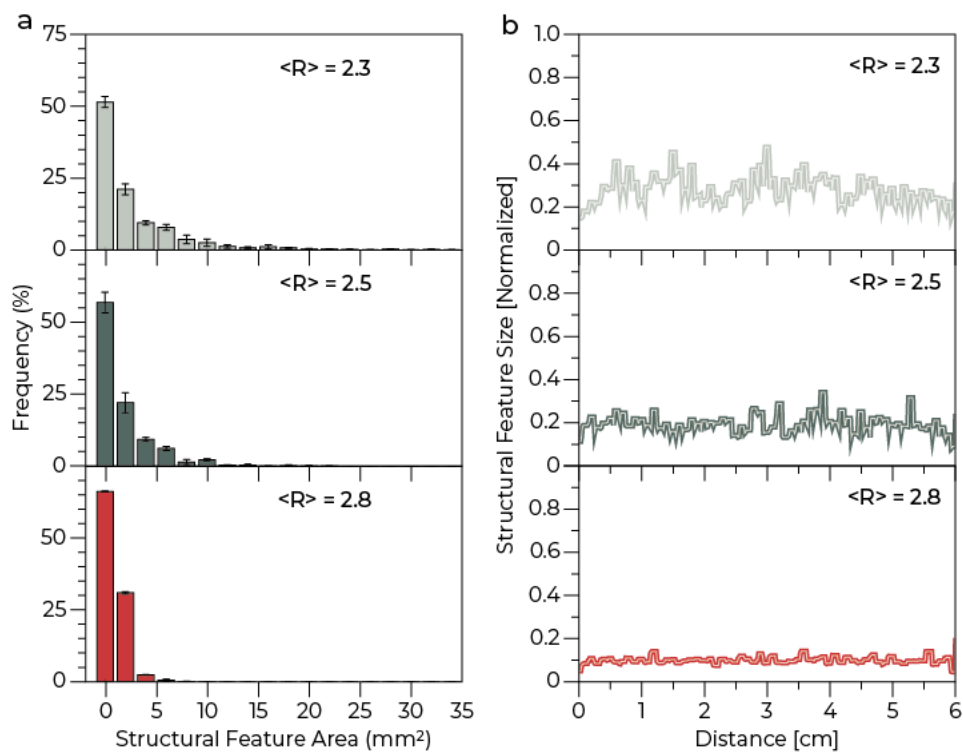


Figure B.5: Structural feature characterization. (a) Structural feature area distributions for 2.3 coordination (top), 2.5 coordination (middle) and 2.8 coordination (bottom) samples. (b) Structural feature area profiles as a function of distance across the sample for 2.3 coordination (top), 2.5 coordination (middle), and 2.8 coordination (bottom) samples.

B.2 Supplementary Discussion

B.2.1 Structural Feature Characterization

By plotting the profile of feature sizes across the samples, we also observe that features are isotropically distributed, and that the average size profile varies across the coordination numbers (Figure B.5). For the 2.8 coordination samples, the smallest features appear as a high frequency with a minimum wavelength of one characteristic length, while for the 2.5 and 2.8 coordination samples, which can form larger features, lower frequencies emerge in addition to the higher frequencies, all of which are superimposed as a result of averaging across the entire structure (Figure B.5).

Appendix C

MECHANICAL AND TEMPORAL RESPONSE OF HIGH-COORDINATED IRREGULAR NETWORK REINFORCED COMPOSITES

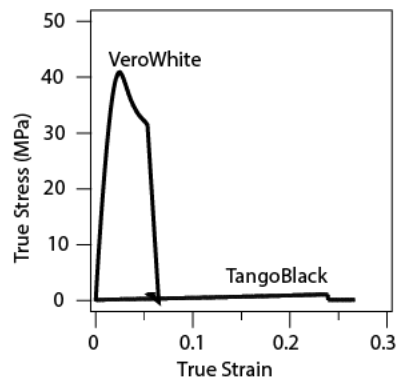
C.1 Supplementary Figures

Figure C.1: Simple tension experiment performed on VeroWhite and TangoBlack samples.

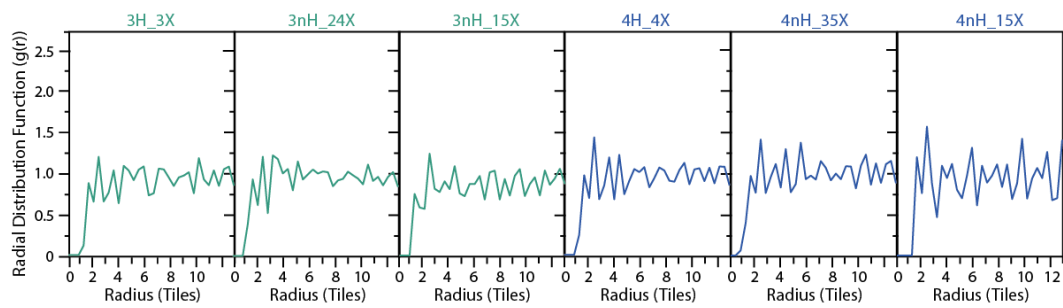


Figure C.2: Radial distribution functions for various topologies.

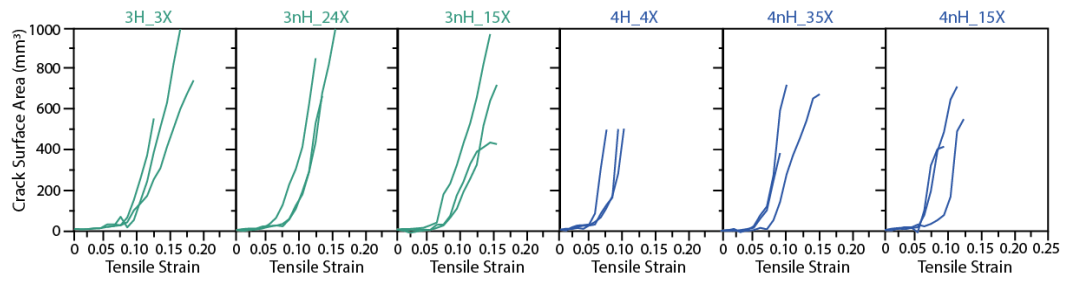


Figure C.3: Crack surface area opened as a function of tensile strain for various topologies.

Appendix D

EXTRACTING GEOMETRY AND TOPOLOGY OF ORANGE PERICARPS FOR THE DESIGN OF BIOINSPIRED ENERGY ABSORBING MATERIALS

D.1 Supplementary Figures

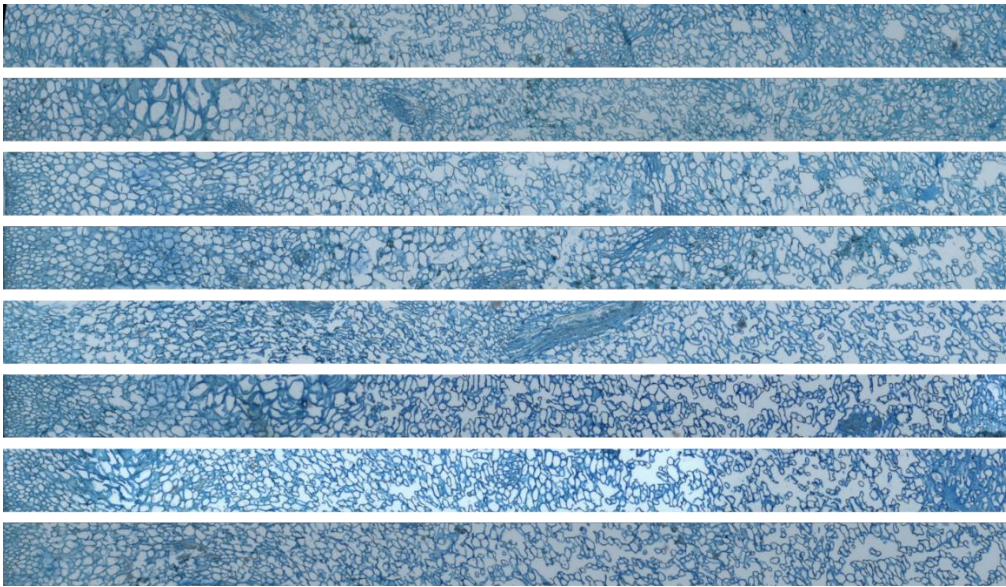


Figure D.1: All orange pericarp cross sections from 0 mm to 5 mm into the fruit.

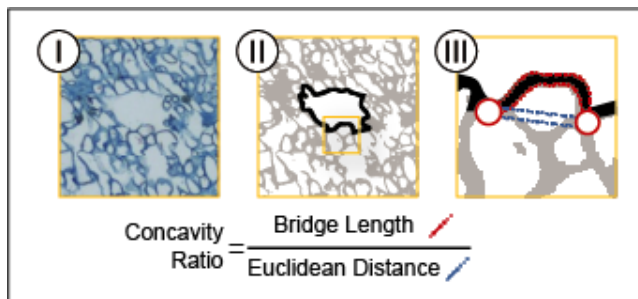


Figure D.2: Concavity description. (I) Original orange pericarp image. (II) Selected feature. (III) Highlighted bridge length (red) and Euclidean distance (blue).

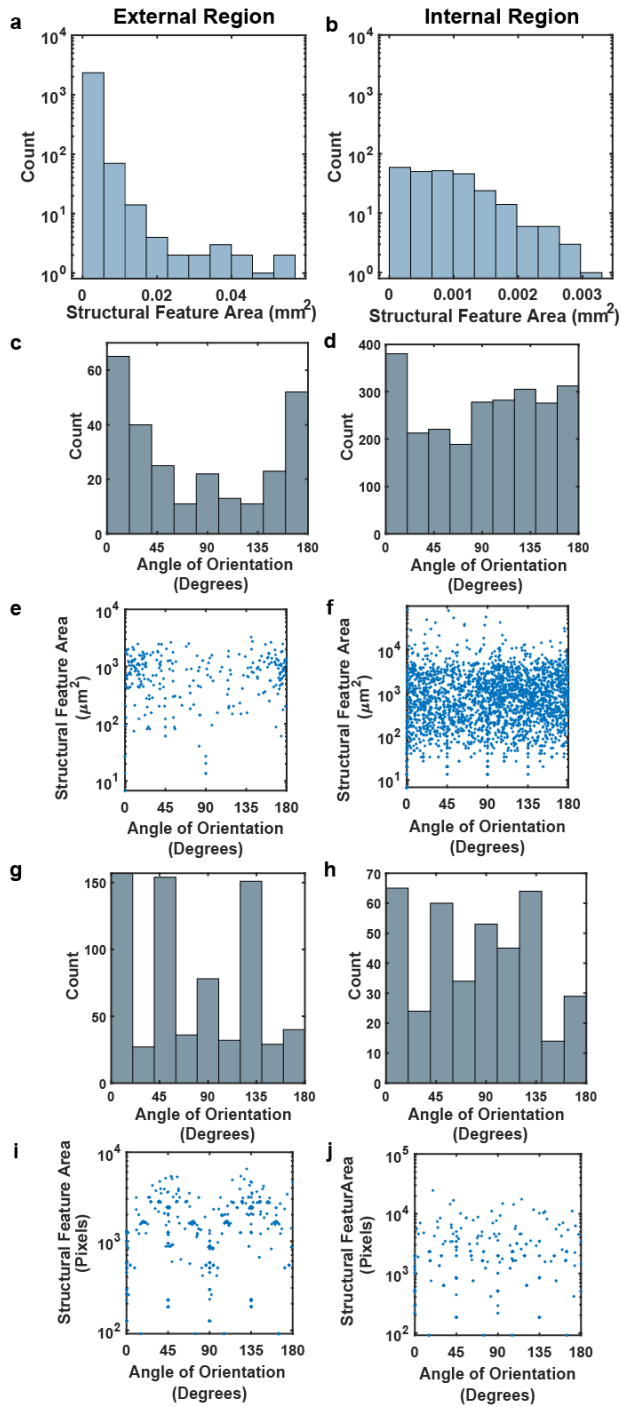


Figure D.3: Orange pericarp and VGA sample characterization. (a) Counts of structural feature areas for external region of orange pericarp. (b) Counts of structural feature areas for internal region of orange pericarp. (c) Counts of structural feature angle of orientation for external region of orange pericarp. (d)

Counts of structural feature angle of orientation for internal region of orange pericarp. (e) Structural feature area plotted as a function of elliptic fit angle of orientation of structural features for external region of orange pericarp. (f) Structural feature area plotted as a function of elliptic fit angle of orientation of structural features for internal region of orange pericarp. (g) Counts of structural feature angle of orientation for external region of VGA sample. (h) Counts of structural feature angle of orientation for internal region of VGA sample. (i) Structural feature area plotted as a function of elliptic fit angle of orientation of structural features for external region of VGA sample. (j) Structural feature area plotted as a function of elliptic fit angle of orientation of structural features for internal region of VGA sample.

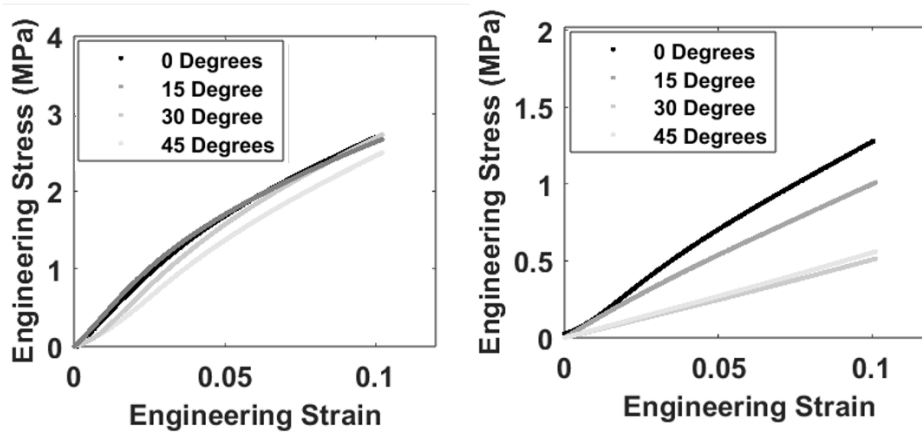


Figure D.4: External region (left) and internal region (right) engineering stress-strain plot for 0-, 15-, 30-, and 45-degree rotated VGA samples.

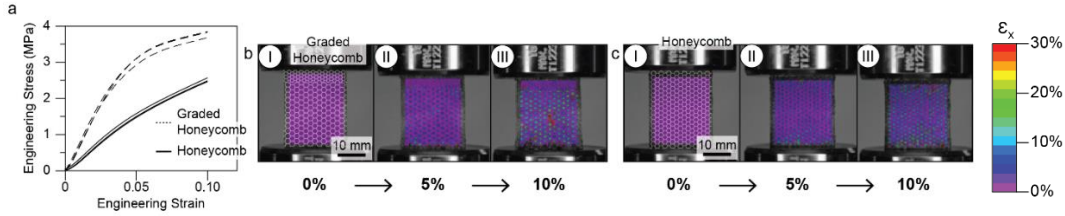
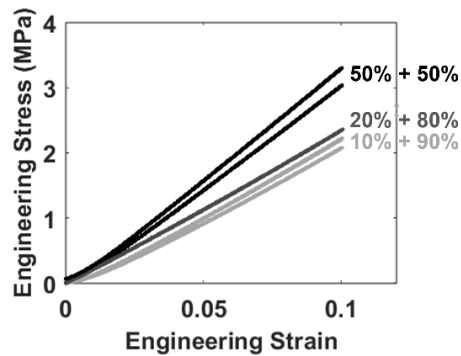
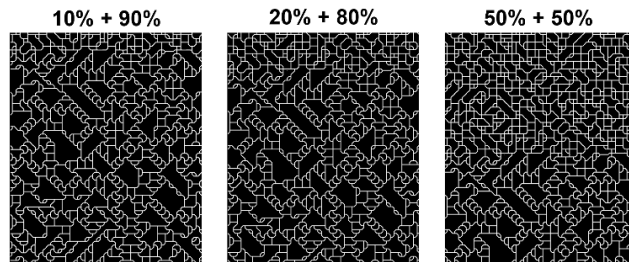


Figure D.5: Quasi-static compression tests. (a) Engineering stress-strain plot for graded and periodic honeycomb samples. (b) Example 2D DIC strain maps for 0%, 5%, and 10% global strain for graded honeycomb sample. (c) Example 2D DIC strain maps for 0%, 5%, and 10% global strain for periodic honeycomb sample.



Sample	Coefficient of Restitution
1 - 10% + 90%	0.29
2 - 20% + 80%	0.33
3 - 50% + 50%	0.36

Figure D.6: Sample external and internal region combinations. Sample PNG's for 10% + 90%, 20% + 80%, and 50% + 50% (top). Compressive stress strain data for each variation (center). Coefficient of restitution for each variation (bottom).

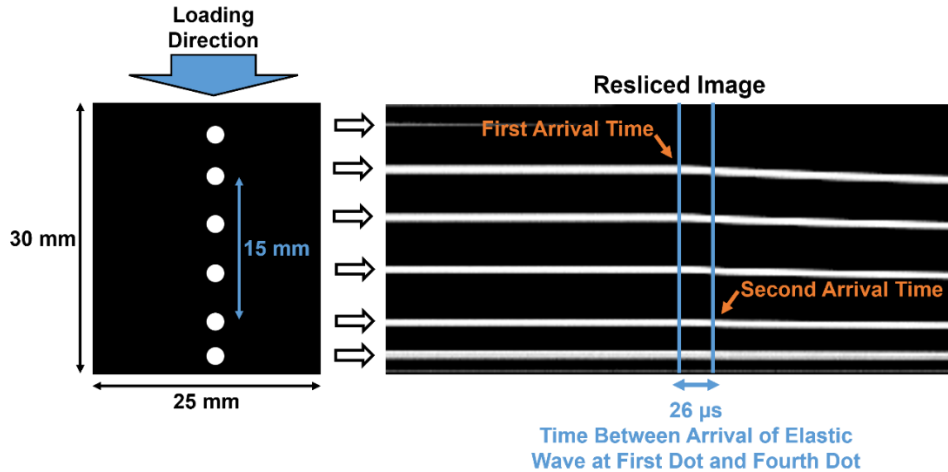


Figure D.7: Wave speed propagation in composite materials. Sample with linear dot pattern and loading direction (left). Resliced image in time with dot trajectories over time as deformation reaches each dot (right).

D.2 Supplementary Discussion

D.2.1 Sample Preparation and Imaging

Tissue samples of approximately 1 cm^3 are collected directly from the orange fruit and include the outer layer (*exocarp* or *flavedo*) and the inner white layer (*mesocarp* or *albedo*)^[1]. The samples are first immersed in a fixative solution, a 4% buffered glutaraldehyde solution at pH 7.2 (*Glutaraldehyde Solution 25% in H₂O*, Sigma Aldrich). The samples remain in the fixative solution for 24 hours, to ensure the complete penetration of the fixative in every part of the biological tissue. The tissues are then sequentially immersed in 70%, 80%, 90%, 95%, and 100% v/v ethanol solutions (*Ethanol Absolute Anhydrous for analysis RPE*, Carlo Erba Reagents), to ensure the complete removal of any water trace. Subsequently, the tissues are immersed in terpene (natural origin, *Bio Clear*, Bio-Optica) for two hours. Terpene is an organic solvent that is miscible with alcohol and with most waxes. The next step is the infiltration of the tissues with an embedding medium. For the purpose, we transfer the tissues into disposable PVC molds, (*DispoMold*, Bio-Optica) fill the molds with liquid paraffin wax at 56°C (*Histosec Pastilles*,

Sigma-Aldrich) and leave it overnight in a temperature-controlled oven at 56°C, to ensure complete infiltration of the paraffin within the tissues. The precise positioning of the tissues is critical to determine the subsequent imaging cross section. The following day, a dedicated support for histological inclusion (*Ring*, Bio-Optica) is placed on top of the PVC mold, filled with liquid paraffin at 56°C and left it to solidify at room temperature. The paraffin block is then mounted on a microtome (RMC Products, Boeckeler MR3) and thin sections are cut (~5 µm). The thin sections are then transferred on microscopy glass slides. After drying, the paraffin-embedded thin tissue slices are treated in terpene (natural origin, *Bio Clear*, Bio-Optica) to eliminate any trace of paraffin. Then we proceed with the re-hydration of the tissues. This is done by immersing the thin tissue slices in solutions with decreasing concentrations of ethanol (*Ethanol Absolute Anhydrous for analysis RPE*, Carlo Erba Reagents): 100% (pure ethanol), 95%, 80%, 50%, and 0% v/v (pure water). After the re-hydration of the tissues, we proceed with the staining. First, we immerse the tissues in a 3% acetic acid solution (*Acetic Acid Solution*, Sigma Aldrich) for 5 minutes. We then perform the staining for 30 minutes using Alcian Blue (*Alcian Blue Solution*, Sigma Aldrich). After rinsing with distilled water, we then perform the counterstaining using Safranin (*Safranin T RS-for Microscopy, Hydroalcoholic Solution*, Carlo Erba Reagents) for 5 minutes. We finally wash the stained tissues using distilled water for 1 minute. Before imaging, the tissues are de-hydrated by sequential immersions in 80%, 95%, and 100% v/v ethanol solutions and immersed in terpene (natural origin, *Bio Clear*, Bio-Optica) for ten minutes. Finally, the thin tissue slices are protected by a mounting cover glass, fixed on top of the microscopy glass slide with a refractive index matching acrylic resin (*Eukitt*, Bio-Optica). An upright optical microscope (Axiophot Microscope, Zeiss) is used for observation with a magnification of 10X and 20X. High resolution images were then acquired with a digital camera (CMOS 11 Discovery C30).

D.2.2 Bioinspired Sample Generation

To generate samples, we use a virtual growth algorithm developed by Liu et al.^[2] and further described by Magrini et al.^[3], to generate a PNG file, which is scalable to any size. From the limitations of the additive manufacturing process and testing setup size, we choose samples with a tile size of 0.5 mm x 0.5 mm and a branch thickness of 0.1 mm.^{[2][3]} The PNG file is then extruded and converted to an STL file to be printed using a Stratasys Objet500 Connex polyjet printer, with a stiff viscoelastic resin (Stratasys VeroWhite Polyjet Resin) for the reinforcing structure, and a soft elastomeric resin (Stratasys TangoBlack Polyjet Resin) for the matrix, both of whose mechanical properties fall within those reported in literature^[4-6]. To investigate the spatially-varying density of the orange pericarp, samples with 0% external and 100% internal regions, 10% external and 90% internal regions, 20% external and 80% internal regions, and 50% external and 50% internal regions, and 100% external and 0% internal regions were all generated. Although the actual orange pericarp has approximately the 10% and 90% region breakdown, the sample dimensions required for testing limits the size of the samples, while the printer's lateral resolution of 40-85 μm ^[7] limits the number of tiles that can be printed for a given sample size and thus the 20% and 80% sample is the optimal tradeoff to maintain a thin external region while having sufficient structural features to understand the structure-property relationship.

D.2.3 Quasi-static Mechanical Testing

Polymer composite samples with a height of 2.5 cm, a width of 2.5 cm and a thickness of 1 cm for the external and internal regions, and with a height of 3 cm, a width of 2.5 cm and a thickness of 1 cm for the combination samples, are tested using an Instron E3000 (Instron, USA) with a 5 kN load cell and compression platens to apply compressive loading at a rate of 1 mm/min up to 10% strain.

D.2.4 Digital Image Correlation

For the digital image correlation, polymer composite samples are spray painted with flat white paint and then speckled with flat black paint to achieve speckles with a diameter of 0.1-0.3 mm. VIC-2D (Correlated Solutions, USA) is used to analyze the Lagrangian strain fields using a subset size of 35 and a step size of 2, such that each subset contains 3x3 to 5x5 speckles and each speckle contains at least 3x3 pixels.

D.2.5 Dynamic Testing

The drop tower consists of an aluminum tube with wall thickness of 0.3 cm, inner diameter of 2.7 cm, and height of 3 m, attached to a steel frame. A 10 cm steel striker with a diameter of 2.5 cm and a mass of ~400 g is released and falls down the tube to impact the sample, positioned and glued at the base, with an impact velocity of 7-8 m/s. A photodiode placed at the base of the tube, just above the sample, captures the moment the striker passes the bottom of the tube, and is used to trigger a high speed camera (Phantom v1610, Vision Research, AMETEK, USA), which captures images of the event at 50,000 frames per second, with resolution of 512 by 512 pixels.

D.2.6 Dynamic Wave Speed Testing

The elastic wave speed is measured during the drop tower test by placing a vertical line of white dots on a sample, in the direction of loading, and using a high-speed camera (Phantom v1610, Vision Research, AMETEK, USA) at 500,000 frames per second to capture when the dots move relative to one another as a measure of when the wave arrives and then dividing the distance between dots by the time interval between arrival events (Figure D.7).

D.2.7 Tiles and Connectivity Rules

We determine the type of tile by examining its perimeter and assigning a binary value of 1 to the left, 10 to the top, 100 to the right, and 1000 to the left and summing the perimeter values for each tile. If we have a 0-coordination tile, also called ‘empty tile’, the perimeter values sum to 0. 2-coordination tiles display perimeter values that sum either to 101 or 1010 for tiles that feature a vertical or horizontal straight line, or to 11, 110, 1100 or 1001 for tiles that feature a diagonal line in their 4-fold rotations. 3-coordination tiles have perimeter values that sum to 111, 1011, 1110 or 1101, depending on their orientation, while 4-coordination tiles have a perimeter sum that is always equivalent to 1111. Following this counting approach, we can then assign a reduced geometry tile equivalent to the original irregular tile. It should be noted that the irregularity of the orange pericarp means that there is no preferential orientation for any tile and all orientations are approximately equally represented in the tile counts. We determine the connectivity rules by determining how often a rule appears relative to the rest of the rules, by examining the tiles adjacent to the right and bottom of each tile. For the virtual growth algorithm approach in this work, it is only possible to either allow or disallow any connectivity rule.

D.2.8 Quasi-static Sample Anisotropy Testing

As discussed in the main article, it should be noted that as a result of the four-sided nature of the virtual growth algorithm tiles and limited sample size, the structural features of the VGA-generated samples have a certain degree of anisotropy with respect to the amount of reinforcing material in the loading direction, as defined by feature orientation (Figure D.3h, 3g). To investigate the effect of anisotropy on the mechanical properties of the samples, we generated VGA-ext and VGA-int samples that feature a structure rotated by 15°, 30°, and 45° and tested them in compression to determine their stiffness (Figure S4). The VGA-ext samples are nearly isotropic, with all rotated samples falling within 9% of the original sample’s stiffness, while

the VGA-int samples display up to 31% lower stiffness at 30° compared to 0°, indicating a higher degree of anisotropy (Figure S4). However, this is an artefact of the finite sample size that we tested and is attributed to the largest structural features with a limited number of orientations that dominate the loading response in a given sample.

BIBLIOGRAPHY

- [1] M. Jentzsch, V. Albiez, T. C. Kardamakis, T. Speck, *Soft Matter* **2024**, *20*, 2804.
- [2] K. Liu, R. Sun, C. Daraio, *Science* **2022**, *377*, 975.
- [3] T. Magrini, C. Fox, A. Wihardja, A. Kolli, C. Daraio, *Advanced Materials* **2023**, *2305198*.
- [4] J. R. C. Dizon, A. H. Espera, Q. Chen, R. C. Advincula, *Addit Manuf* **2018**, *20*, 44.
- [5] D. Bell, T. Siegmund, *Addit Manuf* **2018**, *21*, 658.
- [6] V. Slesarenko, S. Rudykh, *Int J Eng Sci* **2018**, *123*, 62.
- [7] L. Jiaying Tan, W. Zhu, K. Zhou, L. J. Tan, W. Zhu, K. Zhou, *Adv Funct Mater* **2020**, *30*, 2003062.

Appendix E

CONTROLLABLE INTERLOCKING FROM IRREGULARITY IN
TWO-PHASE COMPOSITES

E.1 Supplementary Figures

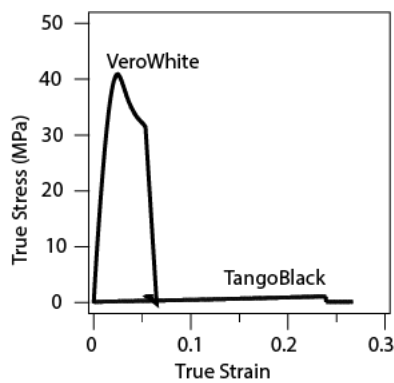


Figure E.1: Simple tension experiment performed on VeroWhite and TangoBlack samples.

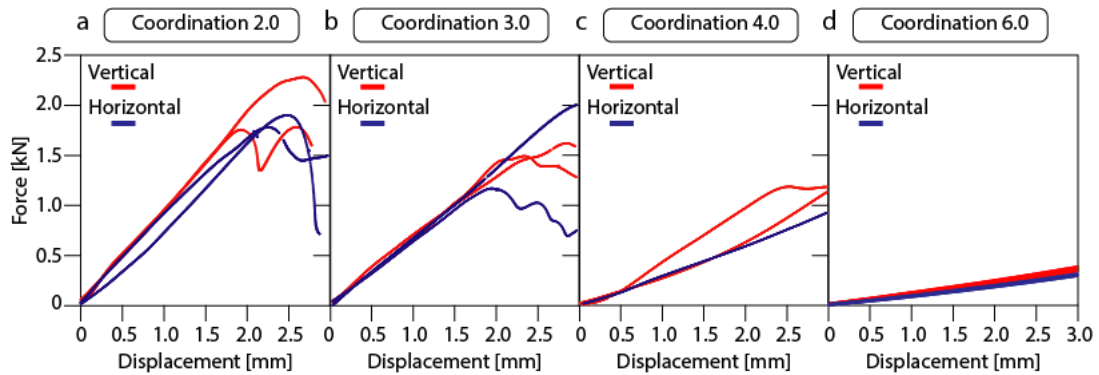


Figure E.2: Force-displacement plots for volume fraction equivalent periodic samples for coordinations 2X, 3X, 4X, and 6X, respectively. Red refers to vertical matrix orientation, blue refers to horizontal matrix orientation.

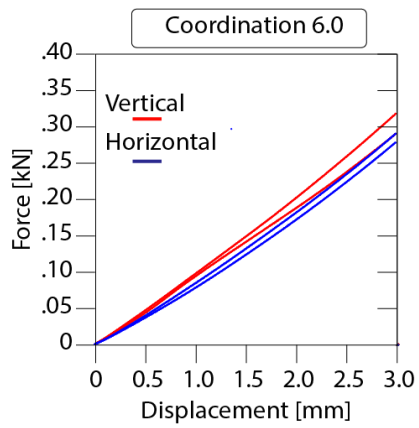


Figure E.3: Force-displacement plots for coordination 6X, zoomed in to show variation from sample orientation.

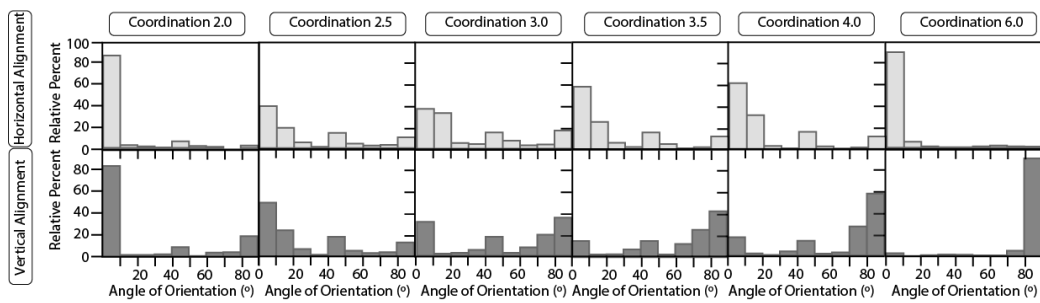


Figure E.4: Angle of orientation of particles as a function of alignment and coordination number.

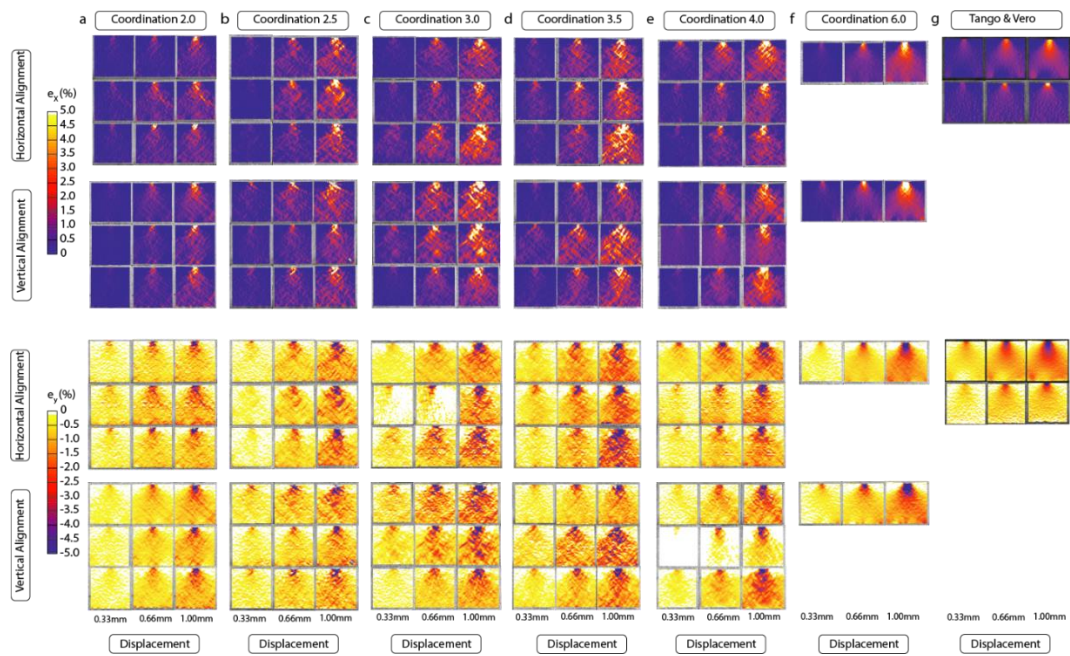


Figure E.5: Cylindrical contact loading characterization. 2D DIC maps of all samples for ϵ_x strain (above) and ϵ_y strain (below).

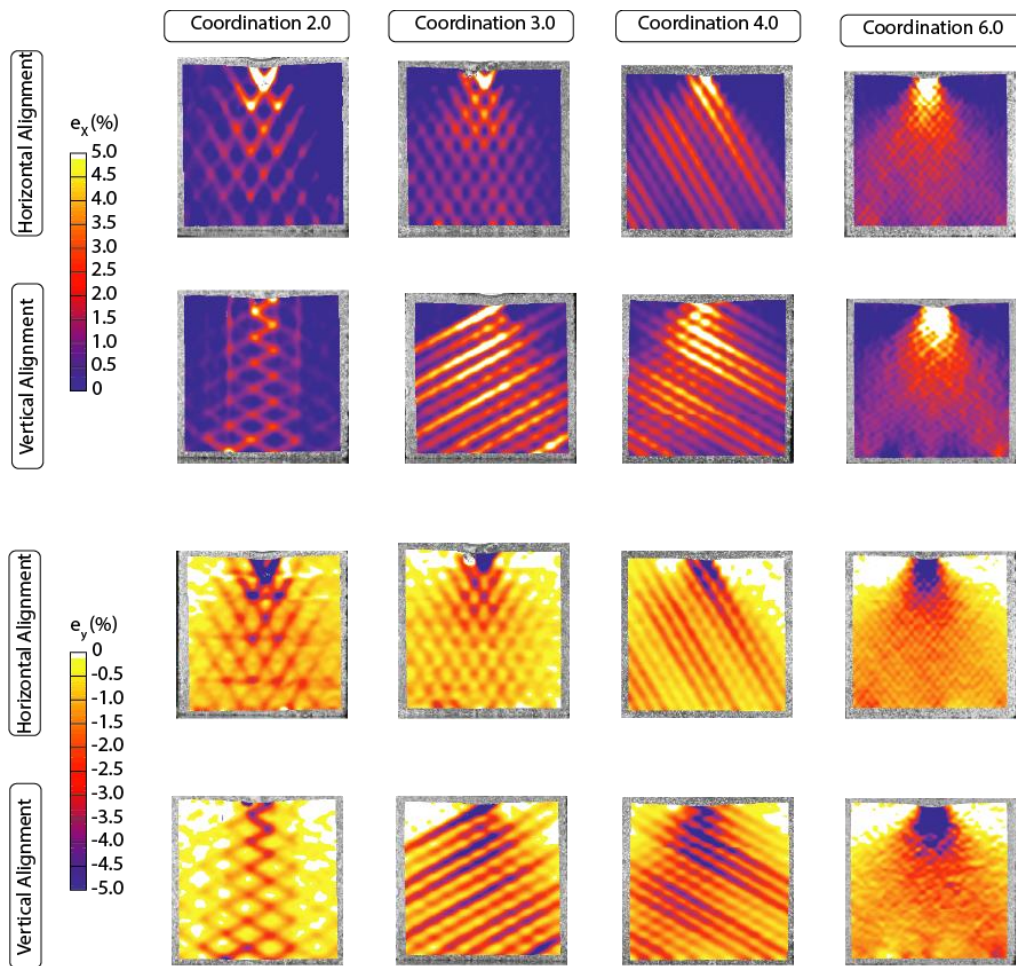


Figure E.6: 2D DIC maps of equivalent volume fraction 6X samples for ϵ_x strain (above) and ϵ_y strain (below) at 1 mm cylindrical contact displacement.

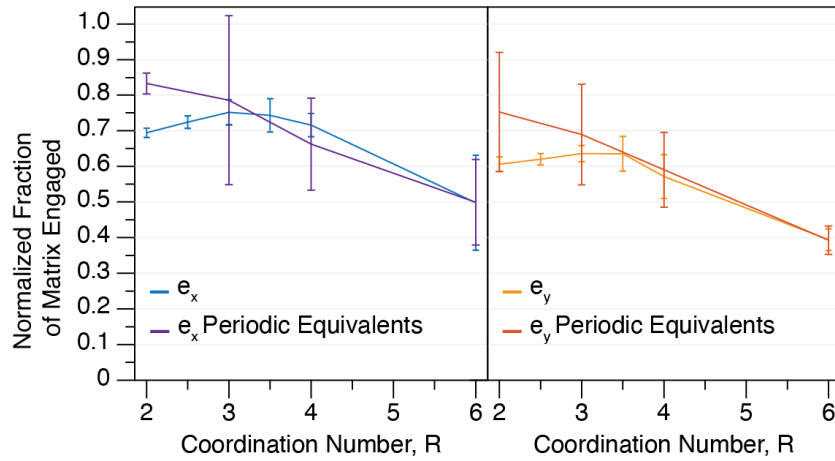


Figure E.7: Volume normalized fraction of matrix engaged as a function of coordination number at 1 mm cylindrical contact displacement for comparison of irregular samples and periodic equivalent 6X coordination samples.